

Development of a Novel Commercial-Scale Atmospheric Pressure Spatial Atomic Layer Deposition System

by

Chee Hau Teoh

A thesis
presented to the University of Waterloo
in fulfillment of the
thesis requirement for the degree of
Master of Applied Science
in
Mechanical and Mechatronics Engineering

Waterloo, Ontario, Canada, 2020

© Chee Hau Teoh 2020

Author's Declaration

I hereby declare that I am the sole author of this thesis. This is a true copy of the thesis, including any required final revisions, as accepted by my examiners.

I understand that my thesis may be made electronically available to the public.

Abstract

Atmospheric pressure spatial atomic layer deposition (AP-SALD) is an advanced thin-film fabrication technique. It can produce high quality (uniform, conformal, pin-hole free), large-area ultrathin films at speeds up to hundreds of times faster than conventional ALD. In this work, a pilot-scale industrial AP-SALD system was successfully designed and built from the ground up. A zinc oxide thin film was successfully deposited on a large borosilicate glass substrate with the system at high speed.

The industrial AP-SALD system has a reactor head that is modular and configurable for functional flexibility and scalability to produce thin films by leveraging on the atomic layer deposition method. The reactor head is made up of different types of components such as precursor gas slits, exhaust slits, plasma sources, and heating and/or a cooling channels for configurable depositions. CFD simulations in 2-dimensional (2D) and 3-dimensional (3D) models were conducted to guide the reactor design based on the isolation of precursor gases and the uniformity of precursor flow. The interspaced elevation and widths of each component can be adjusted to provide tunable control of the flow of gases. A positioning system with a mounting component for the reactor head is designed to provide flexibility in configuring and maintaining the orientation as well as the position of the reactor head relative to the substrate(s). The positioning system uses three laser sensors and four linear actuators to achieve desired reactor head-substrate spacing based on plane equations and rotation matrices. A heating stage with suction is used to heat up and to hold substrates of different sizes, geometry, and thickness. A heater controller box was built to control the heating through the connection with the PLC. A built-in temperature process program from Siemens PLC is used to configure the parameters of the PID controller for the heater. A linear stage is used to oscillate the substrates relative to the modular reactor head. A 3rd order motion profile is implemented to limit the jerk in the system.

Acknowledgements

Foremost, I would like to express my most profound gratitude to Dr. Kevin Musselman for his continuous support throughout my study and research. Dr. Kevin Musselman has always been supportive, approachable, and helpful throughout my master's study. His encouragement and understanding helped me overcome the challenges I faced and he allowed space for me to develop solutions for the novel technology. Working with Dr. Kevin Musselman has been one of the best experiences in my life. Whenever I needed guidance and advice, he was ready and patient to help.

I would like to thank Neil Griffett, the electronics technician, of the Mechanical and Mechatronics Engineering Department at the University of Waterloo. His expertise and assistance with anything electronics related to my research were unparalleled. He has assisted in building the electrical panel and connections. I would also like to thank James Merli and Andy Barber, electronic technologists of the Mechanical and Mechatronics Engineering Department at the University of Waterloo. Andy had provided critical insights on new component selections for safety requirements, while James assisted significantly in ensuring the electrical designs and connections meet Canadian Standards Association (CSA) requirements.

I would like to thank Richard Forgett, Mark Kuntz, Phil Laycock, Fred Bakker, Rob Kraemer, and Jorge Cruz, from the Engineering Machine Shop at the University of Waterloo, for their expertise and assistance with fabricating the mechanical parts for my research. My project would not have been possible without their support.

I also owe my deepest gratitude and appreciation to my colleagues: Jhi Yong Loke (a current MAsc student under Dr. Kevin Musselman's group) and Manfred Kao (a past MAsc student under Dr. Kevin Musselman's group). Jhi Yong has been working closely

with me on the mechanical design aspects of my research and all the testings, setups, and assemblies, while Manfred has been very helpful with electrical design, programming, and system design. I genuinely enjoy the stimulating discussions, the sleepless nights, and all the fun we have had in the past two years.

Lastly, I must thank my wife, friends, and family for their unconditional love and support throughout my academic journey. I would not be in the position I am today if it weren't for them.

Table of Contents

Author’s Declaration	ii
Abstract	iii
Acknowledgements	iv
List of Figures	ix
List of Tables	xvii
1 Introduction	1
1.1 Atomic Layer Deposition and its Applications	2
1.2 Atmospheric Pressure Spatial Atomic Layer Deposition (AP-SALD): A Path Towards Industrialization of Atomic Layer Deposition	7
1.3 Existing Lab-scale AP-SALD system	12
1.4 Motivation for AP-SALD	15
1.5 Engineering Specifications of an Industrial-Scale AP-SALD System	17

1.6	Thesis Overview	19
2	Design and Construction of a Pilot-Scale Industrial AP-SALD System	20
2.1	Exhaust Cabinet Sub-system	24
2.2	Gas Sub-system	29
2.3	Reactor Head Sub-system	32
2.4	Heating Sub-system	46
2.5	Linear Stage Sub-system	53
2.6	Control Sub-system	63
3	Testing Results and Discussion	67
3.1	Linear Stage Movement Test	68
3.2	Substrate Suction Test	71
3.3	Substrate Heating Test and Linear Stage Temperature Monitoring	73
3.4	Reactor Head Flatness Check, Substrate Stage Leveling, Auto-leveling	76
3.5	Leak Test on Gas Sub-system	81
3.6	Flow Test on Reactor Head Sub-system	85
3.7	System Level Testing and Safety	87
3.8	Film Deposition Test and Performance Validation	89

4	Conclusions	93
4.1	Future Work	96
	References	98
	APPENDICES	104
A	Design and Construction of a Pilot-Scale Industrial AP-SALD System	105
A.1	CFD Simulations of Reactor Head	106
A.2	PID Block Diagram for Temperature Control	108
A.3	Motion Simulations of the Linear Stage	110
A.4	Electrical Components of AP-SALD System	111
A.5	AP-SALD Human Machine Interface (HMI)	113

List of Figures

1.1	A representation of ALD showing two self-limiting surface reactions	3
1.2	A diagram showing a ALD cycle with DEZ as metal source and H ₂ O as oxygen source (oxidant), obtained from Manfred Kao with his permission. . . .	4
1.3	A model of Applied Materials Gen-10 PECVD system (AKT 90K CVD) used for deposition of silicon-based films for flat panel displays. The system consists of up to five process chambers, each capable of processing ~9 m ² large glass substrates. Courtesy of Jozef Kudela.	6
1.4	A diagram showing the difference between ALD and AP-SALD. (a) In conventional ALD, different precursor gases are exposed at different time. (b) In AP-SALD, different precursors gases are exposed at the same time but are separated in space.	7
1.5	Schematic illustrations of spatial atomic layer deposition techniques based on (a) circulating flexible substrates, (b) rotating substrate cylinders, and (c) linear “zone-separated” precursor regions. All approaches spatially isolate precursor gases A and B from one another. Reproduced from [1].	8

1.6	A schematic illustration of the production of precursor gases, obtained from Manfred Kao with his permission.	9
1.7	(a) AP-SALD reactor with alternating flows of precursor gases. (b) The substrate first moves underneath precursor A, absorbing a monolayer of the precursor, and then through the purging, inert (I) gas flow. (c) The substrate then moves underneath precursor B, which reacts with A to form a monolayer of the desired material. Reproduced from [1].	10
1.8	A photo of Dr. Kevin Musselman’s lab-scale AP-SALD at the University of Waterloo	13
1.9	A schematic of Dr. Kevin Musselman’s lab-scale AP-SALD at the University of Waterloo.	13
1.10	The deposition process of Dr. Kevin Musselman’s lab-scale AP-SALD at the University of Waterloo.	14
1.11	Schematic illustrations of some established open-air nanoscale deposition techniques. Reproduced from [1].	15
2.1	A 3D model of the pilot-scale industrial AP-SALD system.	21
2.2	The pilot-scale industrial AP-SALD system in Dr. Kevin Musselman’s lab at the University of Waterloo.	23
2.3	The positions of the three filter fan in 3D CAD.	25
2.4	A picture of the shroud connection from the third filter fan to the fume hood.	26

2.5	(a) Metal precursor bubbler made up of stainless steel (b) Water precursor bubbler made up of polycarbonate.	30
2.6	A picture of SMC SS0750 pneumatic manifold with EX260 serial transmission system.	30
2.7	(a) 3D design of the bubbling panel in Siemens NX for planning, photo credited to Jhi Yong Loke (b) the actual setup of the bubbling panel.	31
2.8	An isometric view of the modular reactor head, which can be equipped with heating channels, cooling channels, plasma enhancers, and other components. The inlet ports are on both ends of the slit, where the flow comes in from both sides. The rods are used to hold the slits together.	32
2.9	Detailed view of one possible arrangement for the modular reactor head	33
2.10	A 3D model of the flow region based on the reactor head design shown in Figure 2.9.	34
2.11	A 3D CFD simulation result based on parameters in Table 2.1. Black lines represents precursor A while red lines represents precursor B. White lines are nitrogen.	35
2.12	A 2D CFD simulation result based on the same 3D simulation parameters.	36
2.13	The CFD result of flow velocity across the slit shown in Figure 2.18	37
2.14	(a) A side view of a reactor head component and the interspaced elevation adjustment between two components. (b) A front view of the reactor head with adjustable interspaced elevations for different reactor components. (c) An isometric view of the reactor head.	39

2.15	A side view of the cooling channel and the placement of the cooling channels beside the precursor gas components.	40
2.16	An example of a plasma channel integrated with the reactor head.	41
2.17	The front and bottom views of a scalable reactor head design.	41
2.18	A perspective view of the reactor slit design that can be modified to produce uniform flow.	42
2.19	The actual setup of the reactor head with linear actuators and laser sensors.	43
2.20	An illustration of a positioning system of the reactor head to the heating stage.	45
2.21	(a) A view of the heating stage with a vacuum holding mechanism. (b) An example of substrate placement configuration with four 225 cm ² substrates.	47
2.22	A picture of the customized heating element.	48
2.23	A picture of the actual heating stage setup.	49
2.24	A picture of the heater's controller box	50
2.25	A screenshot of PID parameters configured by Siemens PLC through its pretuning and fine-tuning programs. Only the heating has been configured.	52
2.26	(a) The setup of Akribis linear stage with granite slab only. (b) The setup of the linear stage with heating stage and vacuum reservoir.	53
2.27	An overview of the connections among Siemens PLC, Galil DMC motion controller, Kollmorgen AKD servo drive, and Akribis stage.	54

2.28	A picture of the actual setup of Galil DMC controller and Kollmorgen AKD servo drive in the electrical panel.	55
2.29	A screenshot of Kollmorgen AKD's operating scope which shows the output continuous current is $1.785 A_{rms}$	57
2.30	A picture of the thermocouple's location at the coil unit of Akribis stage. . .	58
2.31	A schematic of the uniform velocity region.	59
2.32	A schematic of the ideal motion profile.	59
2.33	The simulation result in Tecnotion with an uniform velocity of $1.348 \frac{m}{s}$ and an acceleration of $11.044 \frac{m}{s^2}$	62
2.34	The controllers, I/O modules, power supplies, and contactors used in the control system of AP-SALD.	64
3.1	The test result output from Kollmorgen AKD that showed the velocity and current versus the time when the linear stage oscillated at $1.35 \frac{m}{s}$	69
3.2	The placement of big substrates and small substrates during one of the substrate suction tests.	72
3.3	A picture of the heating test.	73
3.4	A screenshot of the response from the temperature controller from the heating stage.	74

3.5	A picture of assembling the reactor head on the substrate stage, where the channels were facing down on the flat surface to ensure the bottom of the reactor was perfectly flat.	76
3.6	The locations of three laser sensors.	77
3.7	A plot of the stage's flatness profile based on three laser sensors' readings across the 600 mm long stage.	78
3.8	A picture shows the placement of spacers used to offset the heating stage from the vacuum reservoir.	78
3.9	(a) The reading of laser sensors when they were in range. (b) The reading of laser sensors after the spacing was adjusted to the 0.125 mm set point. . .	79
3.10	A 0.1 mm shim was used to check the spacing.	80
3.11	A schematic of the bubbling panel with the MFCs removed and a flow meter attached for the leak test.	81
3.12	MFCs were dismantled from the bubbling panel for the leak test.	82
3.13	(a) The position of the ball indicator if the lines stay pressurized. (b) The position of the ball indicator if there is a leak in the line.	83
3.14	There was a minor leakage at the water bubbler.	84
3.15	A bottom view of the actual reactor.	86
3.16	Pressure issue with one MFC for water carrier line.	88
3.17	The first film made with the pilot-scale industrial AP-SALD system.	90

3.18	The uniform film made with the pilot-scale industrial AP-SALD system.	91
A.1	A 3D CFD simulation result with same parameters as shown in Table 2.1, except reactor head-substrate spacing which 3mm is used in this case.	106
A.2	A 2D CFD simulation result with same parameters as shown in Table 2.1, except reactor head-substrate spacing which 0.45mm is used in this case.	107
A.3	A screenshot of the PID block diagram from Siemens PLC program for temperature control and process.	108
A.4	A screenshot of the PID block diagram with anti-windup from Siemens PLC program for temperature control and process.	109
A.5	Parameters for the simulation in Tecnotion.	110
A.6	The log-on page of HMI.	113
A.7	The home page of HMI.	114
A.8	The flow control page of HMI.	115
A.9	The stage control page of HMI.	116
A.10	The recipe overview page of HMI.	117
A.11	The heater's status interface of HMI.	118
A.12	The heater's control interface of HMI.	119
A.13	The heater's permissive and interlock interface of HMI.	120
A.14	The linear actuator's status interface of HMI.	121

A.15	The linear actuator's control interface of HMI.	122
A.16	The linear actuator's permissive and interlock interface of HMI.	123
A.17	The linear stage's status interface of HMI.	124
A.18	The linear stage's control interface of HMI.	125
A.19	The linear stage's permissive and interlock interface of HMI.	126
A.20	The MFC's status interface of HMI.	127
A.21	The MFC's control interface of HMI.	128
A.22	The MFC's permissive and interlock interface of HMI.	129
A.23	The valve's status interface of HMI.	130
A.24	The valve's control interface of HMI.	131
A.25	The valve's permissive and interlock interface of HMI.	132
A.26	The laser sensors' reading on the HMI before auto-leveling is commanded. .	133
A.27	The laser sensors' reading on the HMI after auto-leveling is commanded. . .	134
A.28	A screenshot of flow reading vs. setpoint of mass flow controller from HMI.	135

List of Tables

1.1	A list of some of the smallest film thickness resolutions reported by open-air nanoscale deposition techniques.	16
2.1	The CFD's modeling parameters of the reactor head	34
2.2	The definition of variables used in Equation 2.1 and associated parameters used in block diagram shown in Figure A.3 and Figure A.4 in Appendix A.	51
2.3	The definition of variables for the velocity profile.	60
2.4	The required time for uniform velocity and acceleration.	61
3.1	The calculation of root means square of the current of the linear stage during the oscillation.	69
3.2	The parameters used for the first film deposition on a 150 mm x 150 mm x 2 mm borosilicate glass.	89
3.3	The parameters used for the uniform film deposition on a 150 mm x 150 mm x 2 mm borosilicate glass.	91
A.1	The electrical components used in the AP-SALD system.	111

A.2 The functions of each interface designed in the HMI. 136

Chapter 1

Introduction

1.1 Atomic Layer Deposition and its Applications

Techniques such as sputtering, evaporation, and chemical vapor deposition are used to deposit thin films for many applications (e.g. all modern electronics, optical components, display technologies, food packaging, etc.). Better and better control over the film thickness and quality is needed. For example, 2019 corresponds to the 5nm node on the International Technology Roadmap for Semiconductors, suggesting that semiconductor manufacturers should be developing components with feature sizes of 5 nanometres. Atomic layer deposition (ALD) is the best technique for producing films with nanometre-scale thickness control, as it deposits a film one atomic layer at a time. ALD has emerged as an important thin film deposition technique to create continuous, conformal and pin-hole free films on complex three-dimensional surfaces using sequential, self-limiting surface half-reactions [2, 3].

Most ALD processes are based on binary reaction sequences, where two surface reactions occur and deposit a binary compound thin film. The reactions can only deposit on a finite number of surface species because there are only a finite number of surface sites. Unlike chemical vapor deposition (CVD) and other similar deposition techniques, the precursors are not introduced simultaneously in ALD. Two self-limiting surface reactions proceed in a sequential fashion to deposit thin films with atomic-level control as shown in Figure 1.1 [2].

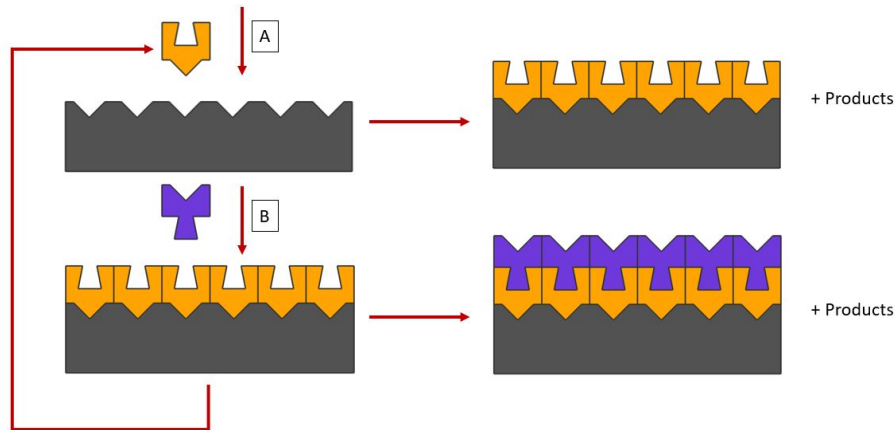


Figure 1.1 A representation of ALD showing two self-limiting surface reactions

In the ALD process, two precursors are usually used in depositing metal oxide films; one of which is the metal source and the other one is the oxygen source [4]. The precursors are injected into a vacuum chamber, where a substrate is placed and is heated to promote the chemical reactions [5]. Precursor gases are highly reactive gases that are created by bubbling inert gas such as argon or nitrogen through the volatile precursor liquid source. The chemical reactions between the precursors are activated at the substrate, commonly thermally or using plasma. A purge step is required in between each exposure of different precursors to remove any excess chemicals that do not bind to the substrate and prevent them from reacting in the chamber. The steps of an ALD cycle for producing a monolayer of material on a substrate are as follows [6]:

1. Introduce the first precursor in the reactor chamber to form a layer on the substrate by saturating the substrate's surface sites.
2. Purge any excess first precursor and by-products.
3. Introduce the second precursor to react with the first precursor molecules on the substrate.

4. Purge or evacuate any excess second precursor and by-products.
5. Repeat Step 1 - 4 until the required film thickness is achieved.

Figure 1.2 illustrates the process of zinc oxide deposition using ALD. Diethylzinc (DEZ) and water are commonly used as the precursors to deposit inorganic zinc oxide thin films. Equation 1.1 shows a simplified reaction mechanism between DEZ and H₂O, and a more in-depth explanation of the ALD reaction can be found in [7].

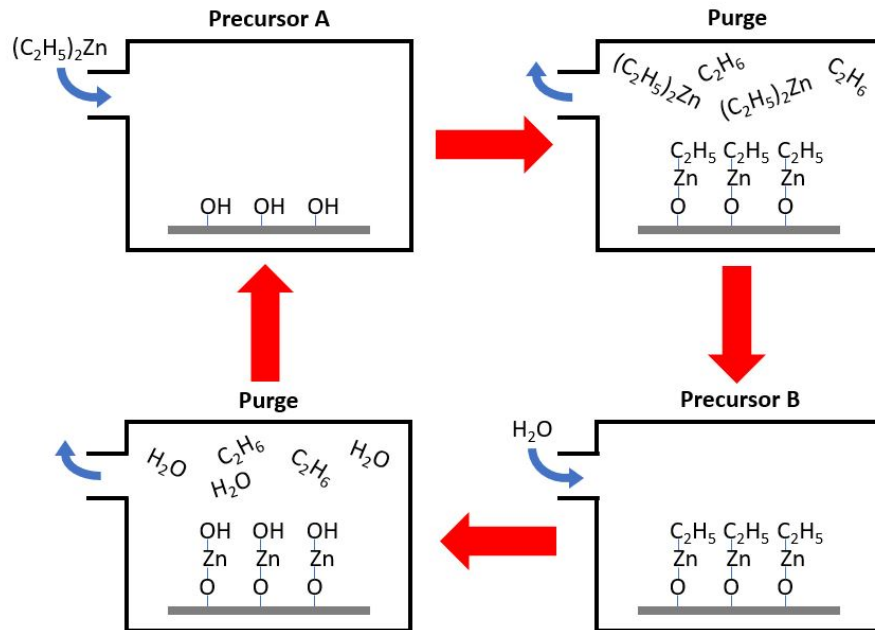
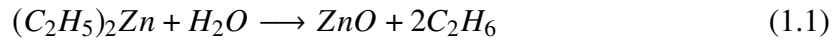


Figure 1.2 A diagram showing a ALD cycle with DEZ as metal source and H₂O as oxygen source (oxidant), obtained from Manfred Kao with his permission.

As feature sizes continue to decrease in integrated circuits and memory devices, ALD is becoming the only option for depositing some thin-film components. A thin film can

be defined as a layer of materials with a thickness ranging from nanometres to several micrometres. ALD has been proven to be a popular and powerful tool in many fields such as the semiconductor industry, where it enables the design of smaller devices with better performance and energy efficiency [8–10]. Application of ALD thin films in fabricating batteries has also been reported to improve the energy density, long-term stability, and durability of the batteries [11–15]. The role of ALD thin films in photovoltaic applications includes absorber films, buffer layers, interface layers, transparent front contacts, photoanodes, encapsulation layers and surface passivation films [16]. When the challenges of cost and throughput are solved, ALD is a promising alternative to present established technologies since it possesses advantages such as easy production and higher flexibility [17–21]. Thin films have applications in medicine and medical devices as well, for instance, they can reduce the size of medical devices, improve their functionalities, and make the medical tools more durable [22, 23]. Furthermore, a number of functional thin-film materials have been identified to have antiviral effects, including copper, brass, zinc, copper oxide, zinc oxide, silver, and combinations thereof [24–33]. In a more timely note, some initial studies have suggested that the lifetime of the COVID-19 virus is reduced on copper surfaces [24].

Although ALD has been proven to be useful with many applications in a broad range of industries, it has its drawbacks. Weaknesses associated with ALD include its speed (it is a relatively slow process) and the need for a vacuum chamber, which limit its throughput and scalability respectively. Companies are working to scale the ALD process by using larger chambers; however, it remains a slow batch process. This is not necessarily an issue for some industries (e.g., integrated circuits and photovoltaics where wafers can be processed in batches) but prevents its use in other applications (e.g., roll-to-roll manufacturing for flexible electronics). Thin-film deposition equipment has to scale with the application and production throughput, which commonly leads to a truly gigantic tool, such as a PECVD system from Applied Materials with up to five process chambers that is used for depositing

silicon-based films on $\sim 9 \text{ m}^2$ large glass substrate for flat panel displays as shown in Figure 1.3.

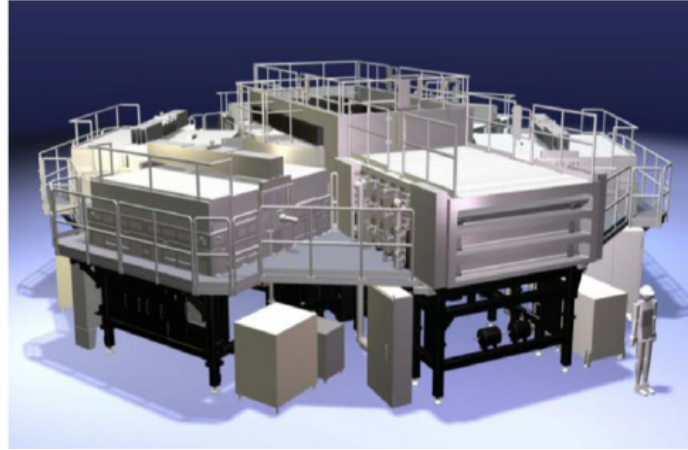


Figure 1.3 A model of Applied Materials Gen-10 PECVD system (AKT 90K CVD) used for deposition of silicon-based films for flat panel displays. The system consists of up to five process chambers, each capable of processing $\sim 9 \text{ m}^2$ large glass substrates. Courtesy of Jozef Kudela.

1.2 Atmospheric Pressure Spatial Atomic Layer Deposition (AP-SALD): A Path Towards Industrialization of Atomic Layer Deposition

Conventional ALD operates by sequentially inserting two chemical precursor gases into a vacuum chamber, with evacuation and purge steps in between the exposures. An atomic layer of the material is formed after each sequence, and the sequence is repeated multiple times to build up a film. Hence, conventional ALD separates the two precursor gases in time.

In contrast, spatial atomic layer deposition (SALD) techniques have been developed, which separates the two precursors in space rather than in time. The substrate is moved back and forth between the two precursor gases to replicate the sequential exposures. This approach eliminates the evacuation and purge steps that make ALD slow. Figure 1.4 illustrates the difference between ALD and AP-SALD.

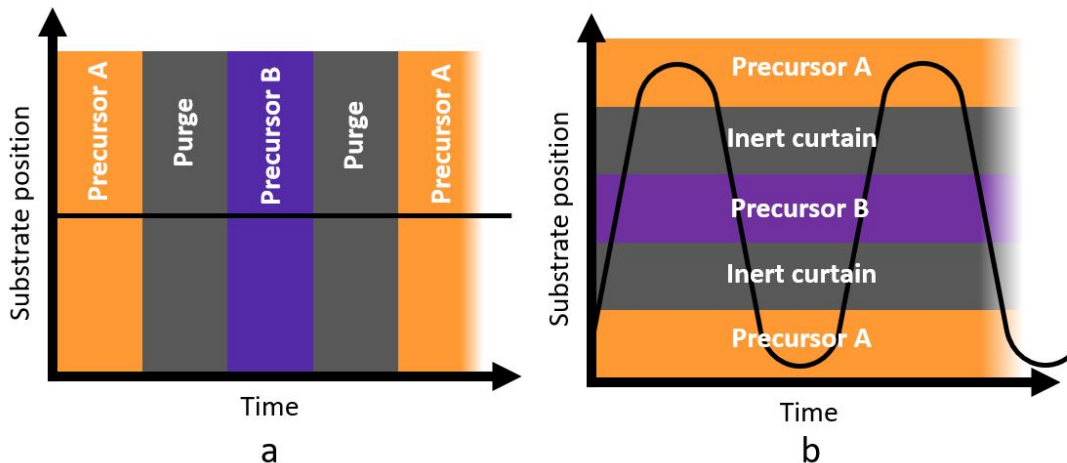


Figure 1.4 A diagram showing the difference between ALD and AP-SALD. (a) In conventional ALD, different precursor gases are exposed at different time. (b) In AP-SALD, different precursor gases are exposed at the same time but are separated in space.

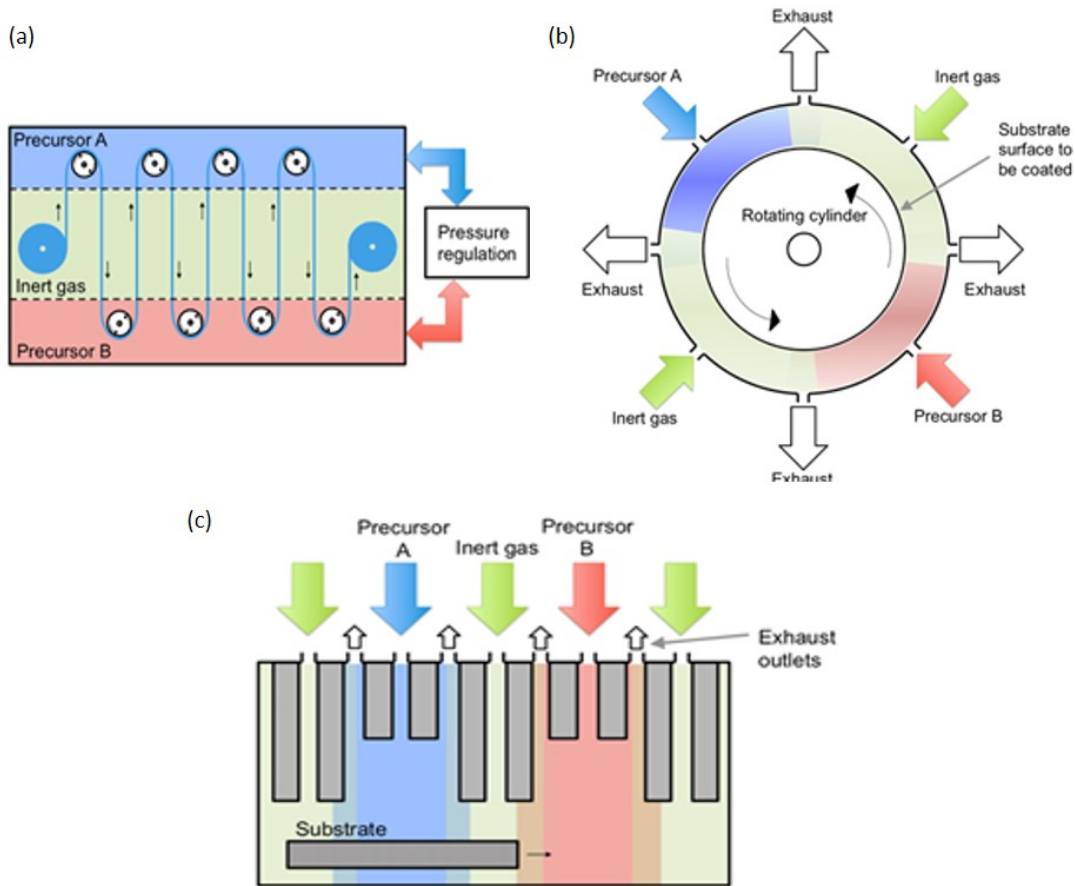


Figure 1.5 Schematic illustrations of spatial atomic layer deposition techniques based on (a) circulating flexible substrates, (b) rotating substrate cylinders, and (c) linear “zone-separated” precursor regions. All approaches spatially isolate precursor gases A and B from one another. Reproduced from [1].

There are several SALD approaches, such as circulating flexible substrates, rotating substrate cylinders, and linear "zone-separated" gaseous precursor regions, as illustrated in Figure 1.5 [1].

The SALD approach shown in Figure 1.5 (c) places the substrate very close (~100 micrometers) to a reactor head that contains parallel channels (which are very close to each other, often only a few millimeters apart) with flows of the two precursor gases. The small space between the parallel channels, as well as the reactor and substrate, combined with inert nitrogen gas curtains and exhaust channels, can keep the precursor gases separated and

isolated from the surrounding air, without the need for vacuum equipment. Similar to ALD, the precursor gases are produced by bubbling an inert gas through a volatile precursor liquid. The vaporized precursor leaves the bubbler and combines with an inert carrier line, which is then supplied to a reactor head (see Figure 1.6 for a diagram).

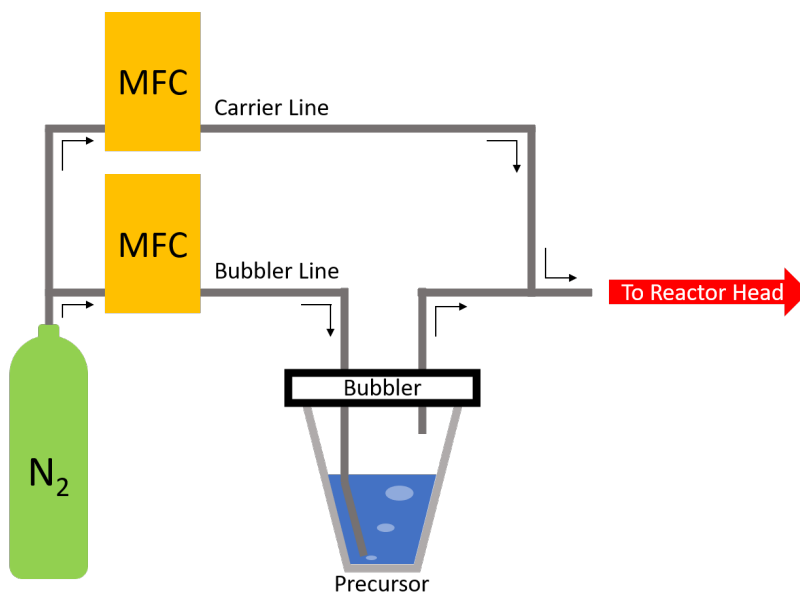


Figure 1.6 A schematic illustration of the production of precursor gases, obtained from Manfred Kao with his permission.

The substrate is oscillated back and forth underneath the reactor to replicate the sequential exposure steps and deposit a film one atomic layer at a time. This approach does not require a chamber or vacuum equipment, which makes it scalable and less costly. Since it operates in atmospheric conditions, it is often referred to as atmospheric pressure spatial ALD (AP-SALD).

AP-SALD can produce thin-film layers of materials (typically metal oxides) that are compact and pinhole-free. AP-SALD can deposit thin films at low temperatures (typically from 100 to 350°C), is 1-2 orders of magnitude faster than conventional ALD, and is scalable (roll-to-roll compatible). AP-SALD has been demonstrated on glasses, semiconducting wafers, foils, and plastic surfaces. These advantages make AP-SALD very attractive for

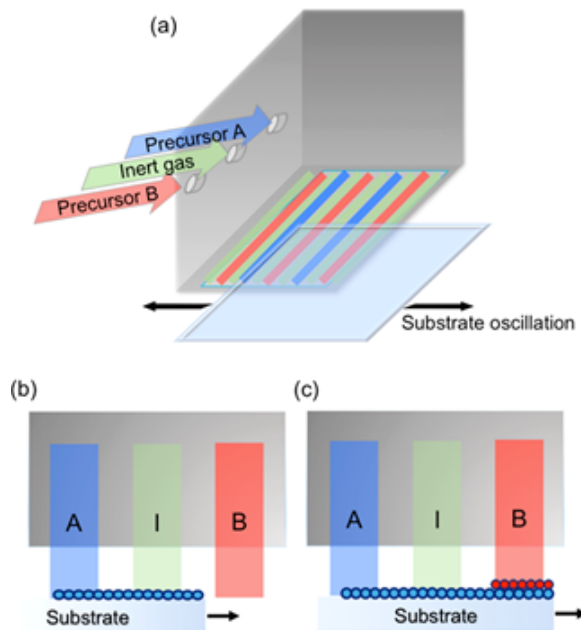


Figure 1.7 (a) AP-SALD reactor with alternating flows of precursor gases. (b) The substrate first moves underneath precursor A, absorbing a monolayer of the precursor, and then through the purging, inert (I) gas flow. (c) The substrate then moves underneath precursor B, which reacts with A to form a monolayer of the desired material. Reproduced from [1].

high-throughput manufacturing of large-area, low-cost electronics, such as photovoltaics, batteries, and microelectronics.

The development of next-generation photovoltaics, such as perovskite solar cells and heterojunction solar cells, requires a new manufacturing method to explore new ways of fabricating thin films for different layers in the solar cells at low cost and high throughput with high quality. AP-SALD is a good technique that can create thin films without defects and at low temperatures which enables the fabrication of thin film solar cells on temperature sensitive substrates such as polymers [34]. Since AP-SALD can operate at atmospheric condition and low temperatures, it is relatively easy to be integrated with other processes to make next-generation photovoltaics [35].

In the battery industry, new ways are always being explored to improve existing battery architectures, safety, and performance, as well as to research and develop next-generation batteries such as solid-state batteries. The current trend of applying thin-film coatings on batteries involves coating one of the electrodes - the cathode [36]. Using AP-SALD, barrier

layers can be coated directly on the cathode electrode instead of the powders to provide the same functionality [37]. Furthermore, AP-SALD is particularly useful for the R&D of 3D all-solid-state batteries, micro-batteries, and thin-film batteries that are made out of solid components (electrodes, separators, electrolytes, collectors) [38–40].

3D formable and stretchable transparent conductive films and touch sensors have many applications in industries such as automotive, consumer electronics, semiconductors, medical diagnostics, and stretchable displays. In-mold electronics require thin films that are transparent and conductive. The film needs to be formable and flexible, enabling 3D touch surfaces and 3D heater solutions. AP-SALD is compatible with a wide range of substrates and high throughput roll-to-roll manufacturing. This approach allows thin films to be made on flexible substrates at low temperature and atmospheric pressure. Hence, AP-SALD can enable the fabrication of plastic components with functional surfaces.

1.3 Existing Lab-scale AP-SALD system

Canada's first lab-scale AP-SALD system was built in Dr. Kevin Musselman's lab at the University of Waterloo in 2018. It was developed based on the close-proximity design discussed above. This system serves as a proof-of-concept that has demonstrated the advantages of AP-SALD for producing high-quality thin films at higher deposition rates. This technique has improved the performance of devices such as metal-insulator-metal (MIM) diode [41]. The system is also equipped with in situ reflectance spectroscopy to measure the properties of thin films during the deposition [42]. Figure 1.8 shows the existing lab-scale AP-SALD system that was built by co-op and graduate students from the University of Waterloo. The simplified schematic of the AP-SALD shown in Figure 1.9 illustrates how the precursors are being bubbled and directed to the reactor head for deposition.

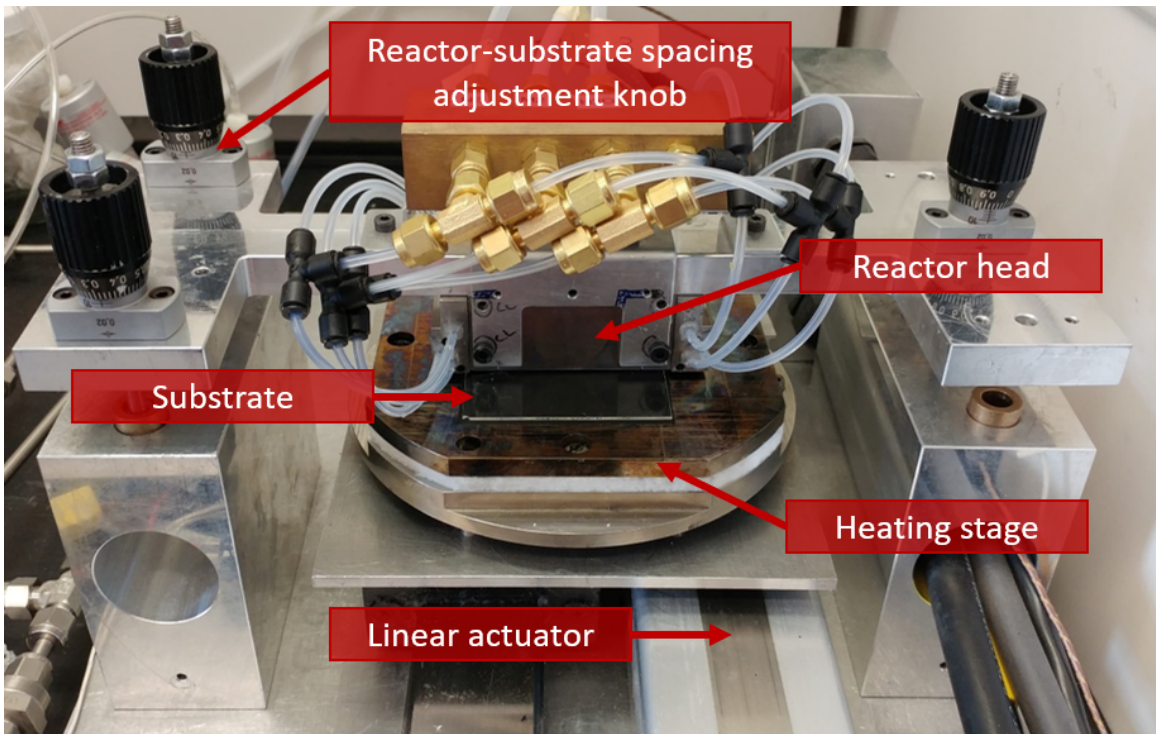


Figure 1.8 A photo of Dr. Kevin Musselman's lab-scale AP-SALD at the University of Waterloo

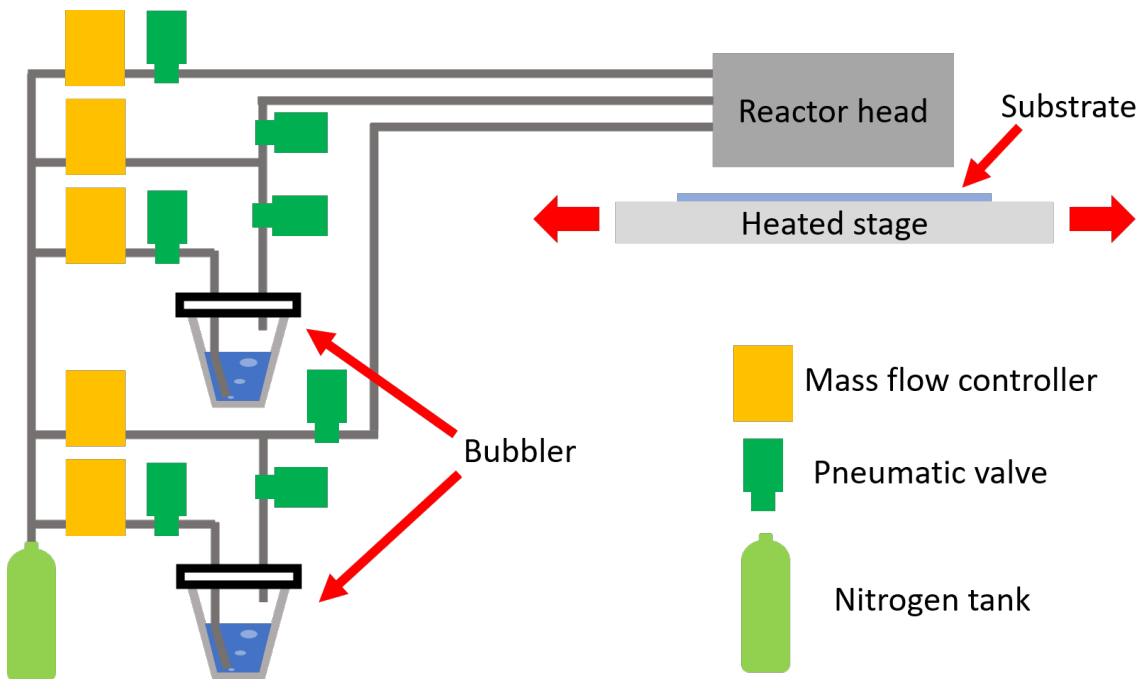


Figure 1.9 A schematic of Dr. Kevin Musselman's lab-scale AP-SALD at the University of Waterloo.

The lab-scale AP-SALD is capable of depositing films that are 50 mm wide and 50 mm long. It is designed to coat small sample sizes for experiment purposes. Figure 1.10 shows the deposition process of the actual lab-scale AP-SALD system, where the liquid precursors are being bubbled and delivered to the reactor. The substrate oscillates under the reactor on a heated stage. An image of a 144.6 nm uniformly thick Zinc oxide film deposited with the AP-SALD system on a borosilicate glass is shown in Figure 1.10 (d).

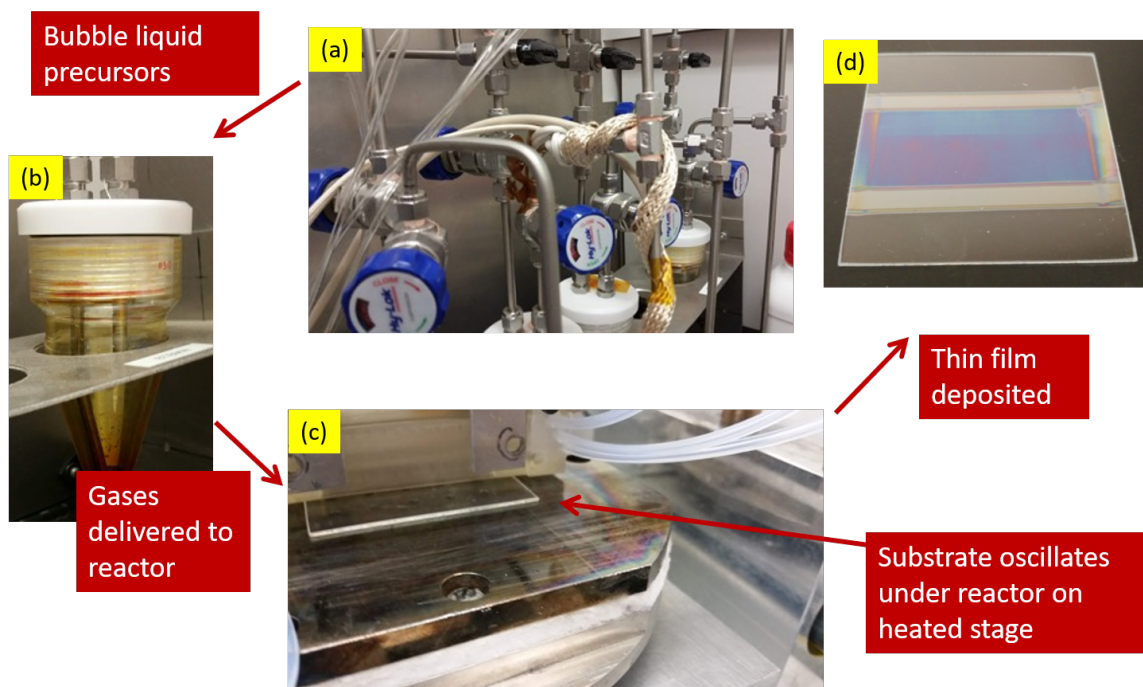


Figure 1.10 The deposition process of Dr. Kevin Musselman's lab-scale AP-SALD at the University of Waterloo.

1.4 Motivation for AP-SALD

Traditional thin film deposition techniques, such as sputtering, evaporation, chemical vapor deposition, and atomic layer deposition, can provide precise control over the film properties and thickness, but they have several disadvantages that limit their development and scalability. These traditional techniques require a reactor chamber with low pressure environment to operate, which make them expensive for wide industrial adoption. These traditional technique are slow with a deposition rate of nanometers per minute, which limit their capability for high throughput manufacturing.

Other establish open-air nanoscale deposition techniques include gravure printing, screen printing, knife-over-edge coating, slot-die coating, inkjet printing, and spray deposition, which are illustrated schematically in Figure 1.11. These nanomanufacturing techniques are inexpensive, more scalable and compatible with roll-to-roll manufacturing. However, they have less control over the film properties and thickness [1].

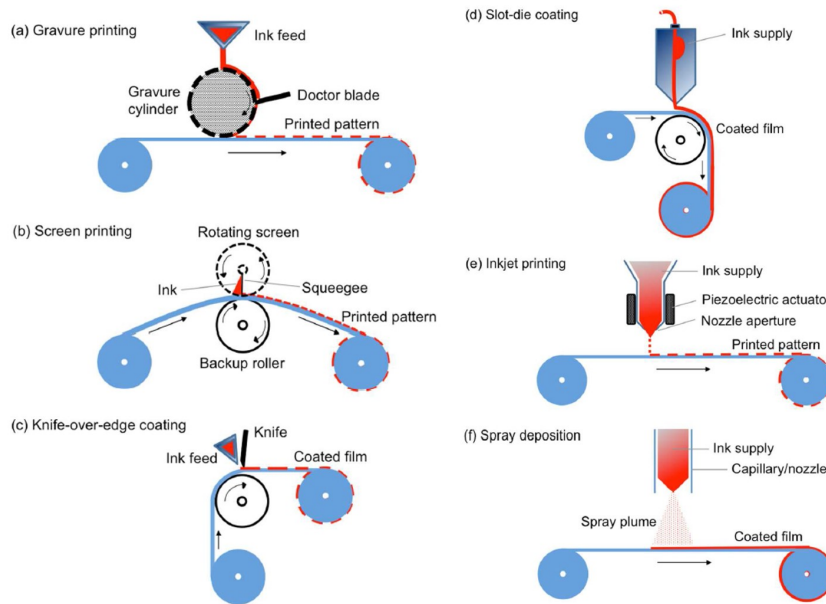


Figure 1.11 Schematic illustrations of some established open-air nanoscale deposition techniques. Reproduced from [1].

Table 1.1 lists some of the smallest film thickness resolutions reported by open-air nanoscale deposition techniques (sourced from [1]). It is seen that of the currently available scalable, open-air, thin-film deposition techniques, AP-SALD has a clear advantage in terms of its ability to deposit sub-10 nm films.

Table 1.1 A list of some of the smallest film thickness resolutions reported by open-air nanoscale deposition techniques.

Open-air film deposition technique	Minimum thickness resolution (nm)
Gravure printing	15-20
Screen printing	40
Knife-over-edge coating	20
Slot die coating	28
Inkjet printing	70
Spray coating	10
AP-SALD	<5

As compared to some of these printing techniques, AP-SALD offers multiple advantages [1]:

- It produces continuous, conformal coatings with pin-hole free and few defects.
- It requires low deposition temperature for the deposited materials.
- It facilitates tuning of material properties.
- It provides atomic-scale thickness control.

1.5 Engineering Specifications of an Industrial-Scale AP-SALD System

SolayTec and Levitech are global players that have a leading position in the field of solar cell ALD equipment. They have previously developed SALD for coating Al_2O_3 passivation layers on silicon photovoltaics. They use gas bearings to float a silicon wafer through different precursor zones for deposition. However, the air bearing setup has several disadvantages:

- The system is tailored for a specific substrate size and weight (less flexible).
- The control of the reactor-substrate spacing is likely more challenging (based on a careful balance of gas flows and substrate weight vs. mechanical positioning).
- A substrate is not heated during the deposition (heated beforehand) which limits the duration of the deposition (substrate will gradually cool) and hence the achievable film thickness.

Kodak, a global technology company focused on print and advanced materials and chemicals, has also developed spatial ALD technology and filed several patents. They similarly make use of gas-bearing technology to position the substrate, which has the same disadvantages as SolayTec and Levitech. Their patented design is based on the linear translation of the substrate through the precursor regions such that film thickness is defined by the number of precursor zones. This constraint makes their design less flexible and not as well suited to deposit thicker films because many precursor zones would be required.

A number of research labs around the world are developing lab-scale SALD technology, but these AP-SALD systems are designed for coating small area ($< 5\text{cm} \times 5\text{cm}$) films.

Our objective was to develop a commercial-scale AP-SALD system with a variety of features:

- Ability to deposit controlled nanoscale films (including sub-10 nm films as well as films >20 nm thick with 1 nm resolution).
- Ability to deposit over large areas (i.e. above 15 cm x 15 cm).
- Modular design to allow scaling for high throughput (above 3000 substrates/ hr).
- Capacity to deposit different materials (e.g., SnO₂, WO₃, Al₂O₃, AZO. . .).
- Operate with a wide range of substrate types, thickness, and geometries.
- Designed for industrial standards mechanically and electrically.
- Capacity to deposit films with thickness and composition gradients for:
 - Rapid prototyping of devices with nanoscale thin films.
 - Nanoscale coatings with novel functionality.

1.6 Thesis Overview

In this paper, the design and construction of a pilot-scale industrial AP-SALD system will be discussed in detail in Chapter 2. Testing results and discussion to validate the performance of different sub-systems will be outlined in Chapter 3. Conclusions and areas for future work will be addressed in Chapter 4.

Chapter 2

Design and Construction of a Pilot-Scale Industrial AP-SALD System

A pilot-scale industrial AP-SALD system was designed and built from the ground up at the University of Waterloo in Dr. Kevin Musselman's lab. The new system was developed based on the lessons learned from the existing lab-scale AP-SALD system and the engineering specifications required for industrial performance discussed in Section 1.5 of Chapter 1. I designed and built the pilot-scale industrial AP-SALD system shown in Figure 2.2 with Jhi Yong Loke (MAsc student), and with the help and support from Dr. Kevin Musselman, Manfred Kao, the engineering machine shop, electronics technical staff, and suppliers.

My contributions to the development of the AP-SALD system included the conceptualization of the mechanisms, the preliminary design of the industrial AP-SALD system, the selection of mechanical and electrical components, the design and simulation of the first version of the reactor head assembly, the design and fabrication of mechanical parts and electronics, the frameworks and algorithms of the automated system operations, the software, the human

machine interface (HMI) and project management. Jhi Yong and I worked closely on fine-tuning and optimizing the design and fabrication of mechanical parts and assembly. He took the lead in the design of the heating stage and vacuum reservoir, which was one of the most challenging mechanical design pieces of the AP-SALD system. Neil from the electronics shop has helped with building the electrical panel and setting up the electrical connections. Figure 2.1 shows the 3D model of the AP-SALD system.

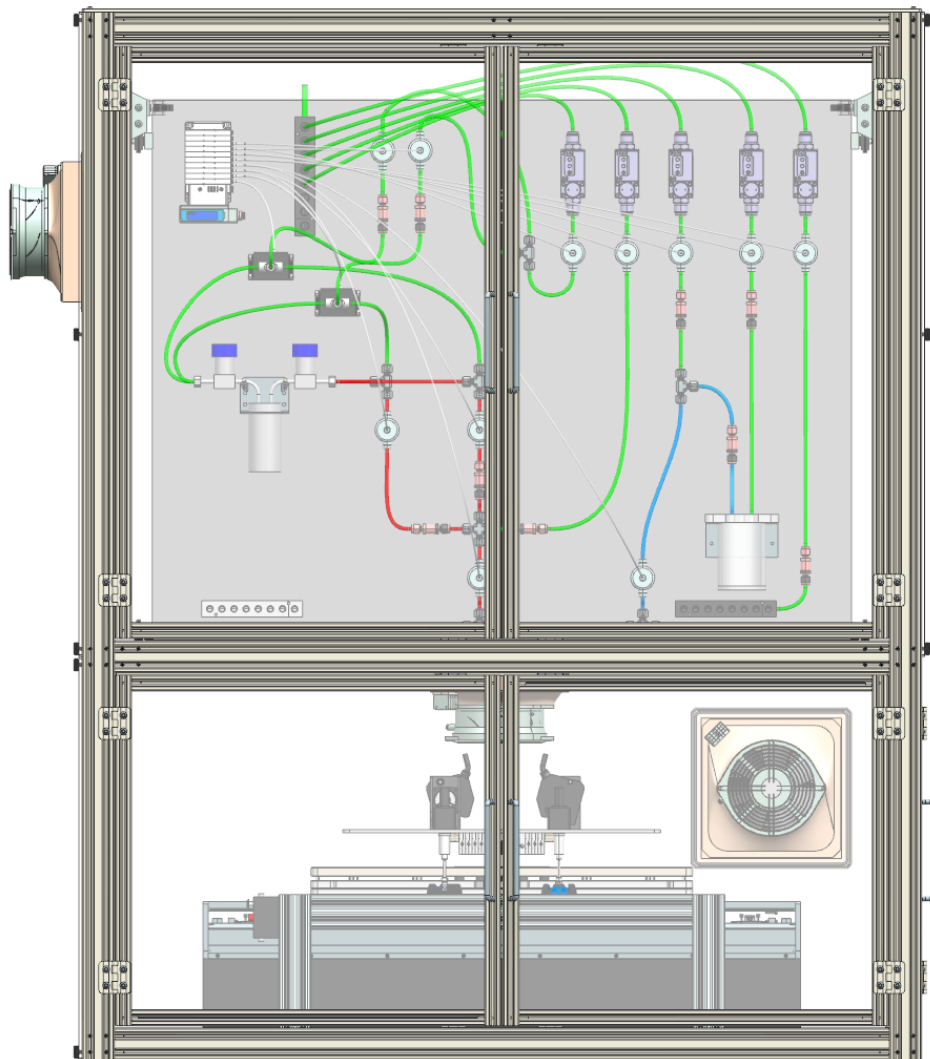


Figure 2.1 A 3D model of the pilot-scale industrial AP-SALD system.

The system can be broken down into three different sections, which are the bubbling section, deposition section, and electronics section. Figure 2.2 is the actual pilot-scale AP-SALD that

was built in Dr. Kevin Musselman's lab, which shows the bubbling section and deposition section. Each section consists of different sub-systems. The bubbling section includes the exhaust cabinet sub-system and gas sub-system. The exhaust cabinet sub-system consists of a cabinet and three exhaust filter fans to provide continuous ventilation and prevent the built-up of any harmful gases. The gas sub-system includes the equipment required to create the gases of the precursor chemicals, control the flow rate and distribute the gases.

The deposition section includes the reactor head sub-system, heating sub-system, and linear stage sub-system. The reactor head sub-system consists of multiple gases and exhaust slits stacked horizontally and a positioning system. The heating sub-system will heat substrates to a certain temperature to promote chemical reactions and hold substrates of any size, geometry, and thickness by the vacuum on the stage. The linear stage sub-system has a linear motor and a granite slab to provide high moving stage speeds for high deposition rates to ultimately achieve high throughputs.

The electronics system covers all the control sub-system. The control sub-system consists of an industrial controller with input/output (I/O) modules to communicate with various system components. All the sub-systems are discussed in the following sections.

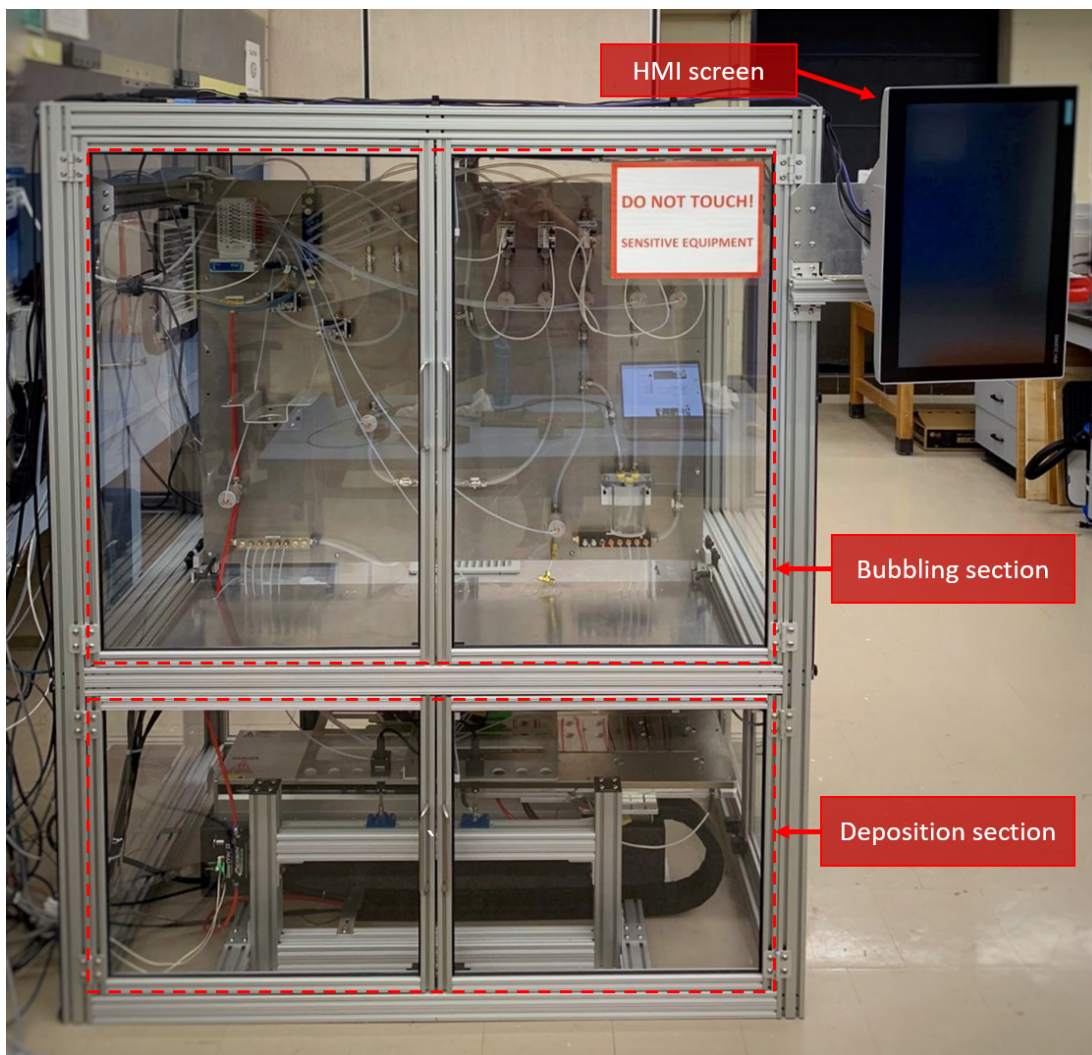


Figure 2.2 The pilot-scale industrial AP-SALD system in Dr. Kevin Musselman's lab at the University of Waterloo.

2.1 Exhaust Cabinet Sub-system

The system cabinet is provided with continuous exhaust ventilation by three 169 CFM filter fans to prevent the buildup of any harmful gases. The airflow in the cabinet is monitored (ifm SL5101 Airflow Monitor), as is the pressure in the exhaust line (VentAlert, a fume hood safety monitoring alarm system). The ifm SL5101 airflow sensor monitors the airflow inside the enclosure by detecting if there is any airflow drop from the calibrated airflow value. A Ventalert model WB86S device monitors the exhaust air system by checking for a negative air pressure condition within the exhaust duct. Both are interlocked to the gas sub-system to ensure the ventilation performance meets the NFPA 497 section 5.6.4 requirement for enclosed spaces of 6 air changes per hour. A hazardous area classification inspection is required to determine the electrical equipment ratings required (Ontario Electrical Code Section 18-002).

The positions of the three filter fans shown in Figure 2.3 are as follows:

1. The first filter fan is located at the lower chamber.
2. The second filter fan is located between the lower chamber and the upper chamber.
3. The third filter fan is located at the upper chamber near the fume hood.

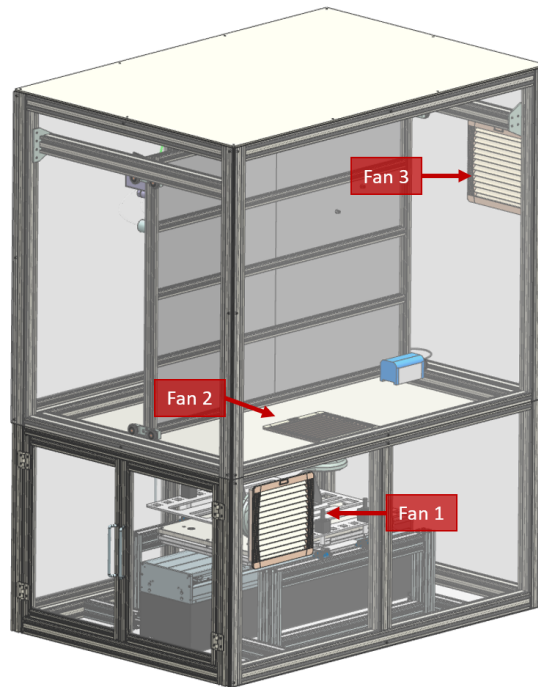


Figure 2.3 The positions of the three filter fan in 3D CAD.

The third filter fan is covered with a shroud and connected with a 6" duct hose to direct the exhaust air into the fume hood, as shown in Figure 2.4. The flow rate of the fume hood is approximately 3530 CFM, which was measured by Chris Ford, a Mechanical Engineering manager from Plant Operations at the University of Waterloo. The airflow of the fume hood is monitored by VentAlert, which is interlocked with our exhaust system and pneumatic manifold.

The following calculations were performed to determine the ventilation performance of the cabinet:

$$\text{Lower chamber volume: } 4 \text{ ft } (L) \times 2.62 \text{ ft } (W) \times 1.88 \text{ ft } (H) = 19.66 \text{ ft}^3$$

$$\text{Upper chamber volume: } 4 \text{ ft } (L) \times 2.62 \text{ ft } (W) \times 3.41 \text{ ft } (H) = 33.83 \text{ ft}^3$$

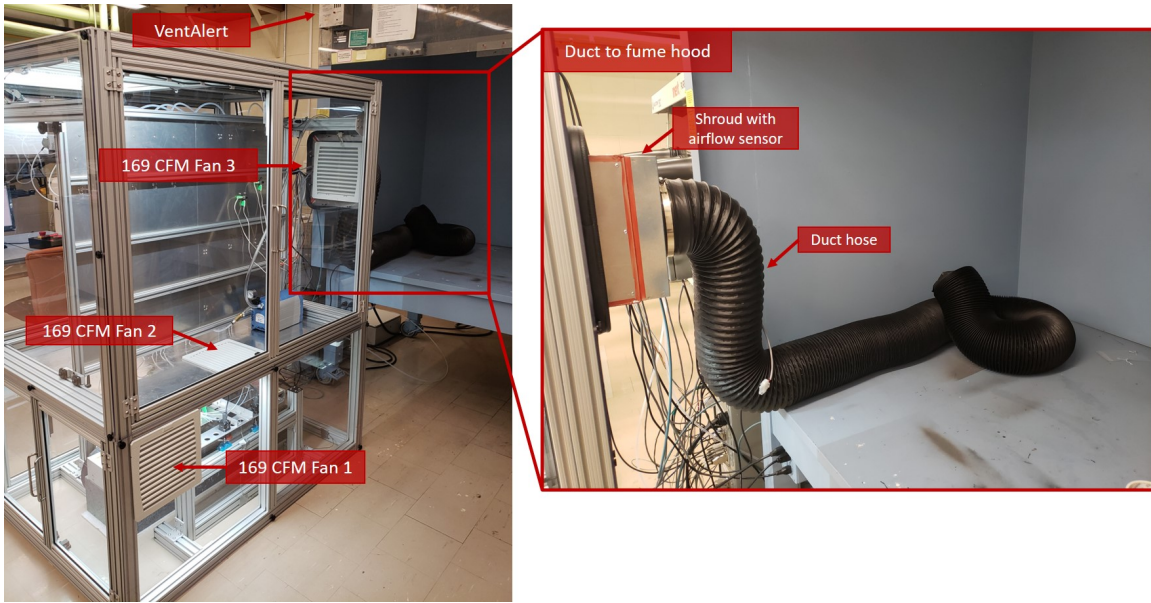


Figure 2.4 A picture of the shroud connection from the third filter fan to the fume hood.

The number of air changes per minute (lower section & upper section) :

$$\frac{169 \frac{ft^3}{min}}{19.66 ft^3 + 33.83 ft^3} = 3.16 \frac{air\ changes}{min}$$

The number of air changes per minute (lower section & upper section) :

$$3.16 \frac{air\ changes}{min} \times \frac{60min}{hour} = 189.6 \frac{air\ changes}{hour}$$

An air change rate of 189.6 per hour is well over the NFPA 497 section 5.6.4 requirement for enclosed spaces of 6 air changes per hour.

The ifm airflow sensor is installed inside the shroud of the exhaust fan near the fume hood. It does not sense actual flow, however it provides confirmation of negative pressure as a protection against a failure of the exhaust system fan or blockage of the duct. This device is powered by an external 24V power supply from the electrical panel and has a connection

with the audible (buzzer) and visual alarms (HMI display). The relay output from the sensor is connected to the digital input module of the programmable logic controller (PLC). When the flow is present, the relay is energized and closes the contact. In the event of an airflow failure:

- A warning sign of “airflow absence” is shown on the HMI display and an audible alarm sounds. This alarm may be silenced by a silence button on the HMI display.
- An electrical output turns on and supplies 24VDC, which is detected by the digital input on the PLC.
- The PLC detects the 24V signal drop through the module and disconnects all power to the filter fans and the pneumatic manifold (shut off all the pneumatic valves to cut chemical flow in the gas line shown in Section 2.2) in the event of loss of airflow.

VentAlert does not sense actual flow, however, it provides a confirmation of negative pressure as a protection against a failure of the exhaust system fan of the fume hood. This device is powered from an internal 9V battery, and has audible and visual alarms and an isolated 9VDC output (1mA capacity), which turns on in the event of a loss of flow. There is no external power source. In the event of an airflow failure:

- A warning LED flashes and an audible alarm sounds. A front-mounted push button may silence this alarm.
- An electrical output turns on. This output supplies 9VDC with a capacity of 1mA.

The Ventalert system also provides:

- A “low battery” indicator light.
- A test pushbutton to confirm that the unit is on and actuates the indicator lights and audible alarm signals.

To ensure that chemicals are dispensed only when airflow is on, a signal monitoring device is installed that uses the 9V 1mA output from the Ventalert to open its contact and drop the 24V signal to 0V. The signal drop is detected by a safety-rated digital input F-DI 8x 24 V DC HF module in the Siemens PLC panel. The connection among all the devices such as pneumatic manifold, filter fans, door lock, and mass flow controllers, were made within the PLC program. If the Ventalert senses a low flow condition, the PLC detects the 24V signal drop through the module and disconnects all power to the pneumatic manifold and filter fans in the event of loss of airflow. Both of these monitoring devices were interlocked to the gas sub-system.

2.2 Gas Sub-system

The gas sub-system includes the equipment required to create the gases of the precursor chemicals (bubblers, bubbler heaters), control the flow rate (mass flow controllers) and distribute the gases (valves, tubing, manifolds, etc.). All these components work together to perform several functions programmed in the PLC, such as purging (to fill lines with nitrogen gas at high flow rate), bubbling (to introduce precursor gases to the reactor head), idling (to fill lines with nitrogen gas at low flow rate), and turning off (to turn off all the flow). It is important to ensure the system starts with purging to fill all the lines with nitrogen gas because any oxygen in the lines will react with the metal precursor gas and form powder. The powder may clog the lines and affect the thin film deposition. The system will automatically switch to idling mode to continuously fill the lines with nitrogen at a lower flow rate to prevent atmospheric air from entering the lines. Before the deposition, the PLC will execute the bubbling program, which directs the nitrogen flow into the metal precursor bubbler and oxygen precursor bubbler to vaporize the liquid precursors and direct the gases to the reactor head. When the user requests to access the cabinet, the system will command the turning off program to close all pneumatic valves and MFCs to prevent exposing the users to any chemical gases.

The metal precursor is held in a stainless steel bubbler, while the oxygen precursor is held in a custom-made polycarbonate bubbler (shown in Figure 2.5). A SMC SS0750 pneumatic manifold with EX260 serial transmission system shown in Figure 2.6 is used to control the distribution of the compressed air to the corresponding pneumatic valves based on the PLC program. The PLC program automatically turns on and off specific pneumatic valves based on the programmed functions. The pneumatic valves operate with 80 PSI compressed air that is supplied from the compressed air line in the lab.

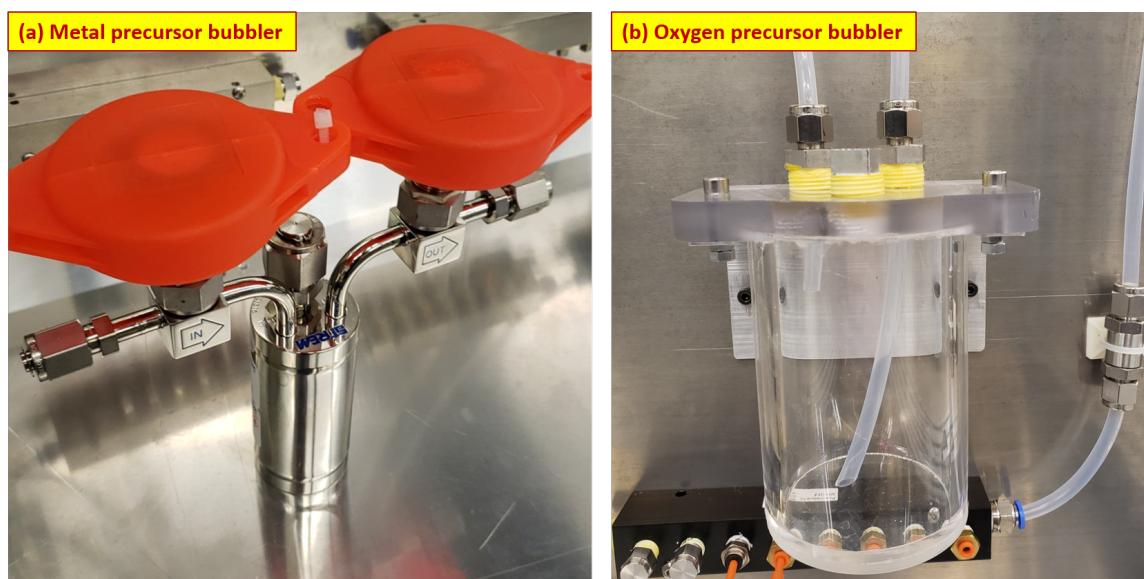


Figure 2.5 (a) Metal precursor bubbler made up of stainless steel (b) Water precursor bubbler made up of polycarbonate.



Figure 2.6 A picture of SMC SS0750 pneumatic manifold with EX260 serial transmission system.

Nitrogen gas is used to bubble the precursor solutions contained in the bubbler to create the precursor vapors. All the nitrogen used in AP-SALD was supplied from a single compressed nitrogen tank regulated to ~45 psi. The nitrogen gas supply is connected to a manifold, which will distribute the gas to five MFCs shown in Figure 2.7. All the flows in the system were controlled electronically by Brooks Thermal Mass Flow Controllers Model

SLA5850. The MFCs are daisy-chained together and communicates with the PLC using RS485 connection.

In Figure 2.7 (a), green lines represent the nitrogen gas lines, red lines represent the metal precursor gas lines, and blue lines represent the oxygen precursor gas lines. The AP-SALD was designed to accommodate two metal precursor gases and one oxygen precursor gas. For initial testing, the precursor gases used are diethyl zinc (DEZ) and distilled water (H₂O) to create zinc oxide (ZnO) films.

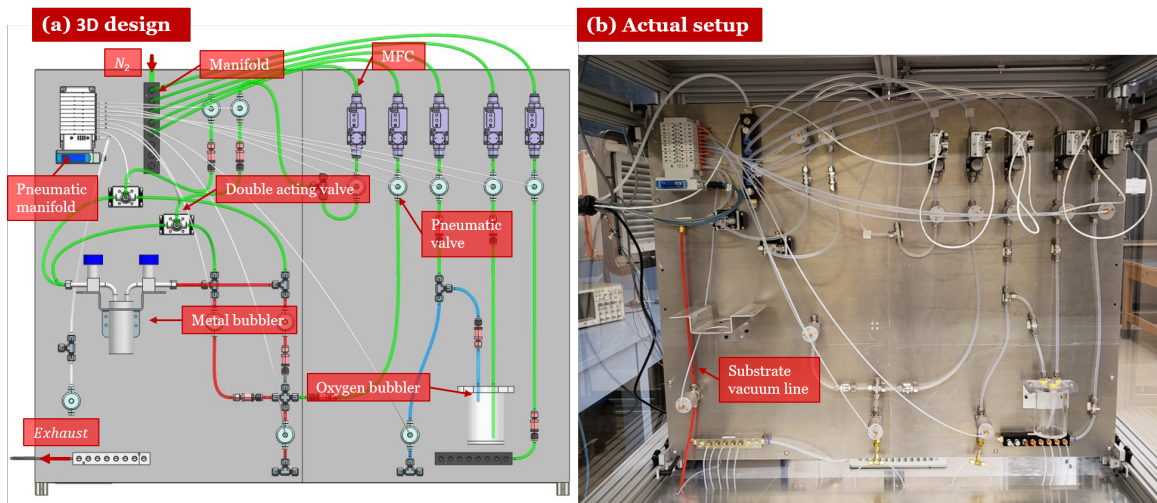


Figure 2.7 (a) 3D design of the bubbling panel in Siemens NX for planning, photo credited to Jhi Yong Loke (b) the actual setup of the bubbling panel.

In order to control the flow distribution in the bubbling panel shown in Figure 2.7 (b), several pneumatic valves, double-acting valves, and one-way valves are included in the AP-SALD system. The pneumatic valves are used to turn on or off the gases to the reactor head. The double-acting valves are used to either direct the nitrogen gas to the metal precursor bubbler for bubbling or bypass the bubbler for purging or idling. Switching the lines can be used to create doped metal oxides thin films by co-injecting and mixing different precursor gases in the lines before depositing onto the substrate or switch between different precursor gases between layers [43].

2.3 Reactor Head Sub-system

The reactor head consists of multiple gases and exhaust slits (machined from stainless steel plates) stacked horizontally. It was designed with modularity and scalability in mind. The initial reactor head design is made up of 13 stainless steel slits, which includes one metal precursor slit, one oxygen precursor slit, three nitrogen slits, two cooling slits, and six exhaust slits, as shown in Figure 2.8. However, 3D printed slits were used for rapid prototyping purposes before the slit's design is finalized. The 3D parts were printed with high temperature resin using a Form 2 SLA printer from Formlabs.

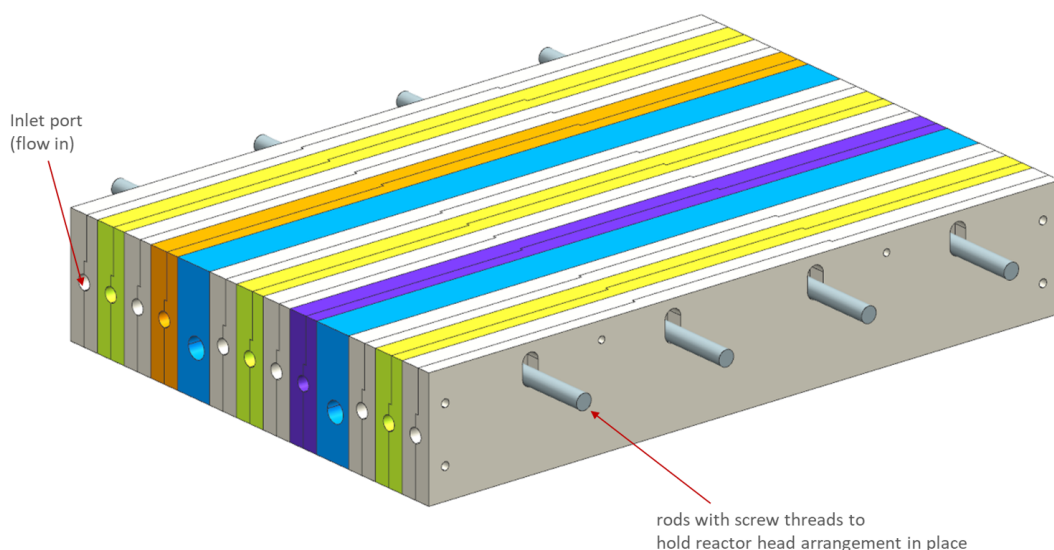


Figure 2.8 An isometric view of the modular reactor head, which can be equipped with heating channels, cooling channels, plasma enhancers, and other components. The inlet ports are on both ends of the slit, where the flow comes in from both sides. The rods are used to hold the slits together.

Figure 2.9 depicts the arrangement of the channels to effectively separate the precursor gases for atomic layer deposition (ALD). The channel arrangement can also be configured in a way that promotes chemical vapor deposition (CVD).

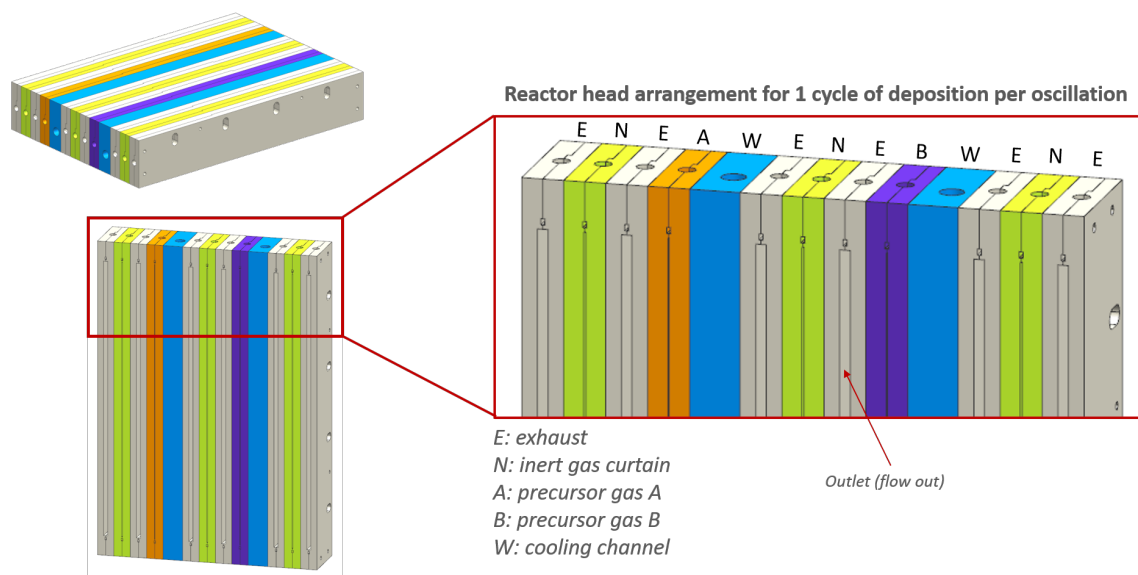


Figure 2.9 Detailed view of one possible arrangement for the modular reactor head

Computational fluid dynamics (CFD) analysis, engineering design and 3D printing/ mechanical machining were used to make a reactor head that can deposit thin films via AP-SALD. In order to achieve the goal, the precursor gases must be isolated to prevent mixing during the deposition. The first step involves preliminary design of the channels that represents the flow region, as shown in Figure 2.10. CFD simulations were conducted to study the parameters for ALD mode deposition, such as reactor head-substrate spacing, precursor gas 1 inlet pressure, precursor gas 2 inlet pressure, exhaust suction pressure, and nitrogen inlet pressure. The assumptions made to simplify the simulations were compressible gas, no heat transfer involved, and no movement for the linear stage under the reactor head. The CFD simulations were conducted in ANSYS Fluent software based on the parameters listed in Table 2.1.

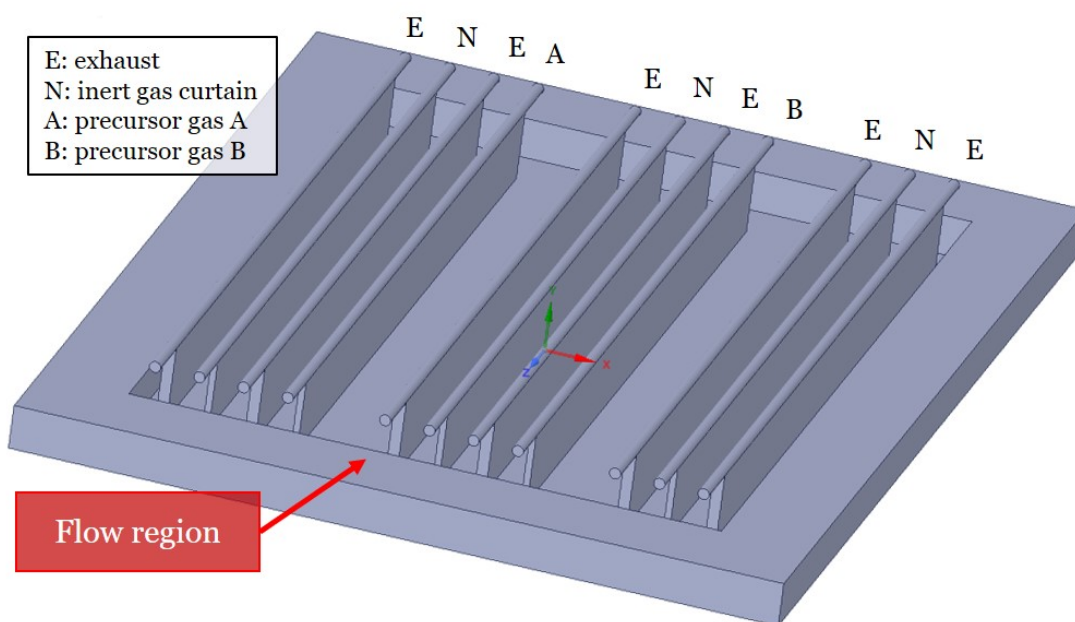


Figure 2.10 A 3D model of the flow region based on the reactor head design shown in Figure 2.9.

Table 2.1 The CFD's modeling parameters of the reactor head

Modeling variable	Setting
Precursor gas 1 inlet pressure	7,000 Pa
Precursor gas 2 inlet pressure	7,000 Pa
Nitrogen inlet pressure	10,000 Pa
Exhaust suction pressure	-50,000 Pa
Reactor head-substrate spacing	0.15 mm

From Figure 2.11, it can be observed that precursor A (black lines) and precursor B (red lines) were well isolated based on their velocity streamlines. With sufficient nitrogen flow as isolating curtains between the precursor gases, efficient exhaust pressure, and small reactor-substrate spacing, the undesirable mixing between the precursor gases can be minimized. By increasing the reactor head-substrate spacing to 3 mm, the CFD result shown in Figure A.1 in Section A.1 of Appendix A exhibits signs of potential mixing, indicating that the reactor-substrate spacing is critical for isolating the precursor gases.

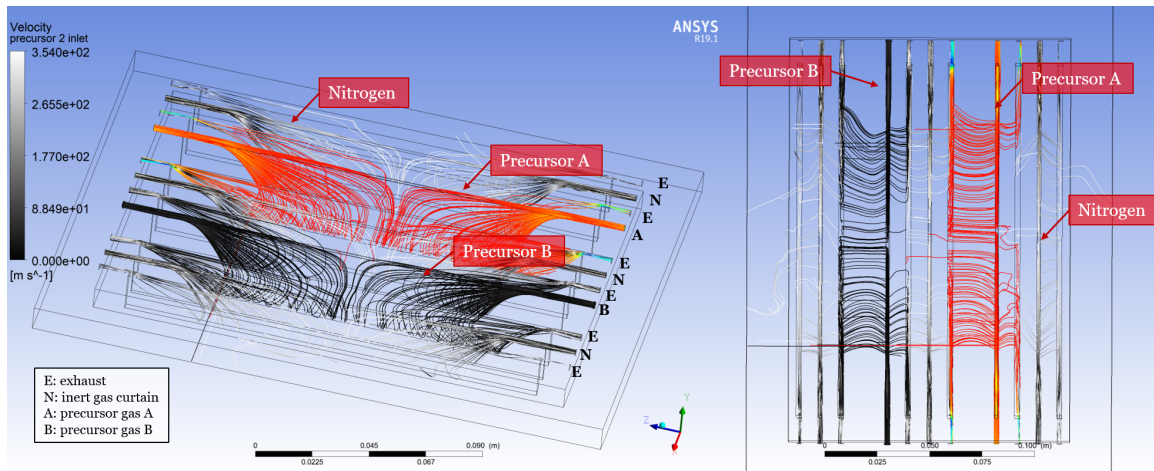


Figure 2.11 A 3D CFD simulation result based on parameters in Table 2.1. Black lines represents precursor A while red lines represents precursor B. White lines are nitrogen.

CFD simulations were also conducted in 2D to simplify the simulation for determining representative parameters. In the 2D model, the flow speed at the inlets were specified and the outlet pressure was set to atmospheric pressure. With 0.15 mm reactor-substrate spacing and $1 \frac{m}{s}$ flow speed at each inlet, the result in Figure 2.12 showed that the gases were well isolated, where precursor A (blue lines) did not mix with the precursor B (orange lines). As it can be gathered from the streamlines, the flow tends to move towards the least resistive path, where the pressure was low/negative. Since the slits are relatively far apart as compared to the lab-scale reactor head, the gases remain well-isolated even with a reactor head-substrate spacing of 0.45 mm based on the simulation result shown in Figure A.2 in Appendix A.

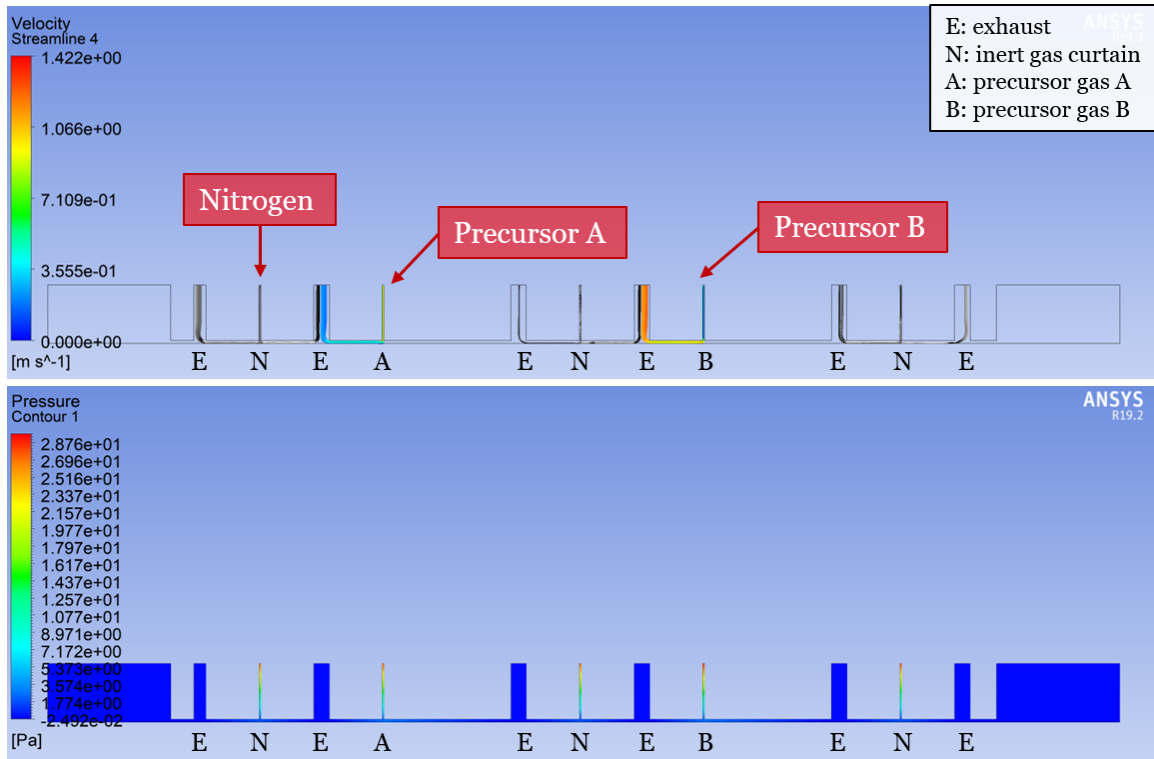


Figure 2.12 A 2D CFD simulation result based on the same 3D simulation parameters.

Apart from precursor gases isolation, the uniformity of the flow at the length of the outlet is critical for depositing uniform films. The key metric used to analyse the flow uniformity is the velocity profile along the outlet. In Figure 2.13, the highlighted region is where the substrate will be exposed to the gases.

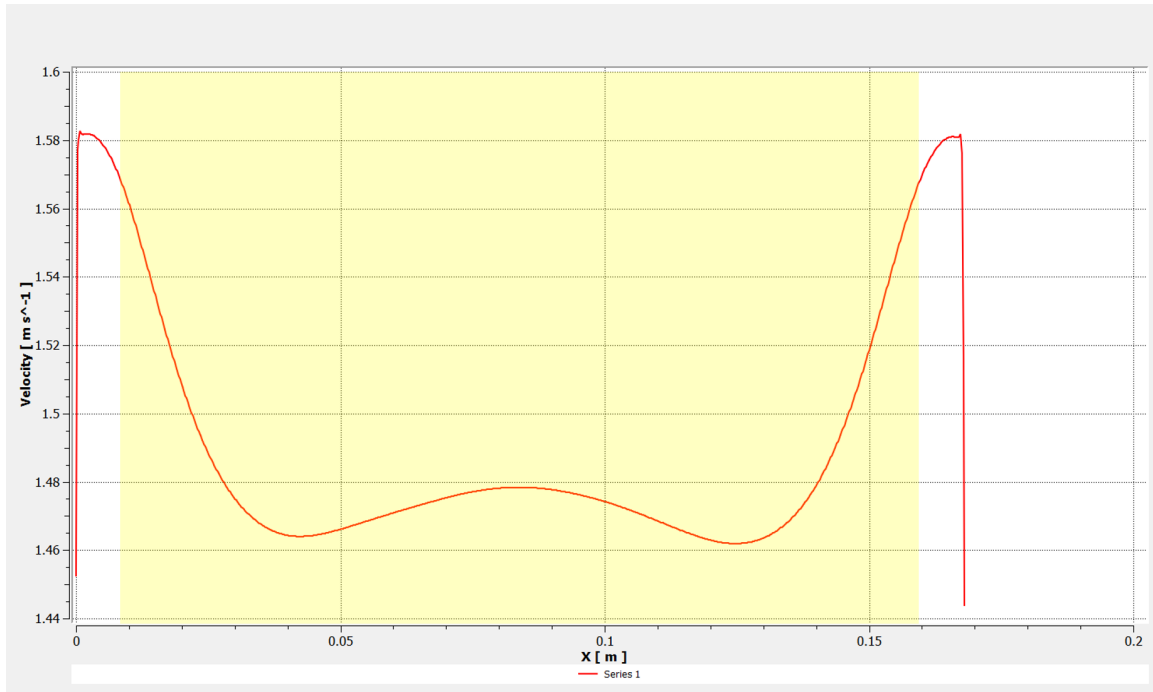


Figure 2.13 The CFD result of flow velocity across the slit shown in Figure 2.18

The simulation was conducted based on the maximum flow rate of the precursor gas (400 sccm) combined with precursor carrier gas (3000 sccm). The combined flow rate (3400 sccm) was divided into two inlets with 1700 sccm each. The flow velocity variation of $0.105 \frac{m}{s}$ between the highest ($1.57 \frac{m}{s}$) and lowest ($1.465 \frac{m}{s}$) velocities is acceptable. If the flow velocity variation is too high, some sites on the substrate might be more saturated by a precursor than others, resulting in non-uniform deposition. The CFD steps could be repeated until a satisfactory or desirable uniform profile (or slope) is attained. Once a finalized channel geometry is determined, the reactor head is re-designed by integrating the new channel geometry into it. Some of the slits were 3D printed using an SLA printer with a resolution of at least $25 \mu m$ and layer thickness of $50 \mu m$. More detail and discussion on this topic will be reported in Jhi Yong's MAsC thesis.

One oscillation in the AP-SALD system was defined as passing the substrate back and forth once underneath the reactor head, which is equivalent to two ALD cycles. The

reactor head can be equipped with more slits to enable multiple ALD cycles in a single substrate oscillation to facilitate high-throughput coating. Heating/cooling channels and plasma channels could also be integrated into the horizontal stack to control the precursor temperatures and to facilitate coating on materials that are more thermally sensitive and require low temperatures, such as fabrics and plastics.

The length of the slits can be increased to enable multiple substrates or larger substrates to be coated at the same time hence enabling high throughput. Each reactor head component can be customized, installed or swapped out, for different functions and purposes - for example, to enable deposition of films with thickness gradient and/or doped films for fast prototyping and testing of film properties.

The individual components are stacked horizontally for easy assembly. The height of individual reactor channel can be mechanically adjusted precisely relative to its adjacent components to achieve desired interspaced elevation (Figure 2.14 (a)).

The interspaced elevation adjustment is expected to provide more flexibility and control over the quality and uniformity of deposition. In Figure 2.14 (b) and Figure 2.14 (c), the exhaust channels are moved up slightly to create a region that promotes the precursor gases to flow into and should improve the exhaust efficiency to prevent the gases from mixing.

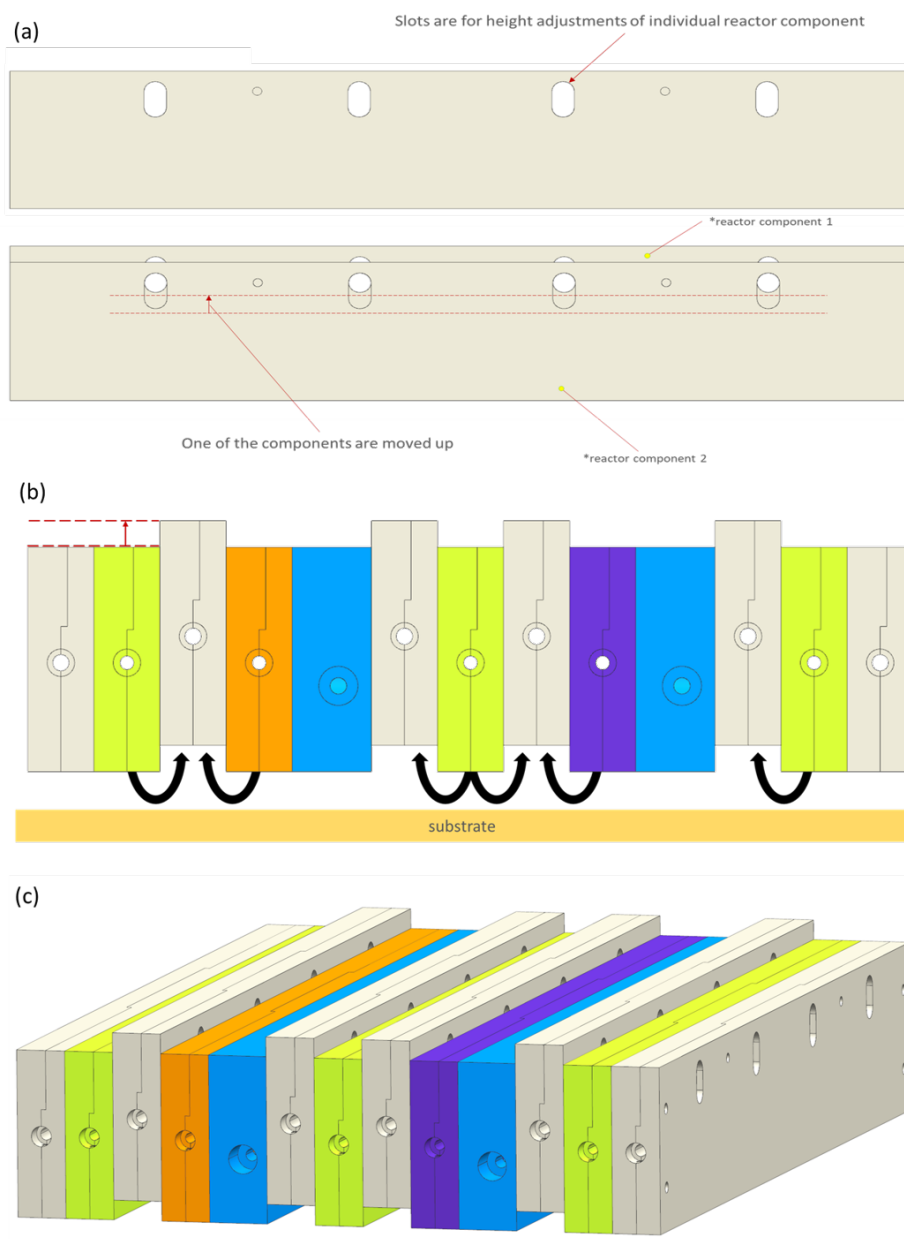


Figure 2.14 (a) A side view of a reactor head component and the interspaced elevation adjustment between two components. (b) A front view of the reactor head with adjustable interspaced elevations for different reactor components. (c) An isometric view of the reactor head.

The cooling channel shown in Figure 2.15 consists of a copper plate to effectively remove heat from the precursor gas channel by circulating chilled water inside the channel.

Controlling the temperature of the adjacent precursor channels ensures that heat-induced

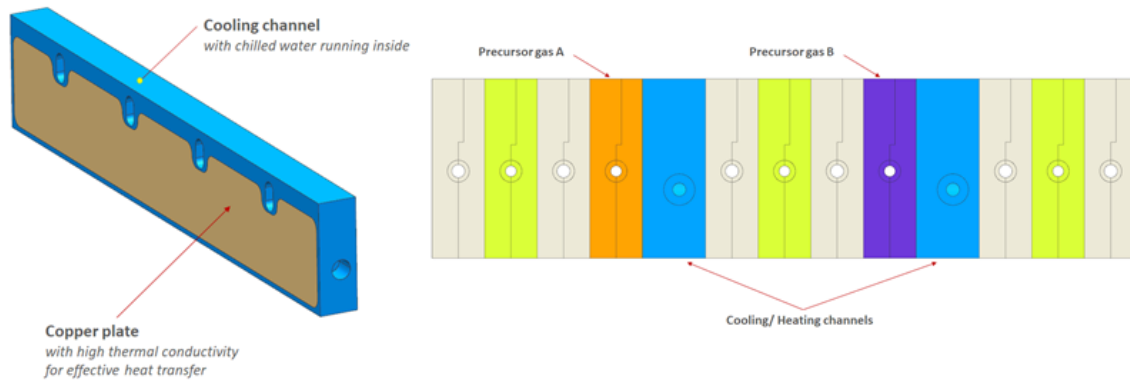


Figure 2.15 A side view of the cooling channel and the placement of the cooling channels beside the precursor gas components.

chemical reactions (and hence film deposition) occur on the substrate, rather than in the precursor channel or before impingement on the substrate. Conversely, the chilled water can be replaced with hot water or a heating element to heat up the precursor channel for precursor gases that are prone to unwanted condensation on cold surfaces. Figure 2.16 illustrates the potential integration of a plasma channel within the reactor head. Plasma can enhance commercial-scale AP-SALD's performance by lowering the required deposition temperature, improving film properties due to more complete reaction, and making the deposition of other potential materials possible.

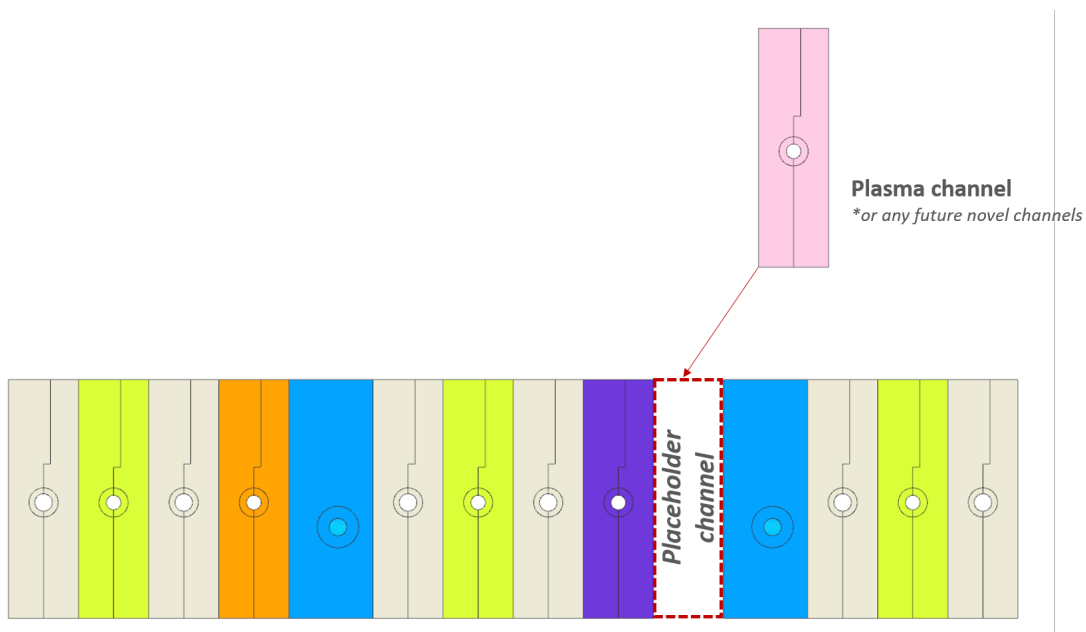


Figure 2.16 An example of a plasma channel integrated with the reactor head.

In Figure 2.17, the reactor head is attached to a mounting plate, which currently allows for mounting up to four sets of ALD slits capable of depositing on substrates that are 400 mm wide.

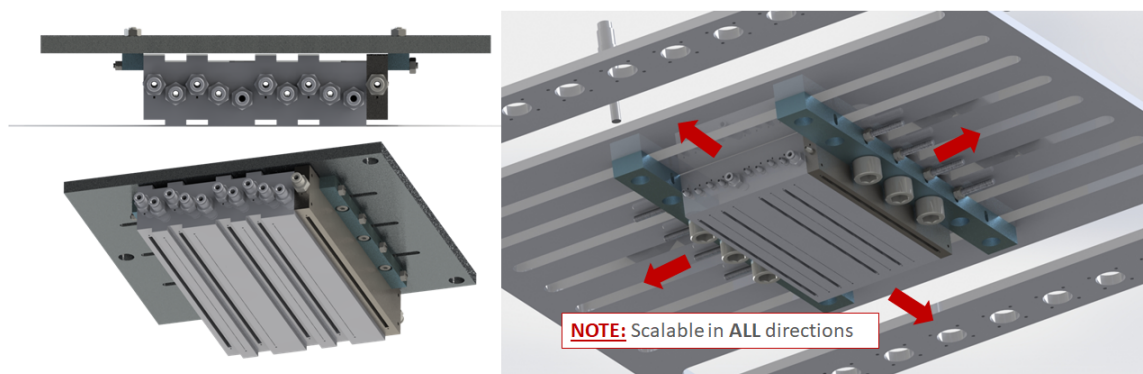


Figure 2.17 The front and bottom views of a scalable reactor head design.

These channels can be fabricated by using additive manufacturing or mechanical machining. The two symmetrical half-pieces concept simplifies the design for manufacturing using

mechanical machining and provides a low-cost solution to fabricate these customized slits. With this fabrication technique combined with the modular reactor head technology discussed above, each individual reactor head component can be customized, installed or swapped out, for different functions and purposes.

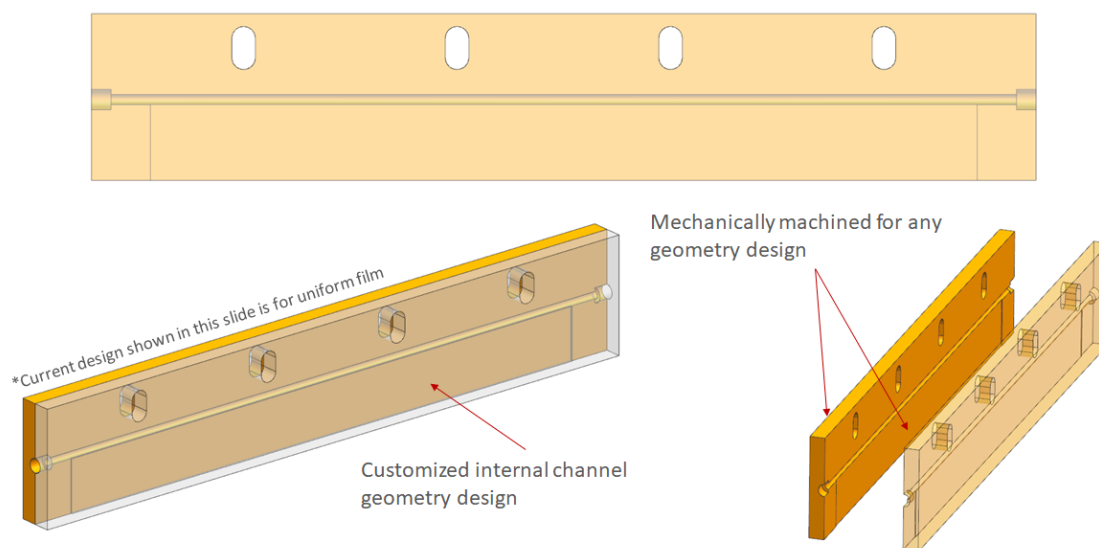


Figure 2.18 A perspective view of the reactor slit design that can be modified to produce uniform flow.

Figure 2.19 shows the actual setup of the reactor head attached to the mounting plate. 3D printed parts were used for prototyping purposes before more resources are spent on machining stainless steel slits which are costly. Once the ideal channel geometry is determined for uniform deposition through experiments, the next step will then be proceeding with machining the remaining stainless steel slits.



Figure 2.19 The actual setup of the reactor head with linear actuators and laser sensors.

The control of the reactor head positioning and substrate-reactor spacing is done by mechanical means (auto-leveling). The positioning system with a mounting component for the reactor head is designed to provide flexibility in configuring and maintaining the orientation and position of the reactor head relative to the substrate. Referring to Figure 2.20, the positioning system consists of three laser displacement sensors as displacement measuring devices and four linear actuators as displacement controlling devices. With both the laser sensors and linear actuators, an in-house auto-leveling code was developed to dynamically monitor and adjust the spacing between the reactor head and the substrate stage with a resolution of $1\ \mu\text{m}$. The auto-leveling code was used to determine the vertical distance, z that each linear actuator needs to travel based on the laser sensors' readings and desired reactor head-substrate spacing. Three points from the three laser sensors were used

to construct a plane equation using the following equation.

$$ax + by + cz = d$$

Where at least one of the real-number constants "a," "b," and "c" is not zero, and "x", "y" and "z" represent the axes of the three-dimensional plane.

The plane was determined using vector cross product. A vector is a line formed between two points in space, while a cross product is the multiplication of two vectors. Another plane equation was also determined based on the desired spacing and angles. If the reactor head requires to tilt at certain angle along the x-axis (ϕ), and angle along the y-axis (θ), rotation matrices are applied to the plane equation and a z value for each linear actuator is calculated. The plane equation was then extended to the locations of the linear actuators. The z differences for each linear actuator between the current plane (constructed by laser sensor's readings) and the desired plane (constructed by desired spacing and angles) are used to move linear actuators to achieve the desired reactor-head substrate spacing.

The ability to accurately control the reactor-substrate spacing can provide control over whether the precursor gases remain isolated (ALD occurs) or mix in the gas phase (CVD occurs).

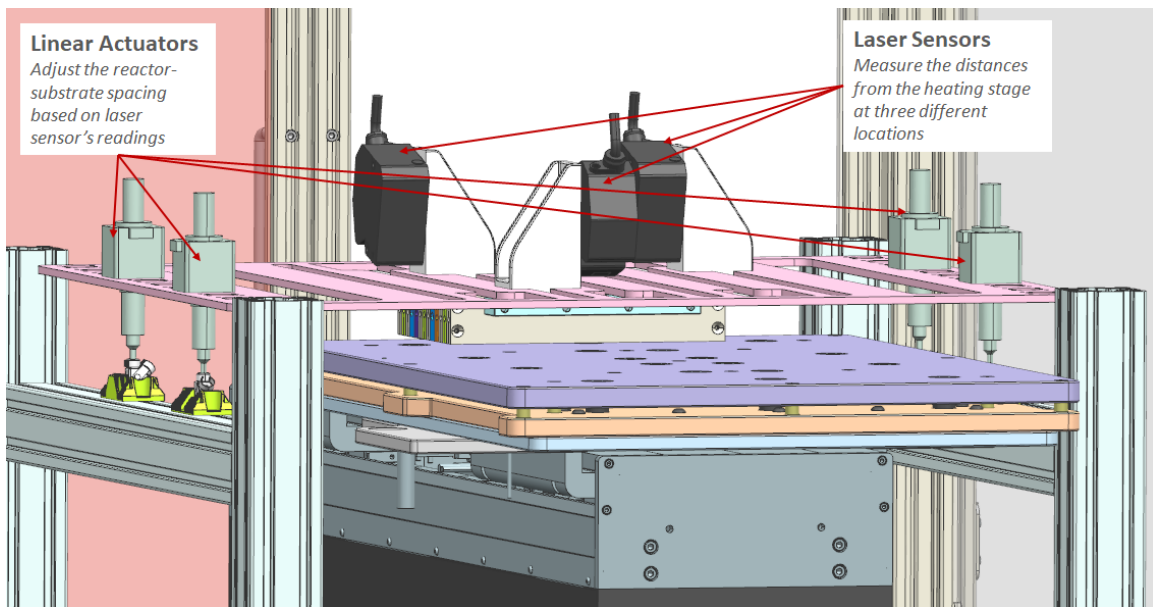


Figure 2.20 An illustration of a positioning system of the reactor head to the heating stage.

2.4 Heating Sub-system

A heating stage is required to heat substrates to a certain temperature for the precursor gases to react at the surface of substrate. The heating stage consists of aluminum plates that are sandwiching a heating element. Aluminum was chosen as the material for the heating stage because of its good thermal conductivity and light weight. A custom formed tubular heater with a diameter of 0.315" rated at 208V 2800W was used to heat up the stage. A thermocouple was integrated into the heating stage to provide feedback on the heating performance. Thermocouples were also installed inside the cabinet to monitor the temperature of the environment. A customized vacuum reservoir was built and installed below the heating stage to provide suction to the substrates. The detailed design of the heating stage and vacuum holding mechanism will be discussed in Jhi Yong Loke's MASc thesis. In this section, the heating stage design overview and a temperature controller interfaced with the Siemens PLC are discussed.

Figure 2.21 (a) illustrates the heating stage with suction. A substrate of any size, geometry, and thickness can be heated up on the heating stage and held by the vacuum as long as it is within the stage dimensions and is flat. Figure 2.21 (b) shows an example of the substrates held by the vacuum. This vacuum hole pattern was configured to accommodate substrates of different sizes and geometry.

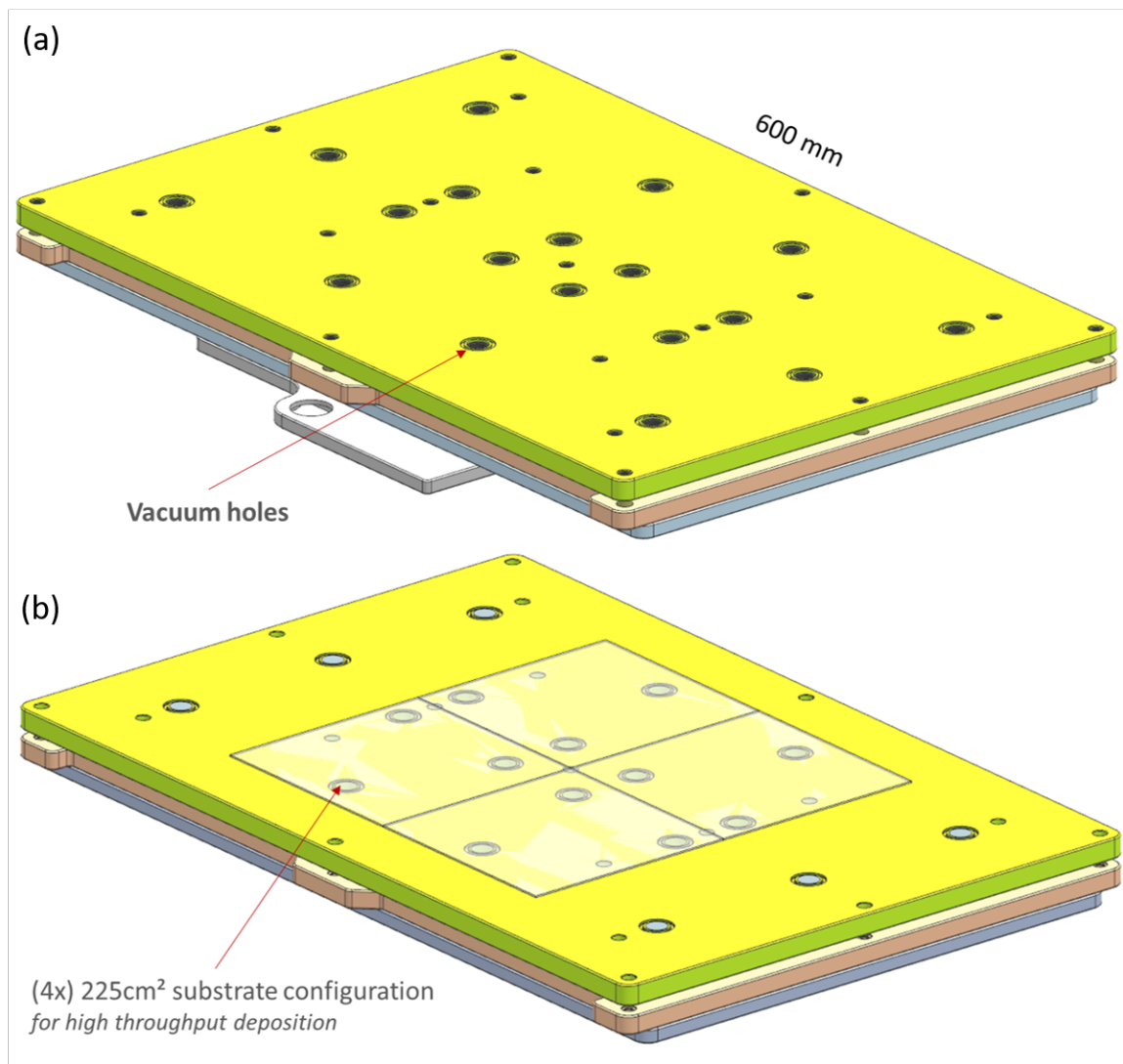


Figure 2.21 (a) A view of the heating stage with a vacuum holding mechanism. (b) An example of substrate placement configuration with four 225 cm² substrates.

The heating stage was offset from the vacuum reservoir (which provides the suction to hold the substrates down) by 10 mm to provide an air gap for insulation. An Aluminum-Silica insulation board was added to provide better insulation for the vacuum reservoir and linear stage from the heat generated by the heating stage. This insulation board is lightweight and uniformly dense. It offers low thermal conductivity, high temperature stability, uniform density and excellent resistance to thermal shock. A thermocouple is installed in the linear stage that is used to oscillate the heating stage to actively monitor the motor's temperature,

to ensure that the heating stage does not overheat the linear stage.

The tubular heater used to heat up the stage is shown in Figure 2.22. Figure 2.23 shows the actual setup of our heating stage, where the top plate was electroplated with 0.0005" Nickel to protect the aluminum plate from scratches and prevent oxidation.



Figure 2.22 A picture of the customized heating element.

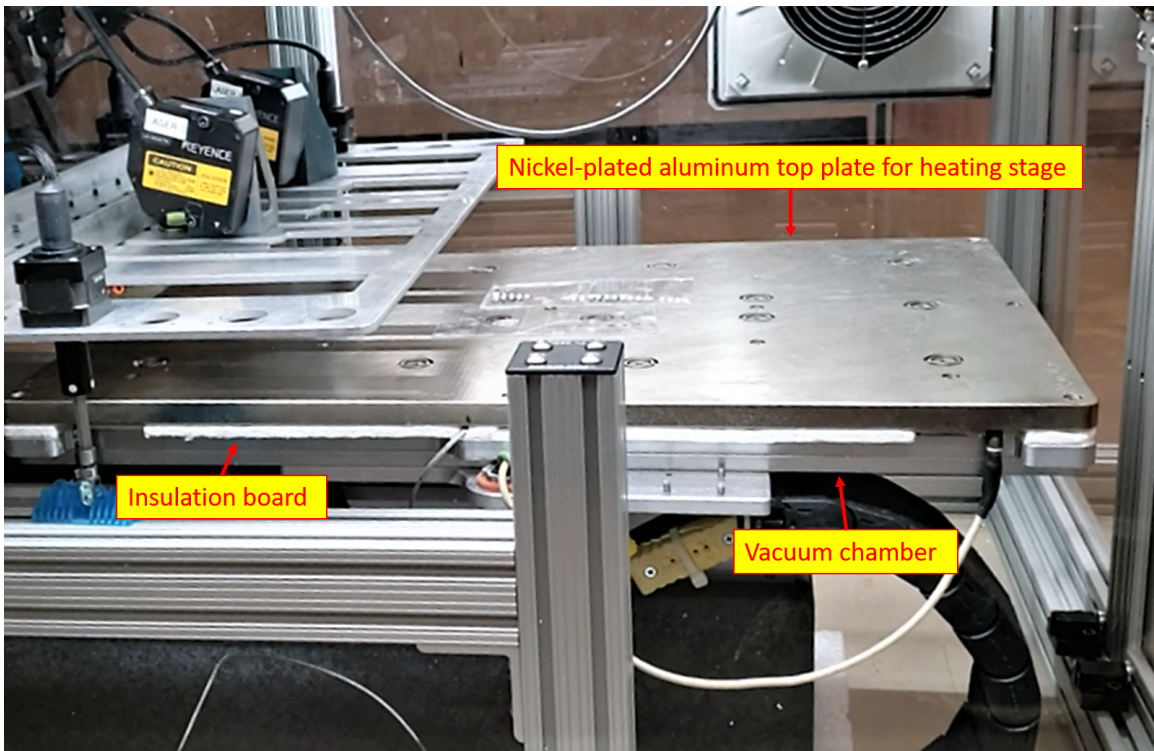


Figure 2.23 A picture of the actual heating stage setup.

In order to control the heating, a controller box specifically for the heater was built and connected to the PLC. The controller box consists of two 240V 15A fuses, two safety relays, and a solid state relay as shown in Figure 2.24. Both the relays and solid state relay are connected to the PLC. The safety relays are used to turn on and off the power supply to the heater. Two relays are used to provide redundancy in making sure the high voltage line is cut off if either of them fails. A solid state relay is used to control the amount of power supplied to the heater via a pulse width modulation (PWM) generated by the digital output PWM module from the Siemens PLC.

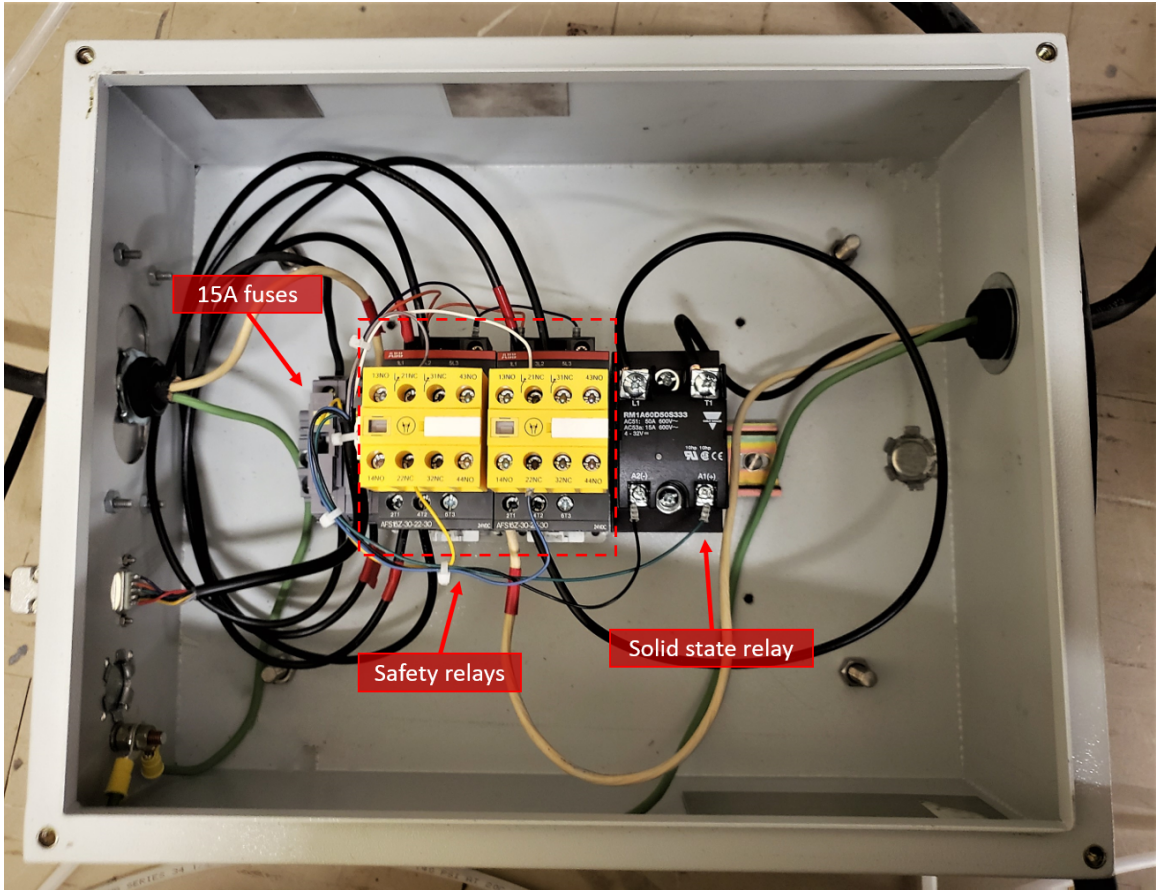


Figure 2.24 A picture of the heater's controller box

Siemens PLC has a built-in temperature process program, which works as a PID controller with anti-windup and weighting of the proportional and derivative actions. The PID algorithm operates according to Equation 2.1 (control zone and dead zone deactivated):

$$y = K_p \left[(b \cdot w - x) + \frac{1}{T_I \cdot s} (w - x) + \frac{T_D \cdot s}{a \cdot T_D \cdot s + 1} (c \cdot w - x) \right] \quad (2.1)$$

Table 2.2 outlines the meaning of the variables used in Equation 2.1 and the associated parameters used in the Siemens PLC PID block diagrams shown in Figure A.3 and Figure A.4 in Appendix A. Figure A.3 presents an overview of the temperature process controller program that processes temperature reading and set points, and calculates the

PWM percentage as the output to control the power supply for heating. Figure A.4 shows the PID program with anti-windup algorithm (PIDT1 Anti Windup block shown in Figure A.3) to maintain the temperature of the substrates.

Table 2.2 The definition of variables used in Equation 2.1 and associated parameters used in block diagram shown in Figure A.3 and Figure A.4 in Appendix A.

Variable	Definition	Associated parameters
y	Output value of the PID algorithm	-
K_p	Proportional Gain	Retain.CtrlParams.Heat.Gain Retain.CtrlParams.Cool.Gain CoolFactor
s	Laplace operator	-
b	Proportional action weighting	Retain.CtrlParams.Heat.PWeighting Retain.CtrlParams.Cool.PWeighting
w	Setpoint	CurrentSetpoint
x	Process value	ScaledInput
T_I	Integral action time	Retain.CtrlParams.Heat.Ti Retain.CtrlParams.Cool.Ti
T_D	Derivative action time	Retain.CtrlParams.Heat.Td Retain.CtrlParams.Cool.Td
a	Derivative delay coefficient (derivative delay $T_I = a \times T_D$)	Retain.CtrlParams.Heat.TdFiltRatio Retain.CtrlParams.Cool.TdFiltRatio
c	Derivative action weighting	Retain.CtrlParams.Heat.DWeighting Retain.CtrlParams.Cool.DWeighting
DeadZone	Dead zone width	Retain.CtrlParams.Heat.DeadZone Retain.CtrlParams.Cool.DeadZone
ControlZone	Control zone width	Retain.CtrlParams.Heat.ControlZone Retain.CtrlParams.Cool.ControlZone

The built-in program allows easy configuration of the proportional–integral–derivative (PID) controller parameters as shown in Figure 2.25. The duty cycle of the PWM signal is bounded between 0 and 100%.

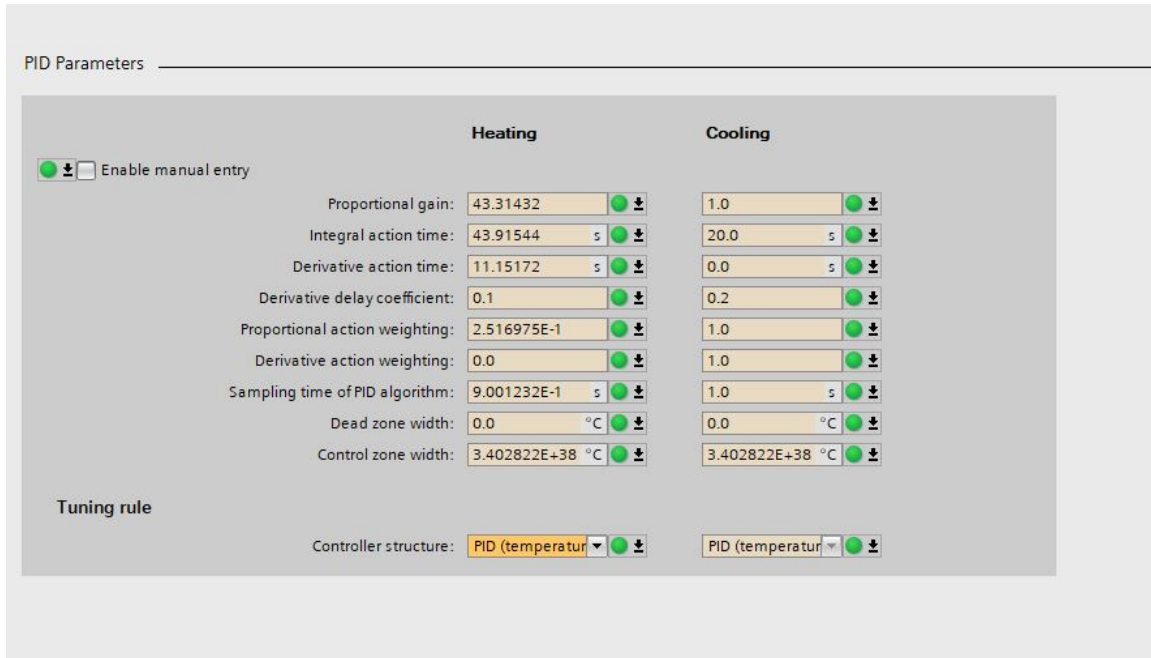


Figure 2.25 A screenshot of PID parameters configured by Siemens PLC through its pretuning and fine-tuning programs. Only the heating has been configured.

2.5 Linear Stage Sub-system

The linear stage consists of an Akribis stage and a Mitutoyo granite slab to provide high moving stage speeds for high deposition rates to ultimately achieve high throughputs. The Akribis stage uses a linear motor to directly drive the payload, such as the heating stage and vacuum reservoir. The linear motor generates the high acceleration while maintaining smooth motion. A 3rd order motion profile is used to limit the jerk in the system. A Mitutoyo granite slab, with flatness variations within $2.54\ \mu\text{m}$ and a mass of 110 kg, is installed and the linear stage is mounted on top. This is done to ensure that the linear stage is held stable and that it operates with known vertical accuracy and flatness. The granite slab also functions to absorb the vibrations caused by the high speed movement of the linear stage. Figure 2.26 shows the setup of the linear stage with granite slab, heating stage and vacuum reservoir.

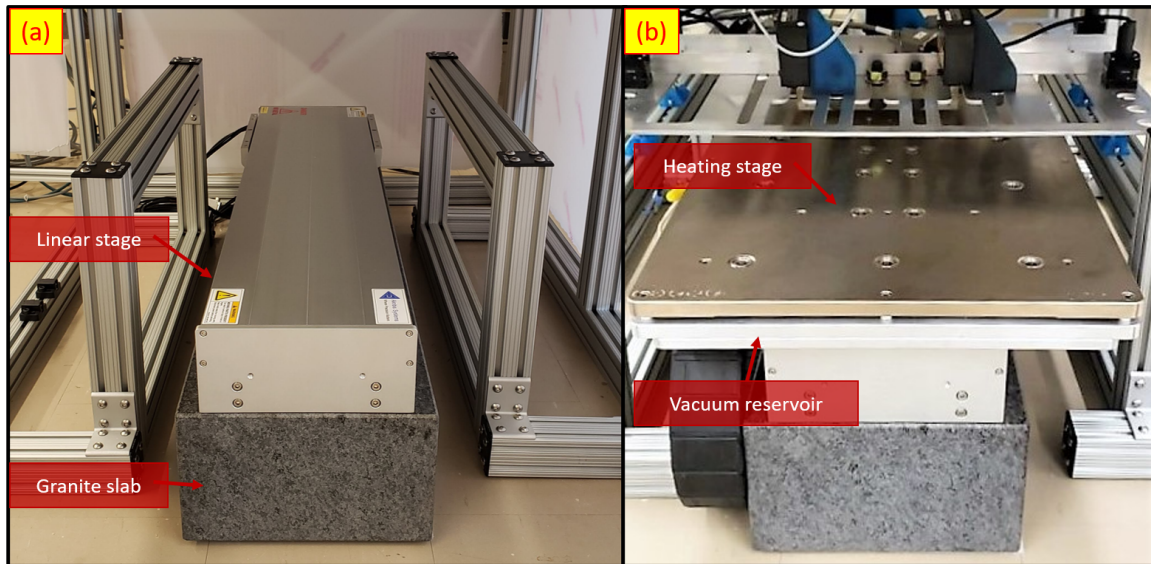


Figure 2.26 (a) The setup of Akribis linear stage with granite slab only. (b) The setup of the linear stage with heating stage and vacuum reservoir.

The Akribis stage provides a 600 mm stroke length with zero backlash and maximum acceleration of $39.92 \frac{m}{s^2}$ and a maximum speed of $2 \frac{m}{s}$. The stage can achieve vertical

flatness of less than $\pm 8 \mu\text{m}$ for a stroke length of 300 mm. The vertical flatness needed to be minimized because it would affect the reactor head-substrate spacing, which is a critical factor for SALD deposition.

A Galil DMC motion controller and a Kollmorgen AKD servo drive are used to control and drive the Akribis stage. Referring to Figure 2.27, the linear motor is wired to the Kollmorgen AKD servo drive, and the encoder from the linear stage is wired to the Galil DMC controller.

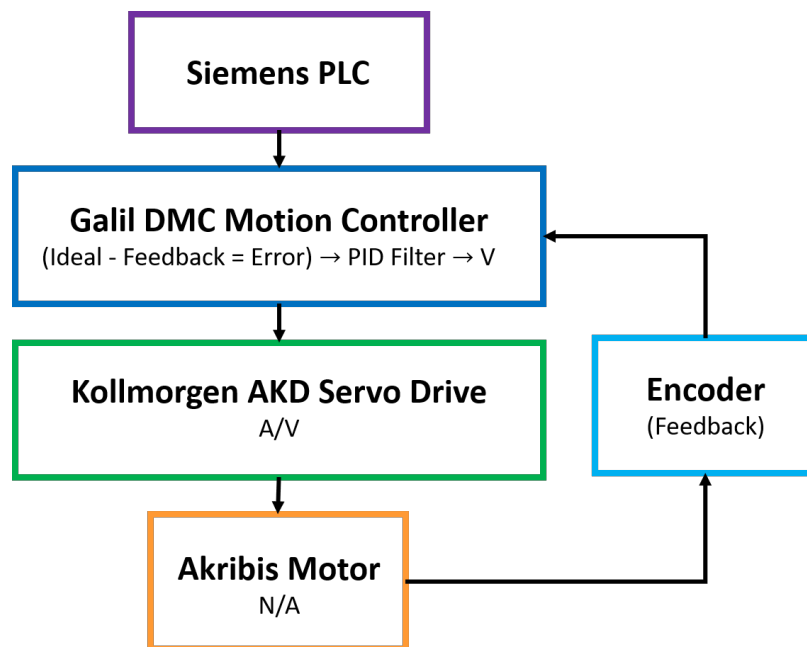


Figure 2.27 An overview of the connections among Siemens PLC, Galil DMC motion controller, Kollmorgen AKD servo drive, and Akribis stage.

The Kollmorgen AKD servo drives can generate significant electrical noises due to the PWM switching to control the motor current, and extra care was taken to ground them properly. The motor and the encoder shields are grounded. Furthermore, the drive was grounded in the panel using a star configuration, meaning that there is one central ground point for the entire panel to avoid ground loops. Figure 2.28 shows the actual setup of Galil DMC controller and Kollmorgen AKD servo drive in the electrical panel with the Siemens

PLC.

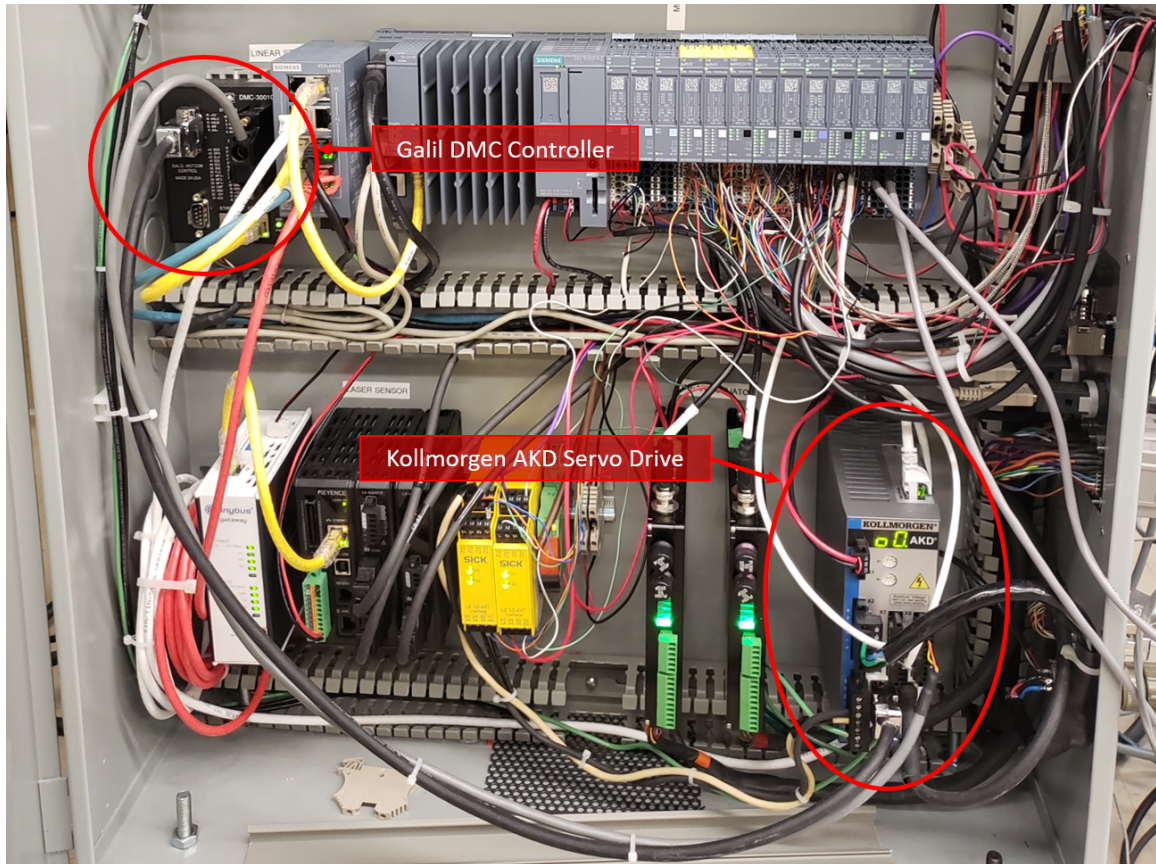


Figure 2.28 A picture of the actual setup of Galil DMC controller and Kollmorgen AKD servo drive in the electrical panel.

The Galil DMC takes in the encoder reading, and outputs an analog signal to the drive (torque output). The Kollmorgen AKD servo drive takes in the analog torque signal and then sends current to the linear motor through the motor power cable. The Kollmorgen's drive settings are configured to match the motor parameters, such as maximum current, inductance, and so on, while the rest of the control is handled by the Galil DMC, such as PID, motion control, and Modbus communication.

The Galil controller communicates with the Siemens PLC using Modbus TCP via an ethernet cable, so the programs in Galil can be commanded from the PLC. Most of the motion functions such as oscillating the stage, setting the speed, homing, auto-calibrating, stopping the stage, and turning the motor on and off, were programmed in the Galil DMC controller.

The Akribis linear stage's performance depends heavily on the payload mounted to it. The total weight of payload, including the heating stage and vacuum reservoir, was approximately 20 kg, which limits the permitted velocity and acceleration of the stage. It is important to make sure that the output continuous current of the Kollmorgen AKD servo drive does not exceed $4.6 A_{rms}$, which could trip the motor and overheat, consequently damaging the servo drive. Figure 2.29 shows the result of an initial test without the payload and the output continuous current was $1.785 A_{rms}$, which was well below the maximum continuous current of $4.6 A_{rms}$ the motor can handle.

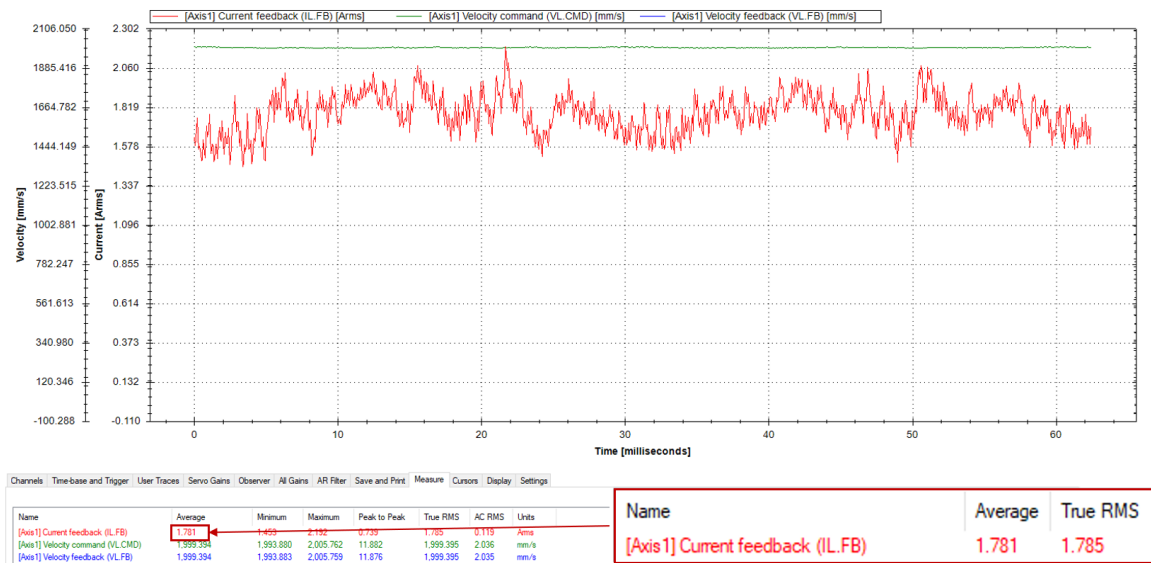


Figure 2.29 A screenshot of Kollmorgen AKD's operating scope which shows the output continuous current is $1.785 A_{rms}$.

As an additional safety measure to prevent the motor from overheating, a thermocouple is attached on the motor case (see Figure 2.30) near the coil unit where the motor coils generate heat. The linear stage also came with a thermostat, which is an open-close switch with a triggering temperature of $100\text{ }^{\circ}\text{C}$. If the temperature of the motor coil surpasses $100\text{ }^{\circ}\text{C}$, the thermostat will close and send a signal to the PLC to turn off the motor. With the thermocouple installed outside, we can correlate it to the internal temperature by monitoring the thermostat as it surpasses $100\text{ }^{\circ}\text{C}$. The thermocouple also allows us to monitor the motor's temperature when we heat the stage up to high temperatures.

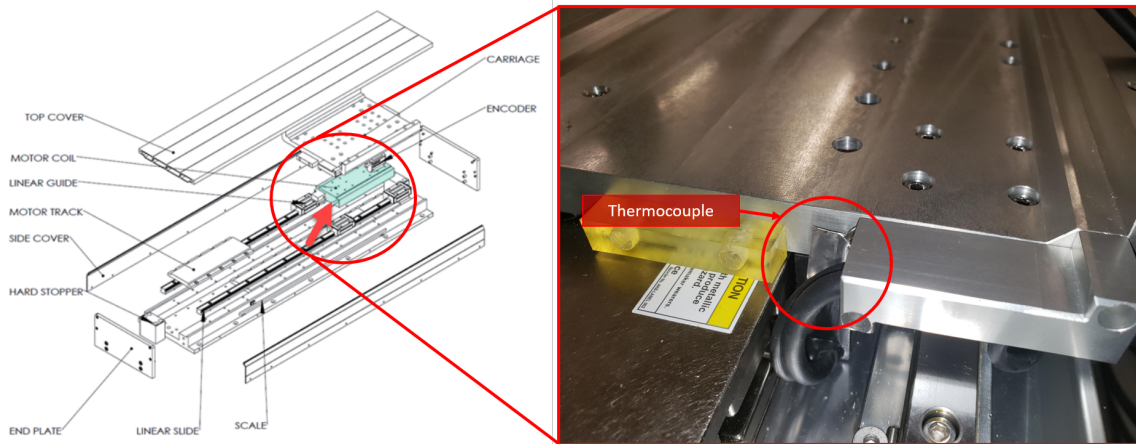


Figure 2.30 A picture of the thermocouple's location at the coil unit of Akribis stage.

Uniform velocity, v_u is required for the regions where the substrates fully pass underneath the reactor head. This feature ensures the deposition rate on the substrate is uniform without any flow interruptions caused by acceleration or deceleration. The total travel distance required for uniform velocity, s_1 is the sum of the length of the reactor head and the length of substrate.

Uniform velocity region distance = Reactor head's length + Substrate's length

$$\text{Uniform velocity region distance} : 0.134 \text{ m} + 0.300 \text{ m} = 0.434 \text{ m}$$

Figure 2.31 shows a schematic of the uniform velocity region and maximum acceleration and deceleration distances.

The maximum acceleration distance, s_2 is equal to the maximum deceleration distance, which is calculated by the following equation.

$$\text{Maximum acceleration distance} = \frac{\text{Full stroke length} - \text{Uniform velocity region}}{2}$$

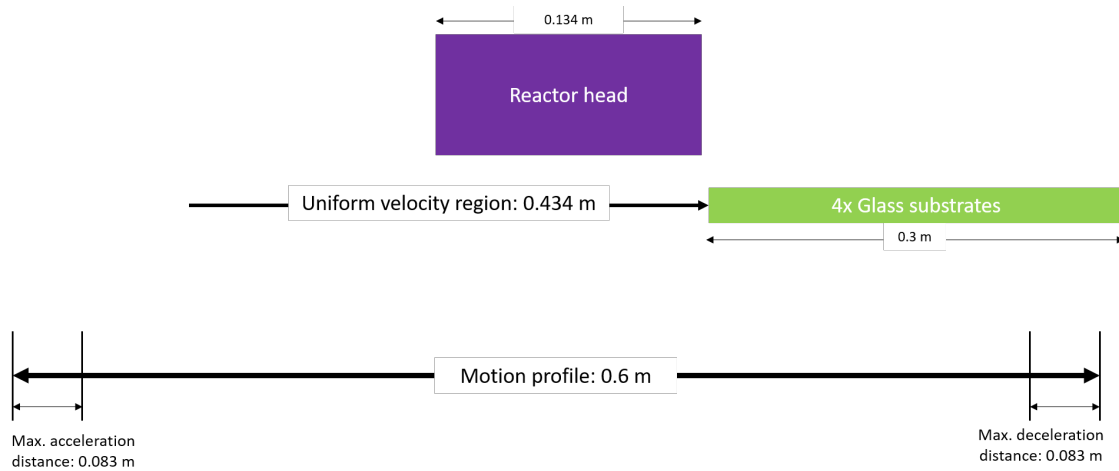


Figure 2.31 A schematic of the uniform velocity region.

$$\text{Maximum acceleration distance} : \frac{0.600 \text{ m} - 0.434 \text{ m}}{2} = 0.083 \text{ m}$$

The ideal velocity profile is shown in Figure 2.32, where Table 2.3 provides the definition of each variables. The area under the graph represents the distance traveled by the stage. The highlighted red regions represent the acceleration and deceleration zones, while the highlighted yellow region represents the uniform velocity region.

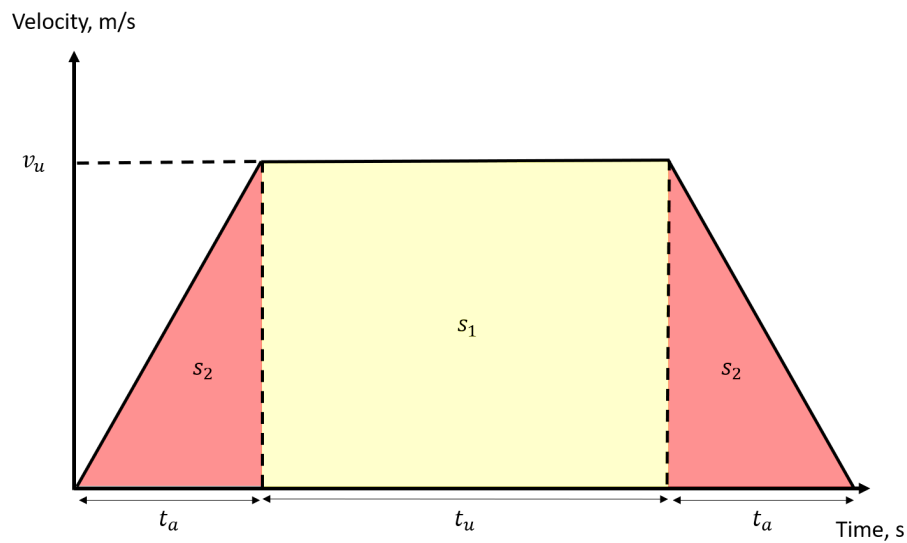


Figure 2.32 A schematic of the ideal motion profile.

Table 2.3 The definition of variables for the velocity profile.

Variable	Definition
v_u	Uniform velocity
t_a	Time for acceleration
t_u	Time for uniform velocity
s_1	Distance for uniform velocity
s_2	Distance for acceleration and deceleration

Based on kinematic equations, Equation 2.2 and Equation 2.3 were derived to determine time required for uniform velocity and acceleration to simulate the motion profile of the linear stage using Tecnotion's motor simulation tool [44]. The uniform velocity was calculated based on Equation 2.6. The relationship between the acceleration and uniform velocity was calculated based on Equation 2.7. The sum of the time for acceleration, uniform velocity, and deceleration was based on the desired oscillation frequency (f) for the linear stage, as shown in Equation 2.4 and Equation 2.5. However, the maximum oscillation frequency depends on the continuous force that could be supplied by the linear stage, which is 221N according to its datasheet. Based on Newton's first law of motion, the maximum acceleration of the linear stage was the continuous force, F divided by the payload of the linear stage, m as shown in Equation 2.8. The resulting maximum acceleration is $11.05 \frac{m}{s^2}$. Referring to Table 2.4, the maximum oscillation frequency that the linear stage could achieve is 0.88 Hz with an uniform velocity distance of 0.434 m.

$$\text{Time for uniform velocity, } t_v = \frac{s_1}{v_u} \quad (2.2)$$

$$\text{Time for acceleration, } t_a = \frac{2 \cdot s_2}{v_u} \quad (2.3)$$

$$\text{Total time, } t_{total} = 2t_a + t_u \quad (2.4)$$

$$\text{Total time, } t_{total} = \frac{1}{2} \times \frac{1}{f} \quad (2.5)$$

$$\text{Uniform velocity, } v_u = \frac{s_1 + 4 \cdot s_2}{t_{total}} \quad (2.6)$$

$$\text{Acceleration, } a = \frac{v^2}{2 \cdot s_2} \quad (2.7)$$

$$\text{Maximum acceleration, } a_{max} = \frac{F}{m} \quad (2.8)$$

Table 2.4 The required time for uniform velocity and acceleration.

Oscillation frequency (Hz)	Stroke period (s)	t_v (s)	t_a (s)	v_u (m/s)	a (m/s ²)
0.10	5.000	2.833	1.084	0.153	0.141
0.15	3.333	1.889	0.722	0.230	0.318
0.20	2.500	1.416	0.542	0.306	0.566
0.25	2.000	1.133	0.433	0.383	0.884
0.30	1.667	0.944	0.361	0.460	1.272
0.35	1.429	0.809	0.310	0.536	1.732
0.40	1.250	0.708	0.271	0.613	2.262
0.45	1.111	0.630	0.241	0.689	2.863
0.50	1.000	0.567	0.217	0.766	3.535
0.55	0.909	0.515	0.197	0.843	4.277
0.60	0.833	0.472	0.181	0.919	5.090
0.65	0.769	0.436	0.167	0.996	5.974
0.70	0.714	0.405	0.155	1.072	6.928
0.75	0.667	0.378	0.144	1.149	7.953
0.80	0.625	0.354	0.135	1.226	9.049
0.85	0.588	0.333	0.127	1.302	10.215
0.88	0.568	0.322	0.123	1.348	10.949
0.90	0.556	0.315	0.120	1.379	11.452

In Tecnotion, a TB15N motor was selected to simulate the Akribis motor's motion profile. The parameters used in the simulation were noted in Figure A.5 in Appendix A. The simulated speed and acceleration shown in Figure 2.33 were $1.348 \frac{m}{s}$ and $11.044 \frac{m}{s^2}$ respectively, which were close to the calculated results in Table 2.4.

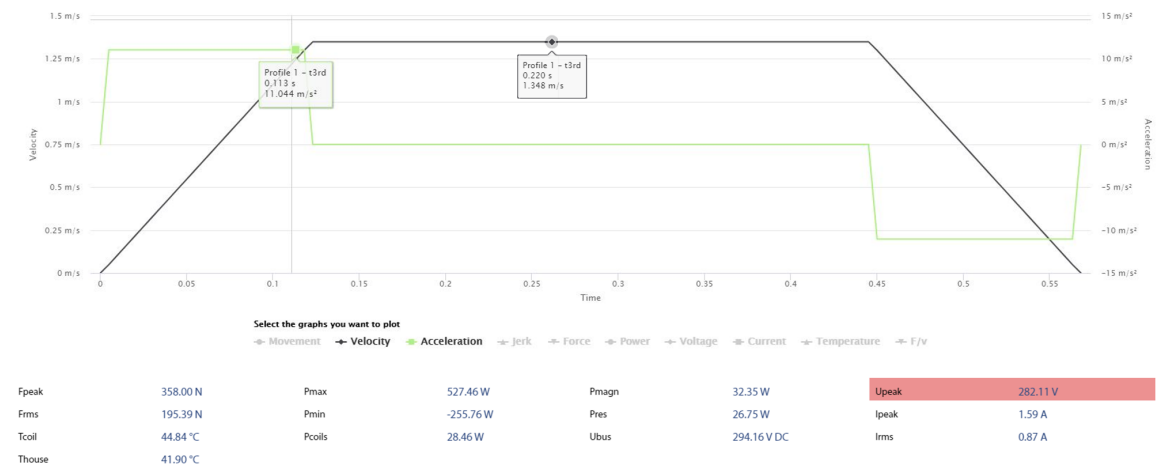


Figure 2.33 The simulation result in Tecnotion with an uniform velocity of $1.348 \frac{m}{s}$ and an acceleration of $11.044 \frac{m}{s^2}$.

Based on Equation 2.7 and a uniform velocity distance of 0.434 m, the following equation was derived and used in the Galil program for setting the speed and acceleration. The Galil program calculates the corresponding acceleration based on the speed input set by the user.

$$\text{Acceleration, } a = 6.024v^2$$

2.6 Control Sub-system

An industrial controller with input/output (I/O) modules to communicate with the various system components was used to develop the control system of the AP-SALD. A PC-based CPU with fail-safe version from Siemens was selected to provide a combination of PC-based software controller with visualization, PC applications, central I/Os, and integrated safety functions. All software for the AP-SALD system was written in TIA Portal V15.1, which is a Siemens PLC's software. The system is fully automated and optimized using PLC and built to meet industrial standards.

The part names of each product used in the control system along with the corresponding short description and usage are summarized in Table A.1 in Appendix A. The Human Machine Interface was designed and developed in WinCC RT Advanced of TIA Portal V15.1 software. Section A.5 in Appendix A shows screenshots of the HMI from the PLC, including log-on page, home page, flow control page, recipe overview page, device's control interface, device's status interface, and device's permissive/interlock interface. The functions of each interfaces are tabulated in Table A.2 in Section A.5 of Appendix A. Figure 2.34 shows most of the electrical components used in the AP-SALD system, including CPU, I/O modules, controllers, fuses, and safety relays.

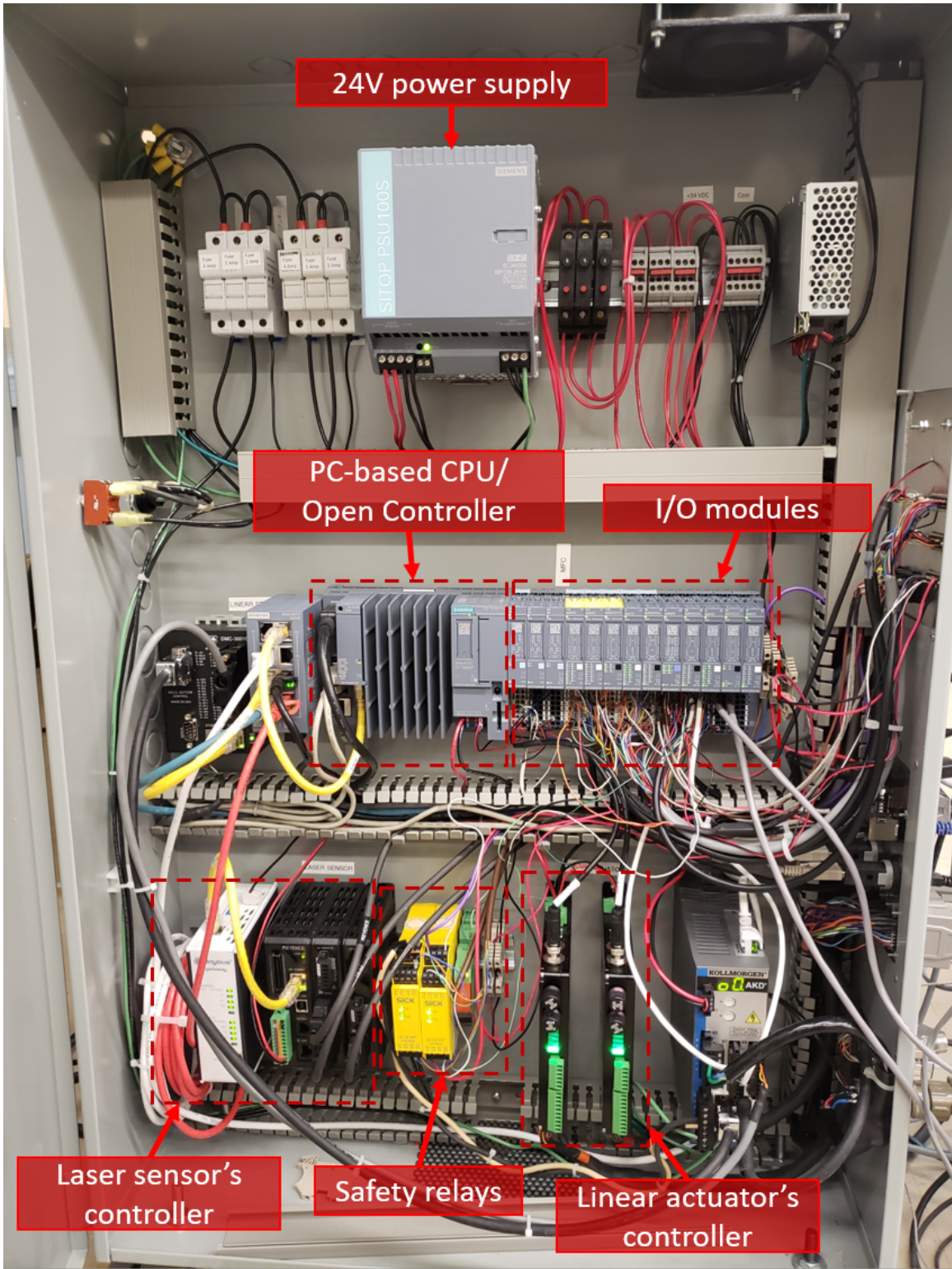


Figure 2.34 The controllers, I/O modules, power supplies, and contactors used in the control system of AP-SALD.

A state machine programming technique was used to make the PLC program simple and easy to create, maintain, and modify. By definition, a state machine model is a programming paradigm wherein the "machine", such as the controller, can only be in one of a set of distinct states and conditions at any given time. In the PLC, state machine programming can be cleverly done through the use of SET and RESET instructions and using internal contacts to direct flow of different states. The key concept is that only one state can be active at any one time, and all the other inactive states are disconnected from the power rail which controls the flow.

Interlocks and permissives are added to each state to make the programs robust. The interlocks are conditions that need to be satisfied for event actions to continue. The master state machine will continue running provided that the serial devices are communicating with the PLC. For instance, if the exhaust fans fail, the system will stop all the flows. On the other hand, the permissives are conditions that need to be satisfied before you can start an event action. For example, the auto-leveling can only start when the laser sensors are in range. Another example is that the linear stage can only move when the vacuum holding the substrates is turned on.

In the PLC program, multiple instances of the state machine can be running at the same time. For the AP-SALD system, one instance of the state machine is the master machine that handles all the actions and state transitions of the different states. Another instance of the state machine is the serial devices machine where it runs continuously in the background to communicate with the devices that use serial communication, such as the linear actuators (RS232) and the mass flow controllers (RS485).

The serial devices are daisy-chained together, meaning they share power and communication data, to simplify the wiring and reduce the number of I/O modules required to communicate with the PLC. A consequence of daisy-chaining the serial devices is that only one device

can be commanded at any given time. Hence, a serial device state machine was designed to command the serial devices sequentially for executing related actions stated in the master state machine.

This state machine was designed to continuously obtain the flow readings from the mass flow controllers and the position of the linear actuators to ensure the flow rates and the positions reach the desired setpoints. Thus, it will send a command to read from the mass flow controllers and the linear actuators one after the other continuously. If any other actions are commanded by the main state machine, the serial devices state machine will put the requested command in queue, wait until the serial bus is free, execute the selected action and then jump back to reading mass flow controllers' flows and linear actuators' positions.

Chapter 3

Testing Results and Discussion

Before starting to run experiments with actual chemicals, multiple dry runs were carried out with a series of tests to examine and verify the system's performance and program's reliability and repeatability. Failure modes and effects analysis (FMEA) was conducted to review as many components, assemblies, and subsystems as possible to identify potential failure modes in the AP-SALD system and their causes and effects on system operations. Below are elaborated results from our testing plan.

3.1 Linear Stage Movement Test

The goal of the test was to validate the performance and programs of the linear stage. All the programs in the Galil controllers were tested by commanding from the PLC. The programs include auto-calibrating (obtain zero reference position), homing (move to zero reference position), setting speed, jogging to the right, and jogging to the left. The linear stage was also tested to validate its maximum velocity and acceleration and ensure its operating current does not exceed the linear stage's limit. Figure 3.1 shows the output velocity and current. The maximum velocity is $1.35 \frac{m}{s}$ with a travel distance of 0.434 m. The motion profile matches well with the calculated values indicating that there are minimal variances between the physical and calculated values in Section 2.5 of Chapter 2. The root mean square (RMS) of the current is determined based on Figure 3.1 and Equation 3.1.

$$A_{rms} = \sqrt{\frac{t_1 A_1^2 + t_2 A_2^2 + t_3 A_3^2}{t_1 + t_2 + t_3}} \quad (3.1)$$

Where t_1 is the time for acceleration, A_1 is the current output during the acceleration, t_2 is the time for uniform velocity, A_2 is the current output during the uniform velocity, t_3 is the time for deceleration, and A_3 is the current output during the deceleration.

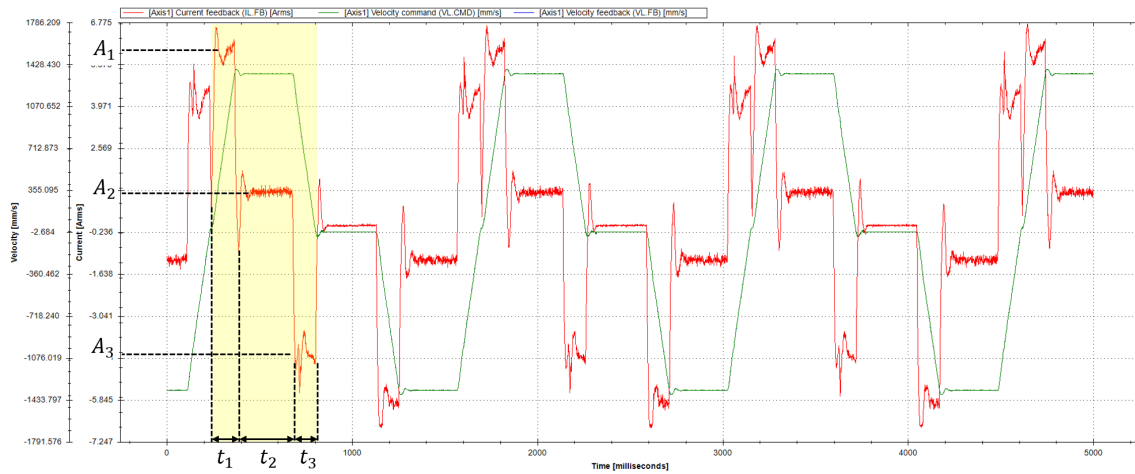


Figure 3.1 The test result output from Kollmorgen AKD that showed the velocity and current versus the time when the linear stage oscillated at $1.35 \frac{m}{s}$.

The highlighted region in Figure 3.1 shows one pass of the linear stage with labels of the time and the current for acceleration, uniform velocity, and deceleration. Only one region needs to be considered since the same motion profile was repeating over time.

Table 3.1 shows the time weighted squares of current values calculated based on each current and time. The calculated current is $3.51 A_{rms}$, which is within the $4.6 A_{rms}$ limit of the linear stage.

Table 3.1 The calculation of root means square of the current of the linear stage during the oscillation.

Current, A (A)	Time, t (ms)	Time weighted squares of current, tA^2 (msA^2)
5.85	109.00	3729.22
1.14	274.00	356.36
4.31	99.00	1840.58
SUM	482.00	5926.15
RMS (A)	3.51	

The linear stage was commanded to oscillate 200 cycles to make sure it does not fault when it oscillated at its maximum speed. No fault was observed during the test. Furthermore, the commanded position was compared with its actual position to check for any discrepancy. The linear stage has a built-in encoder that can measure its current position. It was observed

that there was no discrepancy in the expected and actual position of the stage along its travel distance.

The linear stage is also tied to safety. If the door is opened during a deposition, the safety will be broken and will stop the linear stage. This test was also carried out, for which the linear stage stopped as expected when the door was opened. The linear stage testing was a success because the maximum speed of the linear stage was determined and its performance is reliable and consistent with our calculations.

3.2 Substrate Suction Test

The goal of the test was to ensure the vacuum suction is strong enough to hold the substrates during oscillations. The heating stage is designed to hold four 150 (L) x 150 (W) mm² substrates. For initial testing, 50 mm (L) x 50 mm (W) substrates were used to cover all suction holes. The vacuum was turned on and then we tried using our hands to slide the substrates back and forth to test the strength of the suction. After this test, the stage was set to oscillate at maximum speed ($1350 \frac{mm}{s}$) with the 50 (L) x 50 (W) mm² substrates covering all suction holes. It was observed that the substrates could hardly be moved and they stayed intact during and after the oscillation. The tests were repeated with large 150 (L) x 150 (W) mm² substrates. It was observed that two vacuum holes were required at least to hold a large substrate with strong suction. When the vacuum holes are not in use, they can be blocked by insert plugs. The plugs designed to block the vacuum holes were also tested and confirmed that the sealing they provided works well. The test was a success as the substrates were held firmly during oscillations at maximum speed.

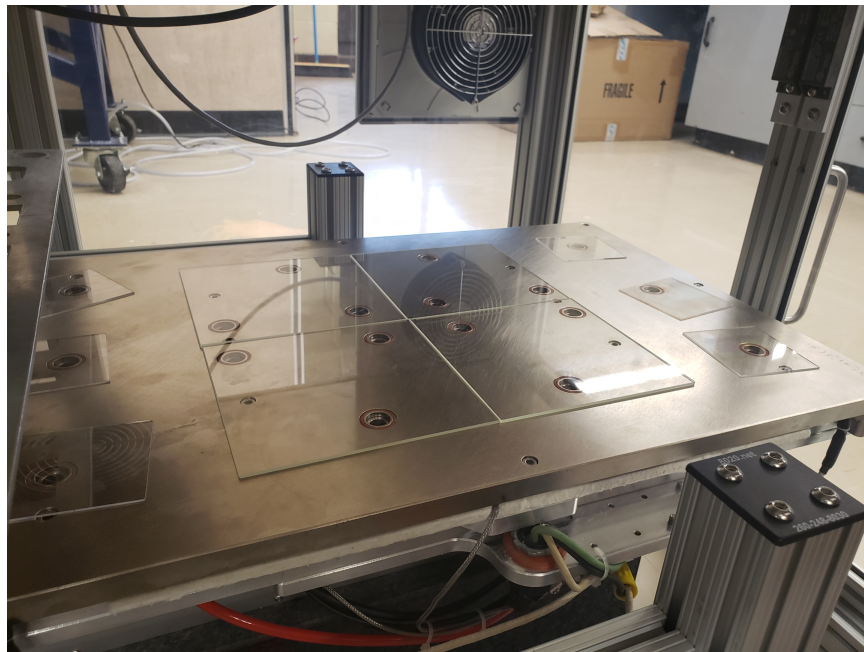


Figure 3.2 The placement of big substrates and small substrates during one of the substrate suction tests.

3.3 Substrate Heating Test and Linear Stage Temperature Monitoring

The goal of the test was to determine the ramp rate of the heater, identify any temperature offset between the heater and the top surface of the heating stage, and ensure the heating stage can maintain its temperature during oscillation. The setup of the heating elements was double checked for proper grounding to prevent shorting as well as electrocution. Thermocouples were used to measure the temperature of the surface of the stage. The leftmost and rightmost sides of the stage where the large substrates are meant to be placed were also measured to check the temperature profile's uniformity. At the same time, the temperature of the linear stage's motor was monitored to make sure that no significant heat is transferred from the heating stage down to the linear stage. The maximum allowable motor temperature is 125°C. For the test, the stage was heated up to 175°C from 25°C (ambient temperature) as shown in Figure 3.3.

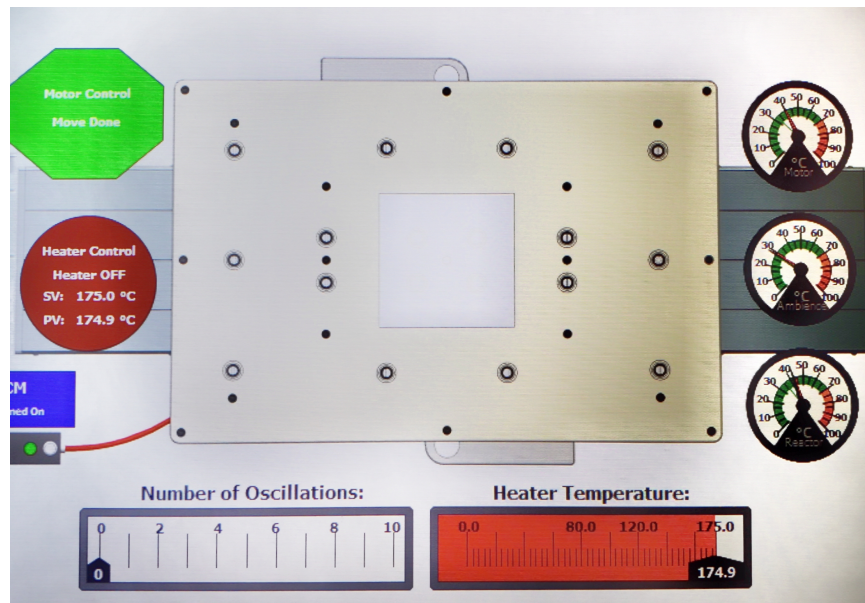


Figure 3.3 A picture of the heating test.

Figure 3.4 shows the temperature setpoint, the temperature input (feedback from a thermocouple), and the controller output of the heating stage. It took 12 minutes for the heater to reach 175°C indicating a ramp rate of 12.5 $\frac{^{\circ}\text{C}}{\text{min}}$. The temperature measured on the stage was 155°C, resulting a temperature difference of 20°C between the top surface’s temperature and the heater.

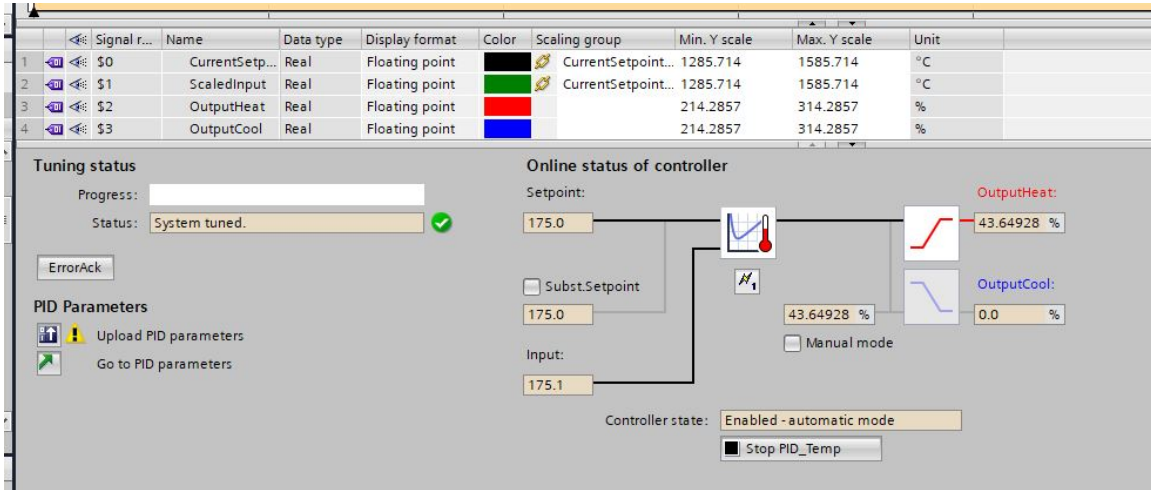


Figure 3.4 A screenshot of the response from the temperature controller from the heating stage.

The lower cabinet seemed to remain fairly cool even when the stage was heated up to 175°C. Based on the thermocouple’s readings in Figure 3.3, the motor’s temperature was 40°C; the ambient temperature was 30°C; the reactor head’s temperature was 42°C. It is clear that the exhaust fan worked to provide air exchange and to cool the cabinet.

However, the air flow from the cabinet exhaust fan seemed to cause a temperature drop on the side of the heating stage that was exposed to the fan, which disrupted the stage’s temperature uniformity. The temperature of the area of the linear stage exposed to the cabinet exhaust fan was measured at 147°C, while the other end of linear stage that was not exposed to the cabinet exhaust fan was at 155°C. The temperature measurement was done when the stage was not moving and a thermocouple was placed on the ends of the linear stage. An air guide on the exhaust fan may be required to redirect air to prevent unwanted

cooling of the heating stage.

3.4 Reactor Head Flatness Check, Substrate Stage Leveling, Auto-leveling

The goals of these tests were to ensure all the reactor head's slits align at the bottom, check if the substrate stage was leveled and flat, and validate the performance of auto-leveling with the laser sensors and linear actuators.

Figure 3.5 shows the assembly of the reactor head slits on the substrate stage to allow clamping and holding each slit flat with G-clamps. A 0.1 mm shim was used to check the alignment of each slit with its adjacent slits. Each slit was adjusted until all of them were aligned. It was found that over-tightening the rods at the top would cause the bottom of the slits to bow outwards in the direction of the fastening rods. Loctite was added to the nuts to prevent the assembly from loosening over time.

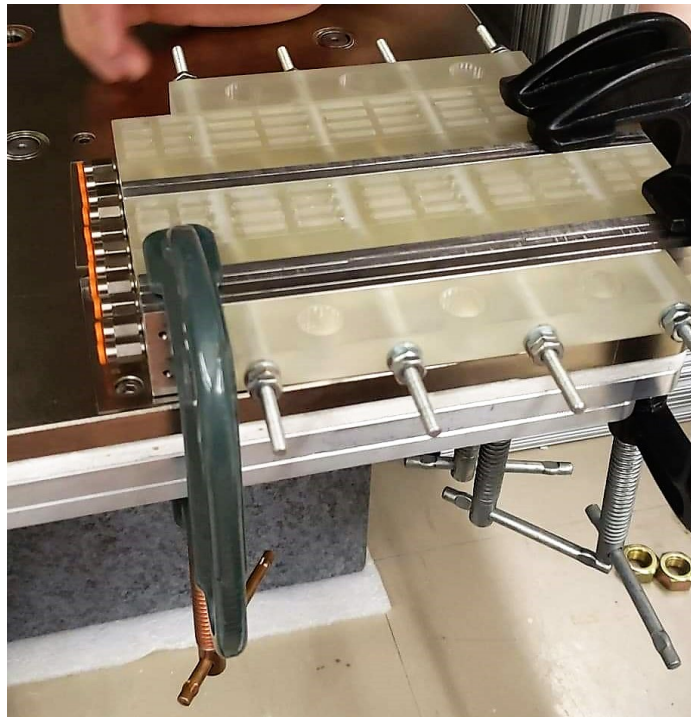


Figure 3.5 A picture of assembling the reactor head on the substrate stage, where the channels were facing down on the flat surface to ensure the bottom of the reactor was perfectly flat.

The flatness of the substrate stage was plotted based on the readings of the three laser sensors. Figure 3.6 shows the locations of the three laser sensors. The reactor head was first leveled until the laser sensors had the same values and then zero-ed in the center of the stage, so that the height variances are relative to the center of the stage where substrates are to be placed.

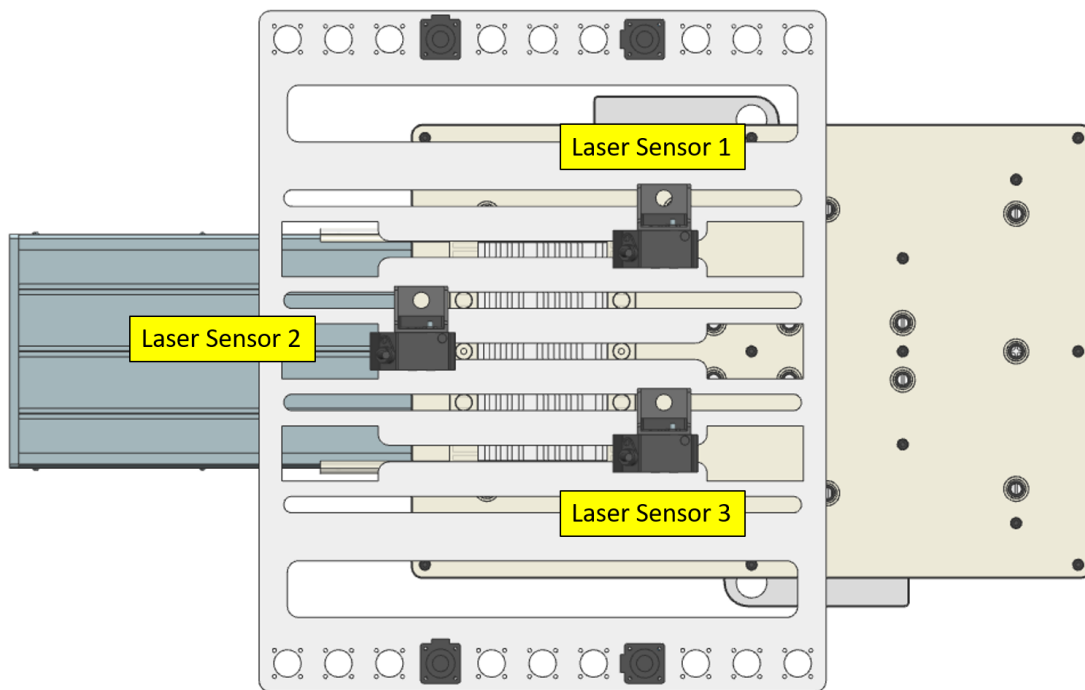


Figure 3.6 The locations of three laser sensors.

The test was conducted by moving the stage from one end to the other while simultaneously taking measurement using the three laser sensors. The data is shown in Figure 3.7. It was observed that part of the stage near laser sensor 3 was lower than the other parts of the stage near laser sensor 1 and laser sensor 2. This issue can be improved by using a spacer (see Figure 3.8 for the location of the spacers) that is slightly higher based on the height variation.

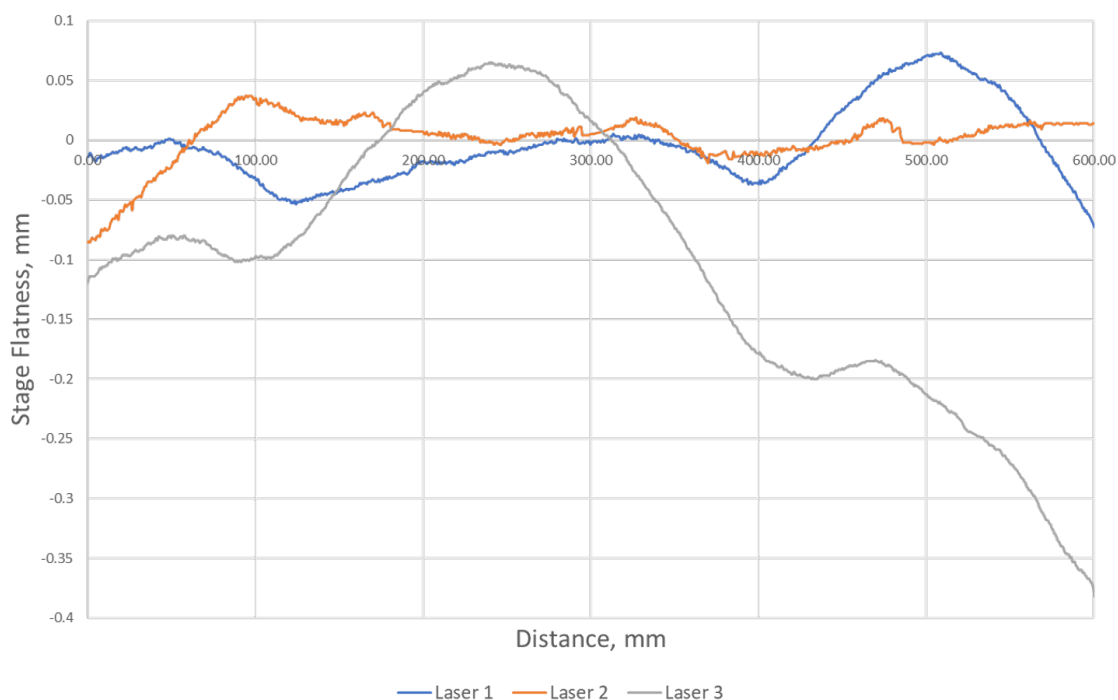


Figure 3.7 A plot of the stage's flatness profile based on three laser sensors' readings across the 600 mm long stage.

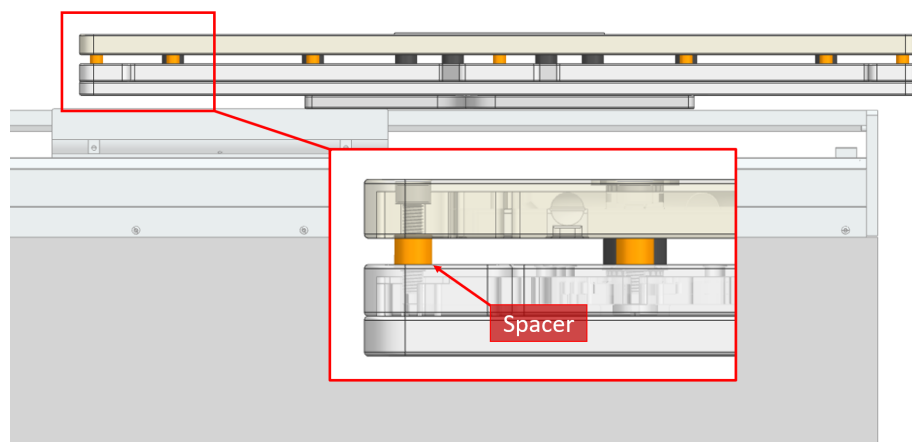


Figure 3.8 A picture shows the placement of spacers used to offset the heating stage from the vacuum reservoir.

Lastly, the reactor head-substrate spacing was validated using shims with known thickness. The linear actuators were moved all the way up, and large 150 (L) x 150 (W) mm² substrates were placed underneath the reactor head. The linear actuators moved down and stopped

when the laser sensors were in range. The laser sensor's readings before auto-leveling are shown in the lower left portion of Figure 3.9 (a). The reactor head-substrate spacing was then auto-leveled to the desired set point, as shown in Figure 3.9 (b) (0.125 mm in the figure). Figure 3.10 shows a shim was used to validate the spacing. The spacing was first set to a 0.5 mm gap and checked with a 0.5 mm shim. The linear stage was then set to oscillate 100 times at a moderate speed. The 0.5 mm gap was checked again with the shim after the oscillations were completed. These steps were repeated with smaller gaps, namely 0.4 mm, 0.3 mm, 0.2 mm, and 0.1 mm. There was no issue observed, which indicated the auto-leveling mechanism worked quite well.

However, heating will cause the stage to expand and affect the spacing. Another test was conducted with the same steps as above, but the stage was heated up to 150°C. It was observed that the spacing became smaller than the initial spacing value. In order to ensure the reactor head will not clash with the substrates, a re-calibration of the zero reference of the laser sensors is required once the stage has reached thermal equilibrium.

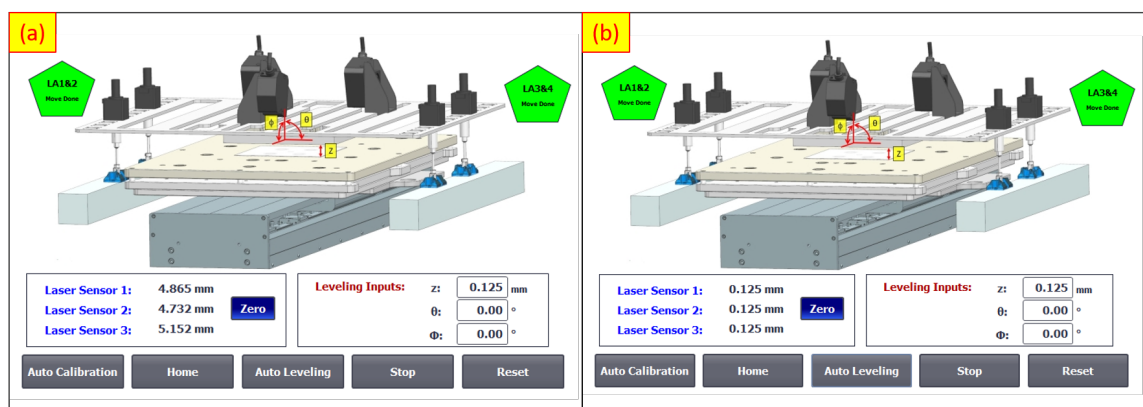


Figure 3.9 (a) The reading of laser sensors when they were in range. (b) The reading of laser sensors after the spacing was adjusted to the 0.125 mm set point.

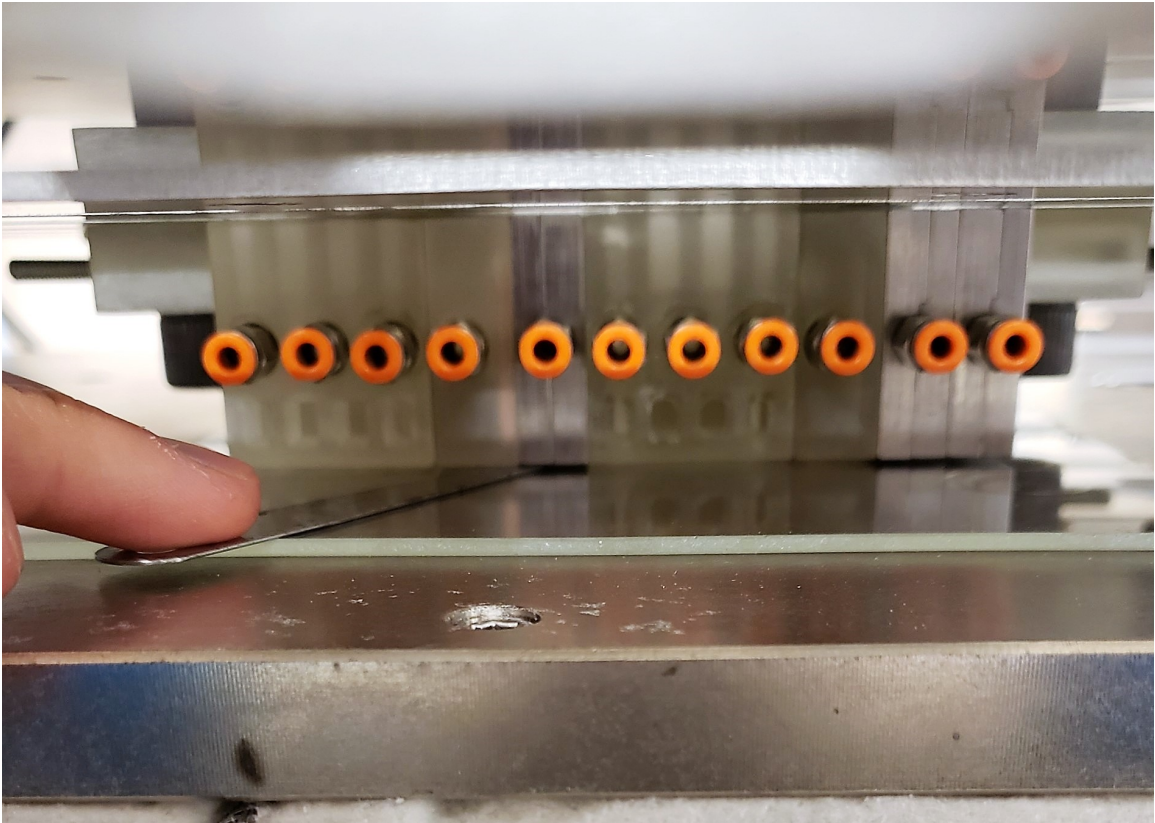


Figure 3.10 A 0.1 mm shim was used to check the spacing.

3.5 Leak Test on Gas Sub-system

The goal of this test was to ensure there was no leak in the gas lines. This is because any leak would cause a pressure drop, affect flow delivered to the reactor head, leak chemicals in the upper cabinet, and allow atmospheric air to enter the lines and react with the chemicals. Figure 3.11 shows a schematic of the test setup with the MFCs bypassed and a flow meter attached between the nitrogen supply from the tank and main supply manifold (that distributes nitrogen evenly to the MFCs). Figure 3.12 is the actual setup of the bubbling panel based on the schematic.

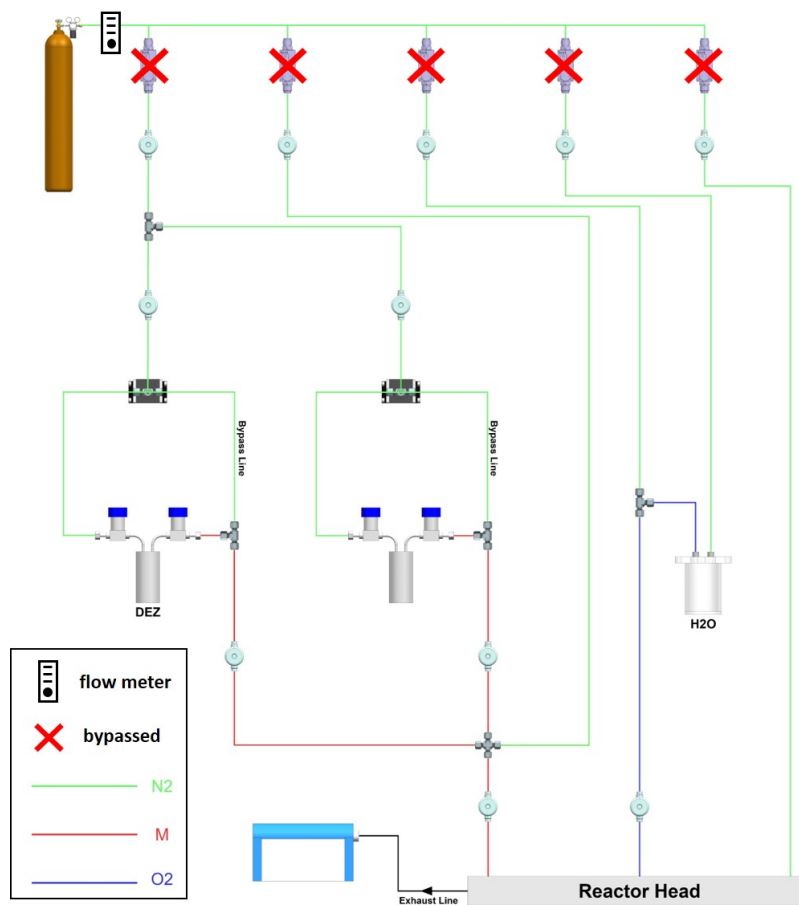


Figure 3.11 A schematic of the bubbling panel with the MFCs removed and a flow meter attached for the leak test.



Figure 3.12 MFCs were dismantled from the bubbling panel for the leak test.

Figure 3.13 shows the positions of the ball indicator if the lines stay pressurized (a) or have leaks (b). The ball indicator inside the flow meter stays at the top position due to the pressure if the lines are pressurized, but it will drop due to gravity if there is a leak and the pressure in the lines is not maintained. For the leak test, all the pneumatic valves are opened, except those at the end of the lines. The different gas lines that make up the gas system were isolated and tested one by one.

Once the lines are pressurized and the end valves closed, the nitrogen supply was turned off. The ball indicator's position in the flow meter was observed for five minutes. The ball indicator did not drop for four minutes, but it dropped in the fifth minute. The minor leakage was identified at the connectors of the water bubbler using soapy water, as shown in Figure

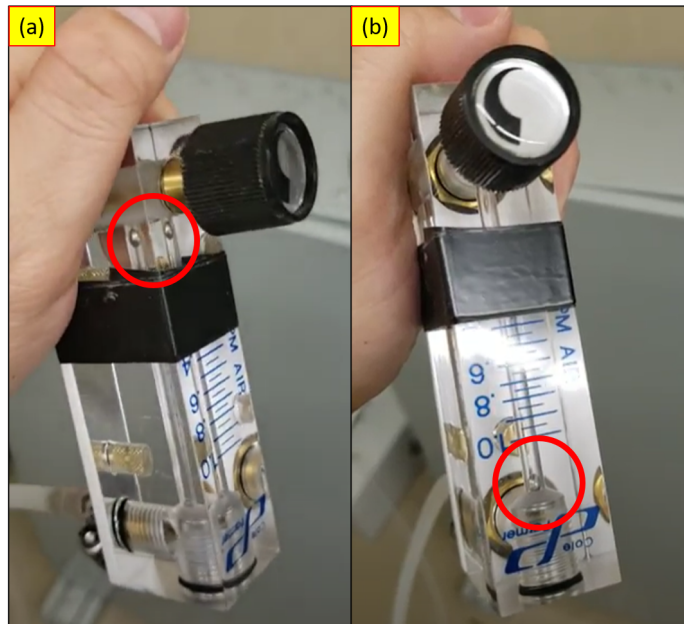


Figure 3.13 (a) The position of the ball indicator if the lines stay pressurized. (b) The position of the ball indicator if there is a leak in the line.

3.14. There was no leak anywhere else when the water line was isolated. It was verified with soapy water at the joints and fittings. The leakage from the water bubbler originated from cracks at the threads. It was found that acrylic material was used to make the water bubbler instead of the intended material (polycarbonate). Acrylic is more prone to crack as compared to polycarbonate, which would seal well for our application. The water bubbler will have to be re-made. The current water bubbler can still be used in the meantime since air leakage into the water line is not a safety hazard.

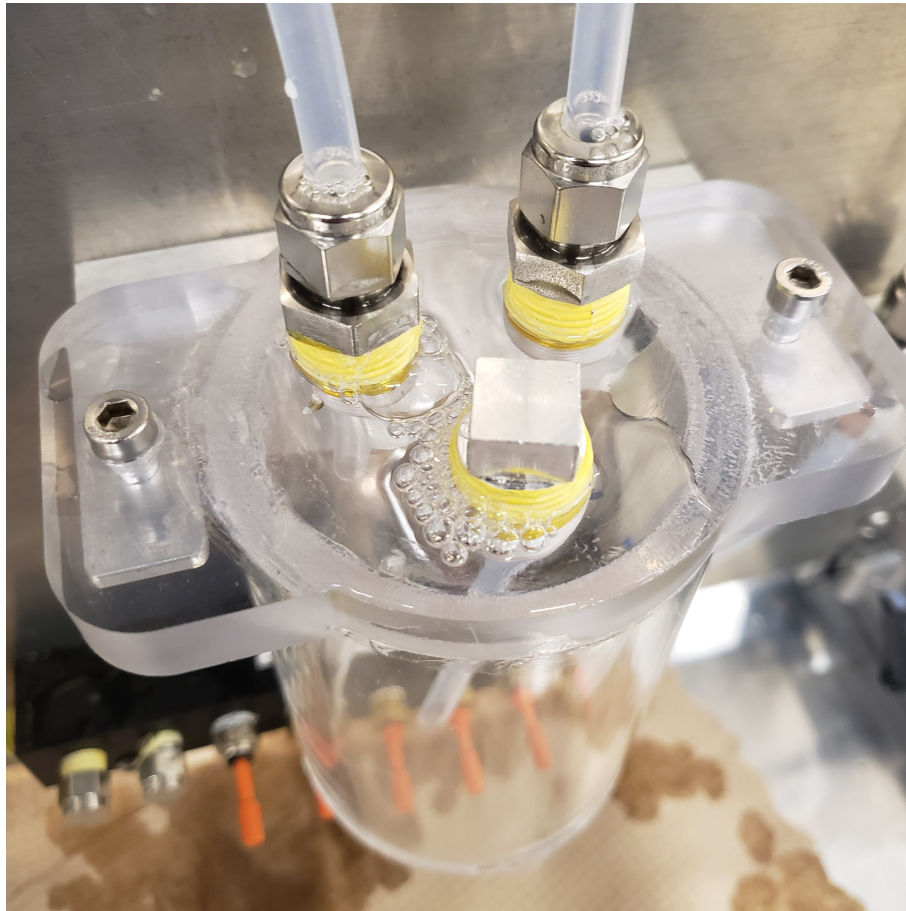


Figure 3.14 There was a minor leakage at the water bubbler.

3.6 Flow Test on Reactor Head Sub-system

The goal of this test was to make sure there are flows coming out of the reactor head. This test was conducted after the leak test to ensure that any issues could be attributed to the reactor head's slits themselves. For the test, the reactor head was moved all the way up to create space for the hand to feel flow coming out of the reactor head. For the metal line, it had flow from the carrier gas only since the metal bubbler was not set up at this point.

Figure 3.15 shows the bottom of the reactor head, where the flows are coming out for deposition. Each line was tested individually and the flow underneath each corresponding slit was checked. All flows could be felt when a hand was placed underneath the reactor head. The exhaust slits were weak at the reactor level, but the suction was felt to be sufficient at the manifold level. However, this test could be subjective and inaccurate. A better test is required to detect the flow coming out from the slits in the future. The uniformity of the flow can be determined through actual film deposition. The other options that can be considered for detecting the flow are:

1. Submerging the bottom of the slits in water to observe any bubbles if a flow is present.
2. Setting up Schlieren imaging to visualize the flow of fluid coming out of the slits based on its varying density.

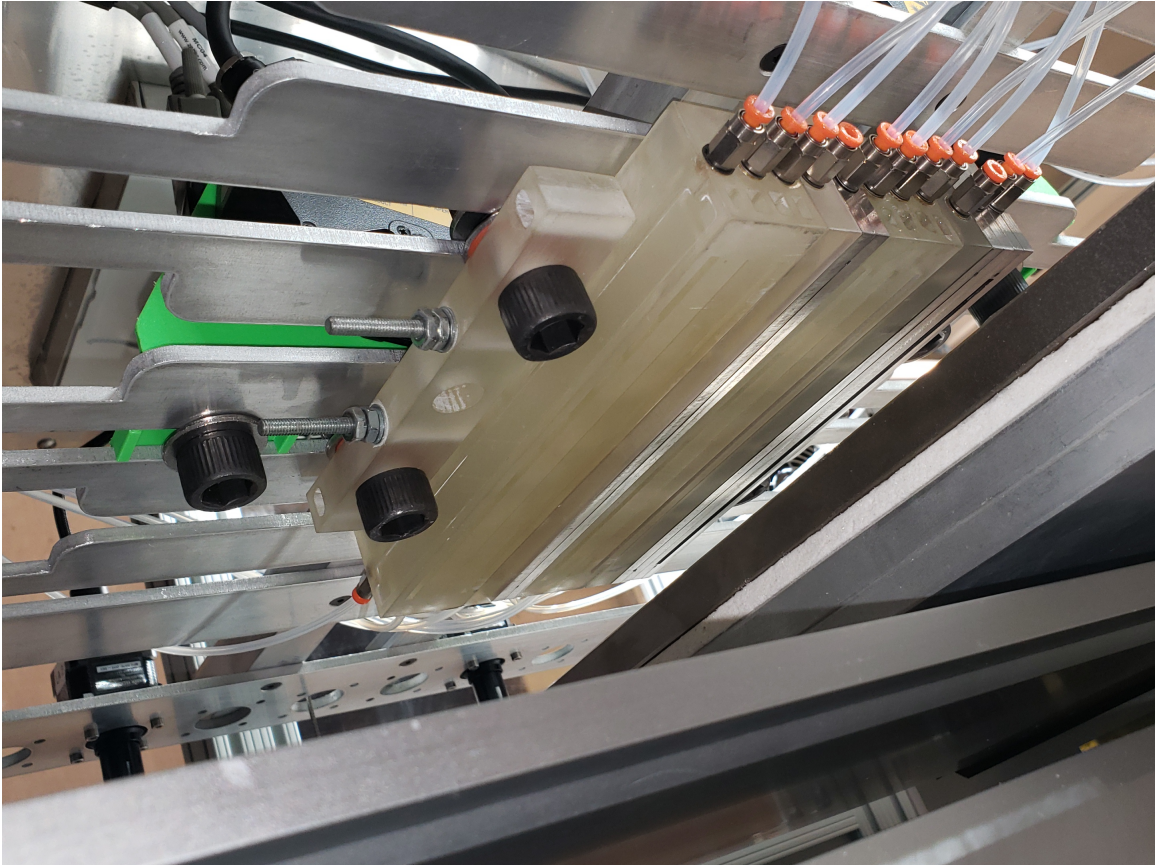


Figure 3.15 A bottom view of the actual reactor.

3.7 System Level Testing and Safety

The goal of this test was to check for all potential faulting scenarios and ensure safety protocol is well established. For instance, the system will fault if a MFC is not reading any flow. The system will stop the deposition if any of the enclosure exhaust fans fails. If the safety fails, the power to the pneumatic manifold will be cut, which will turn off all pneumatic valves. If the door is opened without requesting permission from the system, the system will go to the Aborted state and cut all the power supplies. All these scenarios were tested and they behaved as expected.

Multiple cycles of system level testing were performed to test all the components and no issues were observed, except for the MFC for the water carrier line. All MFCs are calibrated to 45 psi pressure differential between the inlet and outlet, and 1/4" tubing is to be used for accurate operations. At 45 psi, the MFC was having trouble reaching its maximum allowable flow rate. It could only reach 9300 sccm instead of 10,000 sccm. After some troubleshooting, the problem was found to be at the 1/4" to 1/8" reducer connector. The tube size's transition caused backflow that reduced the pressure differential in the water carrier line. The issue was worsened by the type of ferrules used on the 1/8" tee near the outlet as shown in Figure 3.16. Brass ferrules were used originally, which squeezed the Teflon tubes too hard and pinched the tubes. This pinching issue further reduced the inner diameter of the 1/8" tube and restricted the flow. Switching the brass ferrules to Teflon ferrules solved the pinching issue, and the system could operate as expected at maximum flow rates with 45 psi.

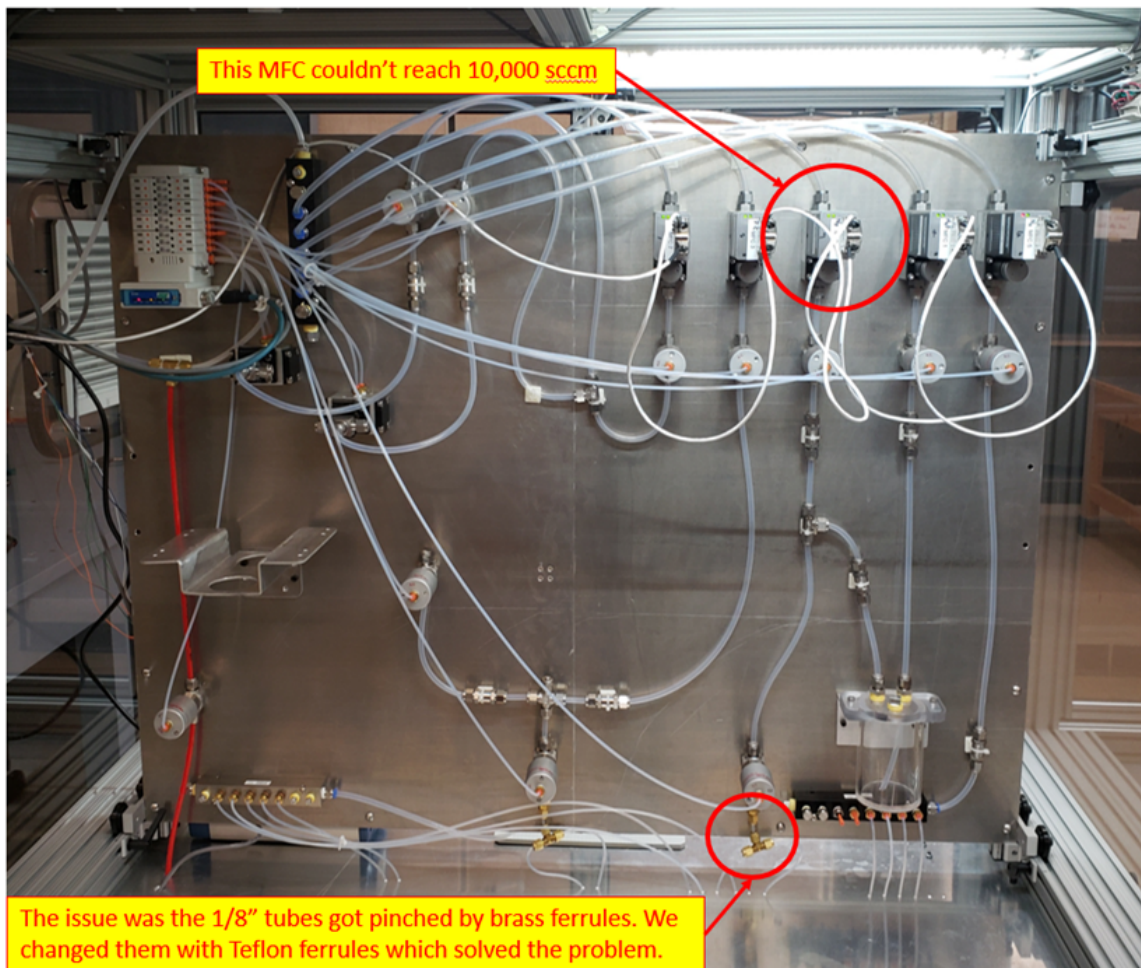


Figure 3.16 Pressure issue with one MFC for water carrier line.

3.8 Film Deposition Test and Performance Validation

The goal of this test was to check if the system would be able to produce a film after all the tests above were conducted. The performance of the system based on the features listed in Section 1.5 of Chapter 1 will be discussed in this section. The system was designed with industrial standards in mind. For example, all the electrical components were set up to meet CSA certification, while all the mechanical components were designed to pass hazardous gas certification. The first test of the film deposition was conducted on July 27, 2020 with Jhi Yong Loke and Prof. Kevin Musselman. All the gas lines were purged with nitrogen, especially the metal gas line, to remove atmospheric air before we connected the metal bubbler. The metal bubbler contained diethylzinc (DEZ) liquid precursor, which is a pyrophoric chemical that requires extra precaution and personal protective equipment, such as face shield, chemical gloves, and lab coat, during handling. The parameters used for the first film are tabulated in Table 3.2. These values were determined based on the values used for zinc oxide deposition using the lab-scale AP-SALD system. The flow rates were scaled four times due to our larger slit design to coat larger area.

Table 3.2 The parameters used for the first film deposition on a 150 mm x 150 mm x 2 mm borosilicate glass.

Parameters	Value and Description
Precursor concentration	15% (90 sccm bubbling flow + 510 sccm carrier flow)
Nitrogen curtain	2400 sccm
Oscillation number	167
Oscillation speed	30 mm/s
Reactor head-substrate spacing	0.15 mm
Temperature	170°C
Exhaust pressure	-0.4 bar

Figure 3.17 shows a picture of the zinc oxide film deposited on a 150 mm x 150 mm x 2 mm borosilicate glass substrate during the first test deposition. The scratch mark on the right side of the film was caused by the interference of the reactor head with the substrate.

This result proves the system's ability to deposit nanoscale films over large areas.

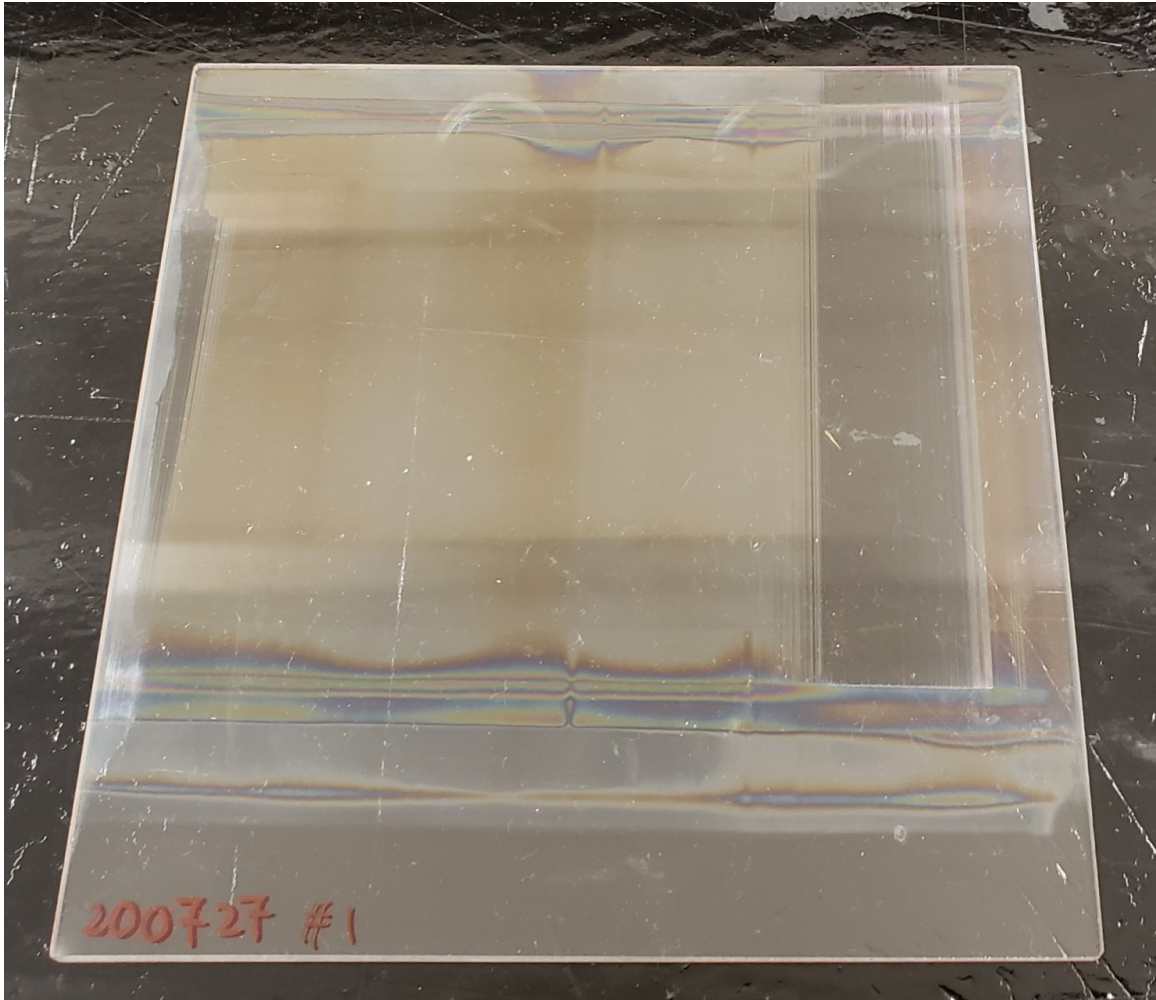


Figure 3.17 The first film made with the pilot-scale industrial AP-SALD system.

After a few testings, Jhi Yong Loke and I were able to obtain a decent film that is quite uniform as shown in Figure 3.18 with parameters in Table 3.3.

Table 3.3 The parameters used for the uniform film deposition on a 150 mm x 150 mm x 2 mm borosilicate glass.

Parameters	Value and Description
Precursor concentration	15% (60 sccm bubbling flow + 340 sccm carrier flow)
Nitrogen curtain	4800 sccm
Oscillation number	400
Oscillation speed	800 mm/s
Reactor head-substrate spacing	0.2 mm
Temperature	170°C
Exhaust pressure	-0.4 bar

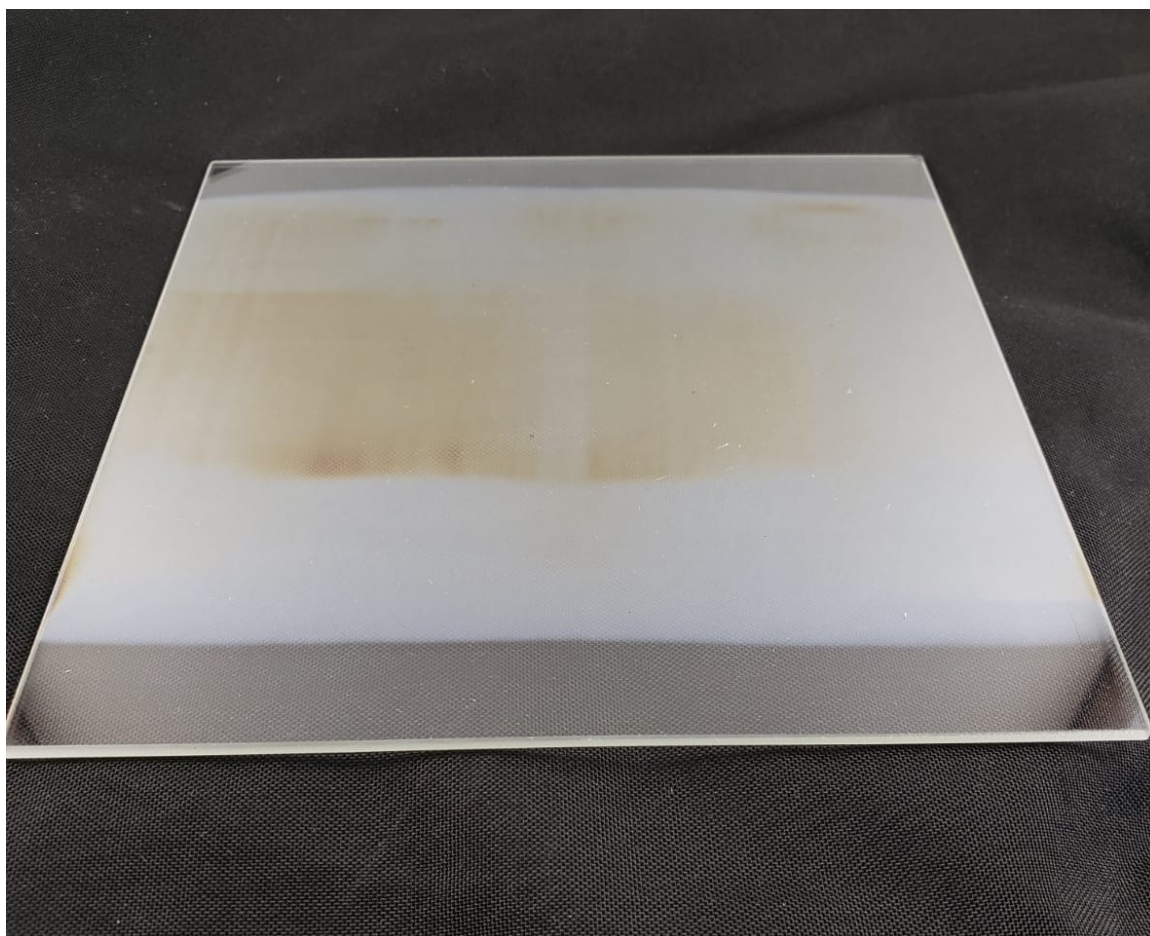


Figure 3.18 The uniform film made with the pilot-scale industrial AP-SALD system.

Some of the parameters were adjusted to improve and optimize the film. The speed was

set to 800 mm/s which is 26 times higher than the first test deposition. The thickness of the film is estimated to be less than 100 nm based on the color of the film. Based on these results, it proves that AP-SALD is a promising open-air nanomanufacturing technique that can deposit ultrathin films at high speed. The capacity of the AP-SALD system to deposit different materials on different type of substrates will be further explored and validated in future experiments.

Chapter 4

Conclusions

A pilot-scale industrial AP-SALD system was successfully designed and built from scratch in Dr. Kevin Musselman's lab at the University of Waterloo. It aims to produce large area, high quality ultrathin films at 100x the speed of conventional ALD. A zinc oxide thin film was successfully deposited on a large borosilicate glass substrate with the system at high speed. The system cabinet is provided with continuous exhaust ventilation by three 169 CFM filter fans to prevent the buildup of any harmful gases. The airflow in the cabinet is monitored by an airflow monitor sensor, as is the pressure in the exhaust line. Both monitoring devices are interlocked with Siemens PLC, which is the main controller of the system. The gas sub-system includes the equipment required to create gases of the precursor chemicals (bubblers, bubbler heaters), to control the flow rate (mass flow controllers) and to distribute the gases (valves, tubing, etc.). A pneumatic manifold is used to control the distribution of compressed air to the corresponding pneumatic valves based on the PLC program. The reactor head consists of multiple gas and exhaust slits stacked horizontally. It was designed with modularity and scalability in mind. The modularity of the reactor design enables high throughput and functional flexibility. CFD simulations were conducted

to guide the design of the reactor. The important criteria in evaluating the reactor design for ALD mode deposition based on CFD were precursor gases isolation and flow uniformity. Experiments with film deposition will be conducted to validate the CFD results. A heating stage was designed and built to heat the substrates to a certain temperature for the precursor gases to react at the surface of the substrates. A heater controller box was built to control the heating through the connection with the PLC. A built-in temperature process program from Siemens PLC is used to configure the parameters of the PID controller for the heater. The linear stage consists of an Akribis stage and a Mitutoyo granite slab to enable high moving stage speeds for high deposition rates to achieve high throughputs. A 3rd order motion profile is used to limit the jerk in the system. A Galil DMC motion controller and a Kollmorgen AKD servo drive were used to control and drive the Akribis stage. An industrial controller with input/output (I/O) modules to communicate with the various system components was used to develop the control system of the AP-SALD. All software and HMI for the AP-SALD system were written in Tia Portal V15.1. The system is fully automated and optimized using Siemens PLC and built to meet industrial standards.

Before starting to run experiments with actual chemicals, multiple dry runs were carried out with a series of tests to examine and verify the system's performance and program's reliability and repeatability. The linear stage movement test was conducted to validate the performance and programs of the linear stage. The maximum speed of the linear stage was determined to be 1350 mm/s and the performance of the linear stage was reliable and consistent. The vacuum suction of the stage was also strong enough to hold the substrates during the oscillations at maximum speed. The heater performed well too and was able to heat up to a desired temperature with a ramp rate of 12 °C/min, while the surrounding environment and linear stage's motor remained cool. From the assembled reactor head test, it was found that it is hard to keep individual slits well aligned. The substrate stage's flatness was not uniform based on the profile plotted by the laser sensor's

measurements, but the height variation was acceptable for initial film deposition testing. The auto-leveling program worked well with the laser sensors and linear actuators, but the reactor head-substrate spacing was mainly affected by the defects in assembling the mechanical parts. For the gas sub-system, a small leak was found at the connectors of the water bubbler, but it was not a safety hazard and no other leak was found anywhere else. Flows from the reactor head's slits could be sensed, but its flow uniformity is yet to be determined through film deposition. Multiple cycles of system level testing were performed to test all the devices and no major issues were observed.

4.1 Future Work

The next phase of the project is to run experiments and optimize ZnO films on borosilicate glass and FTO glass. The parameters of deposition recipes need to be studied and optimized for making the films. It would be interesting to study other materials such as aluminum oxide (Al_2O_3), copper oxide (Cu_2O), and tin oxide (SnO_2) using other precursors. Other substrate materials, such as fabrics and plastics, can be tested for film deposition to explore other applications. The next material test will be driven by the potential industrial collaborations to serve as a proof of concept to validate the value propositions of AP-SALD, such as its promised high deposition rate, its ability to produce large area films with high quality (uniform and conformal), and the atmospheric operation without the need of a vacuum chamber. Further technical development is required to obtain more proof of AP-SALD's technology capabilities.

The current reactor head is made for one substrate width. It would be particularly useful to make the reactor slits longer so that it that can deposit two substrates side by side in one pass. More slits can be added to speed up the deposition by increasing the number of ALD cycles in one pass. The channel geometry of the reactor head's slits can also be customized to certain flow patterns, which may be applicable to develop selective area spatial atomic layer deposition. SLA 3D printing will be used for printing slits with different lengths and channel geometries for rapid prototyping. To allow for low temperature deposition on certain substrate materials such as polymers, a Surface Dielectric Barrier Discharge (SDBD) plasma slit can be integrated to the reactor head to produce reactive plasma species, such as electronic excited states, radicals and ions, to react with certain precursors [45]. The assembling mechanism of the reactor head slits needs to be improved since the current clamping method is not sufficient to hold individual slits in place. The height of each slits can be adjusted relative to adjacent slits. It would be interesting to see the effect of this

parameter on the film deposition.

The flatness of the heating stage can be improved by using spacers with different heights based on the height variations captured by the laser sensors. The granite slab shifted due to the movement of the linear stage and it has to be re-positioned. A foam was placed under the granite slab to act as a cushion between the slab and the floor. However, the foam could not provide enough gripping force to prevent the linear stage from shifting. It can be changed with a rubber mat or removed and replaced with brackets that can constrain the linear stage's movement. For the safety system, the interlock connection between the VentAlert and PLC still requires troubleshooting. A safety interlock will be added to the doors of the upper cabinet to provide easy access to the users.

References

- [1] K. P. Musselman, C. F. Uzoma, M. S. Miller, Nanomanufacturing: high-throughput, cost-effective deposition of atomic scale thin films via atmospheric pressure spatial atomic layer deposition, *Chemistry of Materials* 28 (2016) 8443–8452.
- [2] S. M. George, Atomic layer deposition: an overview, *Chemical reviews* 110 (2010) 111–131.
- [3] V. Miikkulainen, M. Leskelä, M. Ritala, R. L. Puurunen, Crystallinity of inorganic films grown by atomic layer deposition: Overview and general trends, *Journal of Applied Physics* 113 (2013) 2.
- [4] M. R. Shaeri, T.-C. Jen, C. Y. Yuan, M. Behnia, Investigating atomic layer deposition characteristics in multi-outlet viscous flow reactors through reactor scale simulations, *International Journal of Heat and Mass Transfer* 89 (2015) 468–481.
- [5] D. Pan, L. Ma, Y. Xie, T. C. Jen, C. Yuan, On the physical and chemical details of alumina atomic layer deposition: A combined experimental and numerical approach, *Journal of Vacuum Science & Technology A: Vacuum, Surfaces, and Films* 33 (2015) 021511.
- [6] P. O. Oviroh, R. Akbarzadeh, D. Pan, R. A. M. Coetzee, T.-C. Jen, New development of atomic layer deposition: processes, methods and applications, *Science and technology of advanced materials* 20 (2019) 465–496.
- [7] T. Weckman, K. Laasonen, Atomic layer deposition of zinc oxide: diethyl zinc reactions and surface saturation from first-principles, *The Journal of Physical Chemistry C* 120 (2016) 21460–21471.
- [8] H. Kim, W.-J. Maeng, et al., Applications of atomic layer deposition to nanofabrication and

emerging nanodevices, *Thin Solid Films* 517 (2009) 2563–2580.

- [9] K. J. Kanarik, J. Marks, H. Singh, S. Tan, A. Kabansky, W. Yang, K. Taeseung, D. M. Hausmann, T. Lill, Integrating atomic scale processes: Ald (atomic layer deposition) and ale (atomic layer etch), 2017. US Patent 9,576,811.
- [10] X. Meng, Y.-C. Byun, H. S. Kim, J. S. Lee, A. T. Lucero, L. Cheng, J. Kim, Atomic layer deposition of silicon nitride thin films: a review of recent progress, challenges, and outlooks, *Materials* 9 (2016) 1007.
- [11] B. Yan, X. Li, Z. Bai, X. Song, D. Xiong, M. Zhao, D. Li, S. Lu, A review of atomic layer deposition providing high performance lithium sulfur batteries, *Journal of Power Sources* 338 (2017) 34–48.
- [12] Y. S. Jung, A. S. Cavanagh, L. A. Riley, S.-H. Kang, A. C. Dillon, M. D. Groner, S. M. George, S.-H. Lee, Ultrathin direct atomic layer deposition on composite electrodes for highly durable and safe li-ion batteries, *Advanced Materials* 22 (2010) 2172–2176.
- [13] X. Meng, X.-Q. Yang, X. Sun, Emerging applications of atomic layer deposition for lithium-ion battery studies, *Advanced Materials* 24 (2012) 3589–3615.
- [14] L. Ma, R. B. Nuwayhid, T. Wu, Y. Lei, K. Amine, J. Lu, Atomic layer deposition for lithium-based batteries, *Advanced Materials Interfaces* 3 (2016) 1600564.
- [15] H. Knoops, M. Donders, M. Van De Sanden, P. Notten, W. Kessels, Atomic layer deposition for nanostructured li-ion batteries, *Journal of Vacuum Science & Technology A: Vacuum, Surfaces, and Films* 30 (2012) 010801.
- [16] J. Van Delft, D. Garcia-Alonso, W. Kessels, Atomic layer deposition for photovoltaics: applications and prospects for solar cell manufacturing, *Semiconductor Science and Technology* 27 (2012) 074002.
- [17] D. Muñoz-Rojas, V. H. Nguyen, C. M. de la Huerta, S. Aghazadehchors, C. Jiménez, D. Bellet, Spatial atomic layer deposition (sald), an emerging tool for energy materials. application to new-generation photovoltaic devices and transparent conductive materials, *Comptes Rendus Physique* 18 (2017) 391–400.

- [18] W. Niu, X. Li, S. K. Karuturi, D. W. Fam, H. Fan, S. Shrestha, L. H. Wong, A. I. Y. Tok, Applications of atomic layer deposition in solar cells, *Nanotechnology* 26 (2015) 064001.
- [19] A. F. Palmstrom, P. K. Santra, S. F. Bent, Atomic layer deposition in nanostructured photovoltaics: tuning optical, electronic and surface properties, *Nanoscale* 7 (2015) 12266–12283.
- [20] C. Barbos, D. Blanc-Pelissier, A. Fave, C. Botella, P. Regreny, G. Grenet, E. Blanquet, A. Crisci, M. Lemiti, Al₂O₃ thin films deposited by thermal atomic layer deposition: Characterization for photovoltaic applications, *Thin Solid Films* 617 (2016) 108–113.
- [21] P. Poodt, D. C. Cameron, E. Dickey, S. M. George, V. Kuznetsov, G. N. Parsons, F. Roozeboom, G. Sundaram, A. Vermeer, Spatial atomic layer deposition: A route towards further industrialization of atomic layer deposition, *Journal of Vacuum Science & Technology A: Vacuum, Surfaces, and Films* 30 (2012) 010802.
- [22] R. J. Narayan, S. P. Adiga, M. J. Pellin, L. A. Curtiss, A. J. Hryn, S. Stafslin, B. Chisholm, C.-C. Shih, C.-M. Shih, S.-J. Lin, et al., Atomic layer deposition-based functionalization of materials for medical and environmental health applications, *Philosophical Transactions of the Royal Society A: Mathematical, Physical and Engineering Sciences* 368 (2010) 2033–2064.
- [23] A. Abou Chaaya, M. Le Poitevin, S. Cabello-Aguilar, S. Balme, M. Bechelany, S. Kraszewski, F. Picaud, J. Cambedouzou, E. Balanzat, J.-M. Janot, et al., Enhanced ionic transport mechanism by gramicidin a confined inside nanopores tuned by atomic layer deposition, *The Journal of Physical Chemistry C* 117 (2013) 15306–15315.
- [24] N. Van Doremalen, T. Bushmaker, D. H. Morris, M. G. Holbrook, A. Gamble, B. N. Williamson, A. Tamin, J. L. Harcourt, N. J. Thornburg, S. I. Gerber, et al., Aerosol and surface stability of sars-cov-2 as compared with sars-cov-1, *New England Journal of Medicine* 382 (2020) 1564–1567.
- [25] S. L. Warnes, Z. R. Little, C. W. Keevil, Human coronavirus 229e remains infectious on common touch surface materials, *MBio* 6 (2015).
- [26] S. L. Warnes, E. N. Summersgill, C. W. Keevil, Inactivation of murine norovirus on a range of copper alloy surfaces is accompanied by loss of capsid integrity, *Applied and environmental*

microbiology 81 (2015) 1085–1091.

- [27] H. Ghaffari, A. Tavakoli, A. Moradi, A. Tabarraei, F. Bokharaei-Salim, M. Zahmatkeshan, M. Farahmand, D. Javanmard, S. J. Kiani, M. Esghaei, et al., Inhibition of h1n1 influenza virus infection by zinc oxide nanoparticles: another emerging application of nanomedicine, *Journal of biomedical science* 26 (2019) 1–10.
- [28] J. Hodek, V. Zajíčová, I. Lovětinská-Šlamborová, I. Stibor, J. Müllerová, J. Weber, Protective hybrid coating containing silver, copper and zinc cations effective against human immunodeficiency virus and other enveloped viruses, *BMC microbiology* 16 (2016) 1–12.
- [29] G. Borkow, H. H. Lara, C. Y. Covington, A. Nyamathi, J. Gabbay, Deactivation of human immunodeficiency virus type 1 in medium by copper oxide-containing filters, *Antimicrobial agents and chemotherapy* 52 (2008) 518–525.
- [30] G. Borkow, J. Gabbay, Copper as a biocidal tool, *Current medicinal chemistry* 12 (2005) 2163–2175.
- [31] K. Sunada, M. Minoshima, K. Hashimoto, Highly efficient antiviral and antibacterial activities of solid-state cuprous compounds, *Journal of hazardous materials* 235 (2012) 265–270.
- [32] R. Nakano, H. Ishiguro, Y. Yao, J. Kajioka, A. Fujishima, K. Sunada, M. Minoshima, K. Hashimoto, Y. Kubota, Photocatalytic inactivation of influenza virus by titanium dioxide thin film, *Photochemical & Photobiological Sciences* 11 (2012) 1293–1298.
- [33] J. G. McEvoy, Z. Zhang, Antimicrobial and photocatalytic disinfection mechanisms in silver-modified photocatalysts under dark and light conditions, *Journal of Photochemistry and Photobiology C: Photochemistry Reviews* 19 (2014) 62–75.
- [34] R. L. Hoye, D. Muñoz-Rojas, D. C. Iza, K. P. Musselman, J. L. MacManus-Driscoll, High performance inverted bulk heterojunction solar cells by incorporation of dense, thin zno layers made using atmospheric atomic layer deposition, *Solar energy materials and solar cells* 116 (2013) 197–202.
- [35] A. T. Marin, D. Muñoz-Rojas, D. C. Iza, T. Gershon, K. P. Musselman, J. L. MacManus-Driscoll, Novel atmospheric growth technique to improve both light absorption

- and charge collection in zno/cu₂o thin film solar cells, *Advanced Functional Materials* 23 (2013) 3413–3419.
- [36] R. L. Patel, J. Park, X. Liang, Ionic and electronic conductivities of atomic layer deposition thin film coated lithium ion battery cathode particles, *RSC advances* 6 (2016) 98768–98776.
- [37] S. Neudeck, A. Mazilkin, C. Reitz, P. Hartmann, J. Janek, T. Brezesinski, Effect of low-temperature al₂o₃ coating on ni-rich layered oxide composite cathode on the long-term cycling performance of lithium-ion batteries, *Scientific reports* 9 (2019) 1–11.
- [38] M. Donders, W. Arnoldbik, H. Knoops, W. Kessels, P. Notten, Atomic layer deposition of licoo₂ thin-film electrodes for all-solid-state li-ion micro-batteries, *Journal of The Electrochemical Society* 160 (2013) A3066.
- [39] M. Létiche, E. Eustache, J. Freixas, A. Demortière, V. De Andrade, L. Morgenroth, P. Tilmant, F. Vaurette, D. Troadec, P. Roussel, et al., Atomic layer deposition of functional layers for on chip 3d li-ion all solid state microbattery, *Advanced Energy Materials* 7 (2017) 1601402.
- [40] V. Miikkulainen, A. Ruud, E. Østreg, O. Nilsen, M. Laitinen, T. Sajavaara, H. Fjellvag, Atomic layer deposition of spinel lithium manganese oxide by film-body-controlled lithium incorporation for thin-film lithium-ion batteries, *The Journal of Physical Chemistry C* 118 (2014) 1258–1268.
- [41] A. H. Alshehri, K. Mistry, V. H. Nguyen, K. H. Ibrahim, D. Muñoz-Rojas, M. Yavuz, K. P. Musselman, Quantum-tunneling metal-insulator-metal diodes made by rapid atmospheric pressure chemical vapor deposition, *Advanced Functional Materials* 29 (2019) 1805533.
- [42] K. Mistry, A. Jones, M. Kao, T. W.-K. Yeow, M. Yavuz, K. P. Musselman, In-situ observation of nucleation and property evolution in films grown with an atmospheric pressure spatial atomic layer deposition system., *Nano Express* (2020).
- [43] R. L. Hoye, D. Muñoz-Rojas, S. F. Nelson, A. Illiberi, P. Poodt, F. Roozeboom, J. L. MacManus-Driscoll, Research update: Atmospheric pressure spatial atomic layer deposition of zno thin films: Reactors, doping, and devices, *APL materials* 3 (2015) 040701.
- [44] Tecnotion, Technotion motion simulation tool, 2020. URL: <https://simtool.tecnotion.com/>.

- [45] Y. Creighton, A. van der Bruele, A. Illiberi, F. Roozeboom, P. Poedt, Atmospheric pressure plasma enhanced spatial atomic layer deposition, in: 22nd International Symposium on Plasma Chemistry, 2015, pp. 1–4.

APPENDICES

Appendix A

Design and Construction of a Pilot-Scale Industrial AP-SALD System

A.1 CFD Simulations of Reactor Head

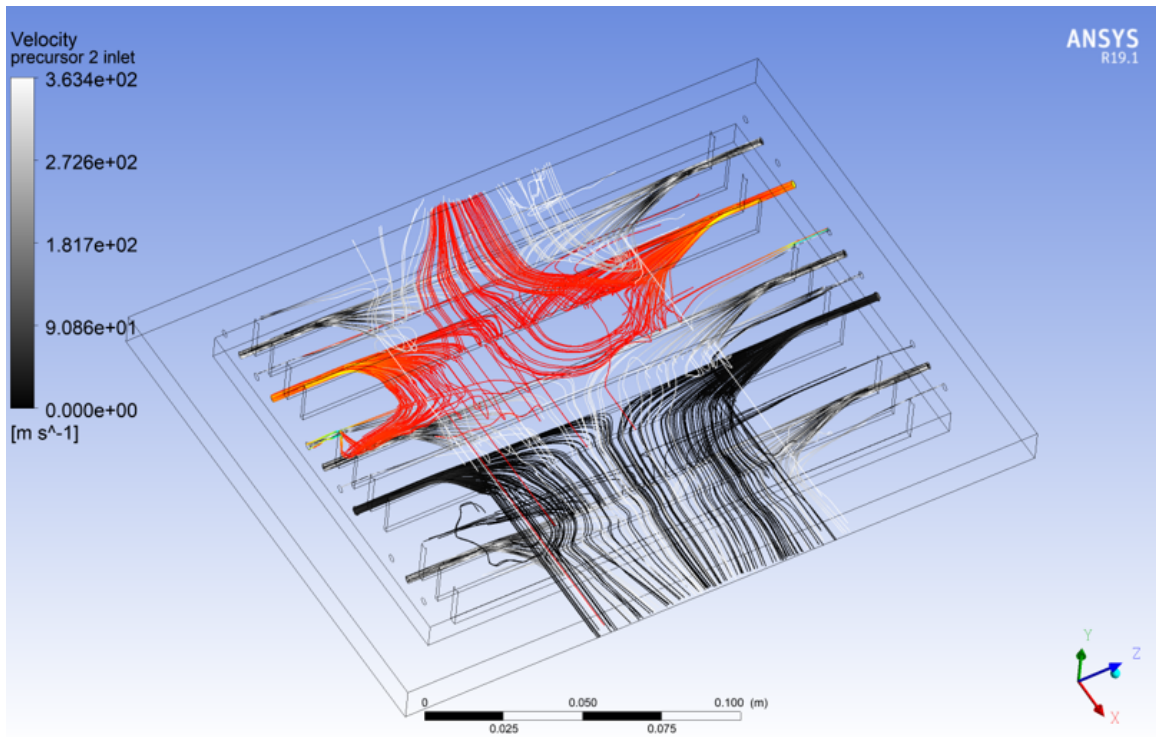


Figure A.1 A 3D CFD simulation result with same parameters as shown in Table 2.1, except reactor head-substrate spacing which 3mm is used in this case.

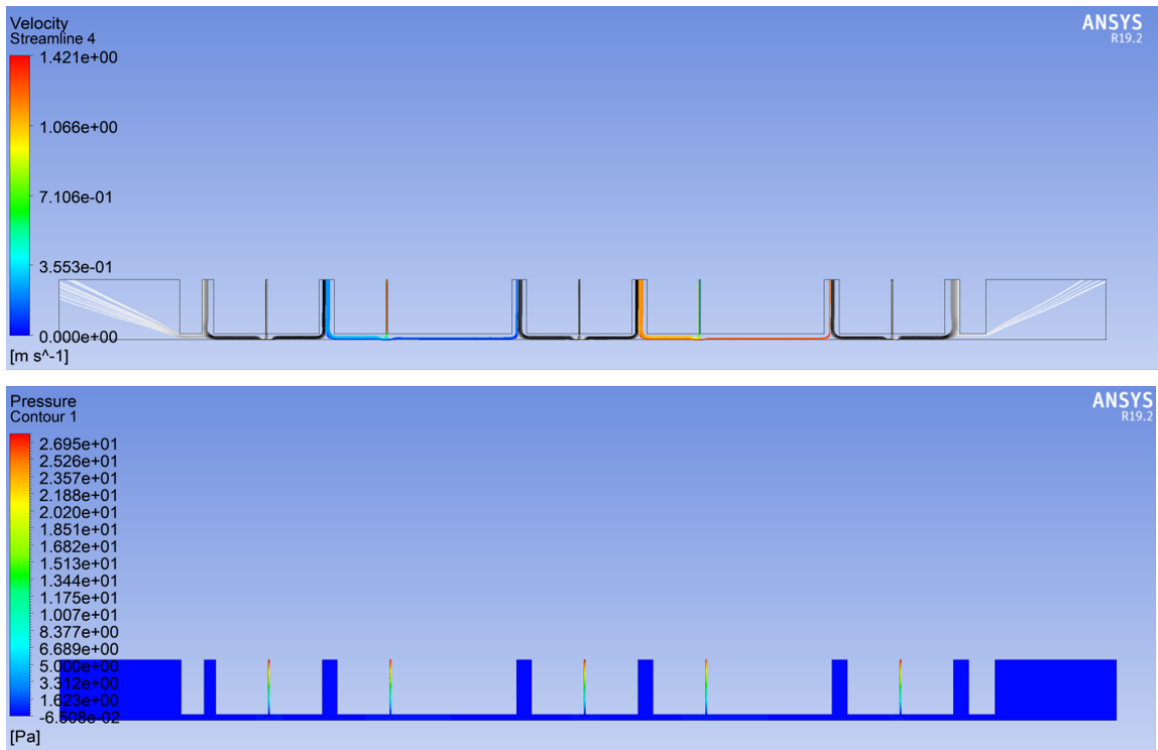


Figure A.2 A 2D CFD simulation result with same parameters as shown in Table 2.1, except reactor head-substrate spacing which 0.45mm is used in this case.

A.2 PID Block Diagram for Temperature Control

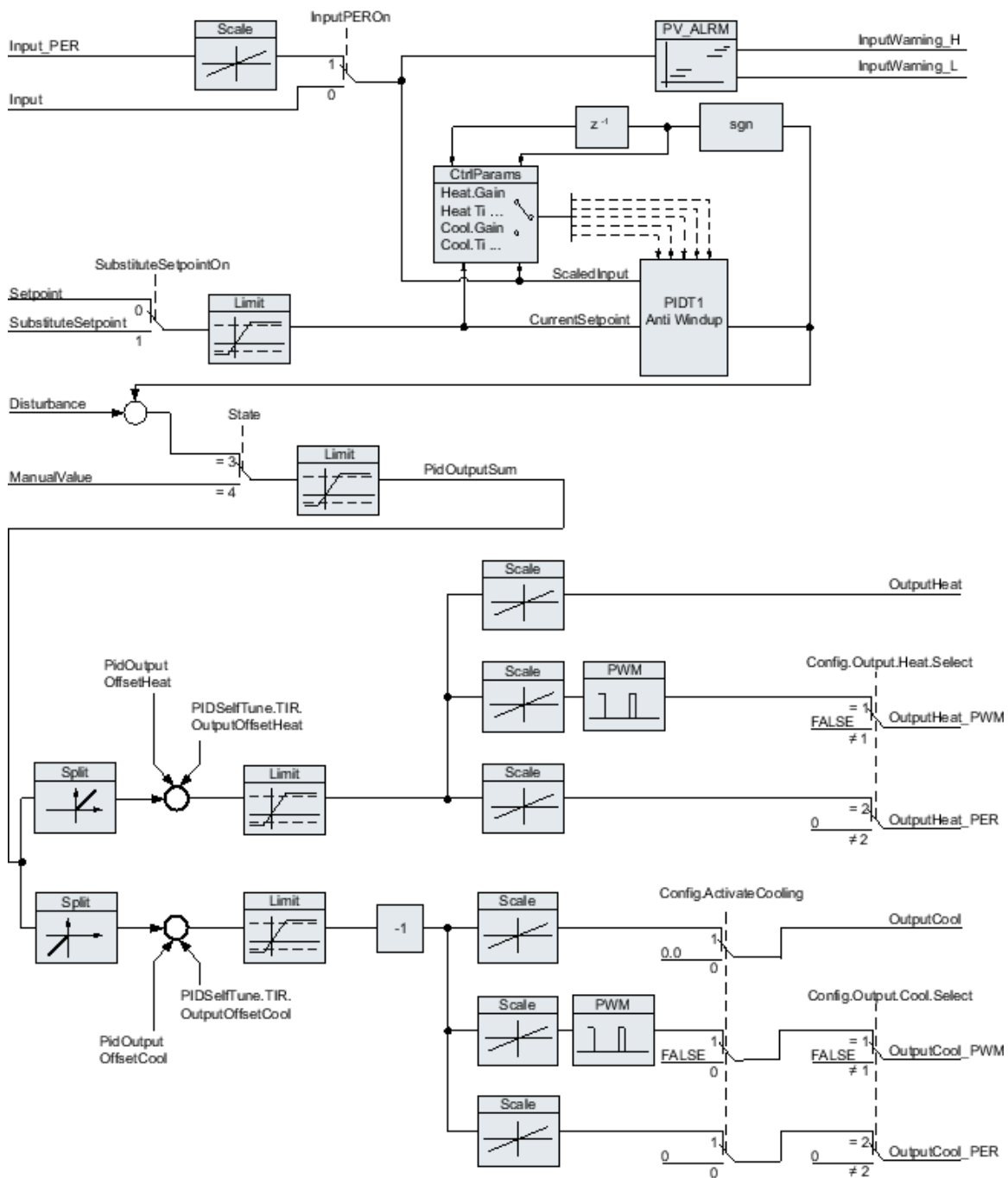


Figure A.3 A screenshot of the PID block diagram from Siemens PLC program for temperature control and process.

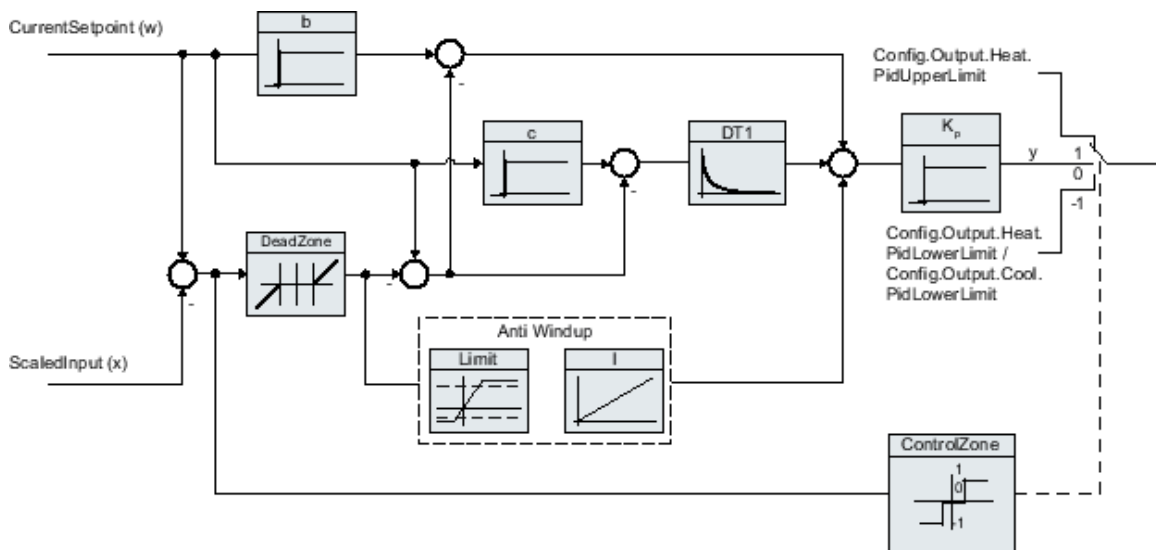


Figure A.4 A screenshot of the PID block diagram with anti-windup from Siemens PLC program for temperature control and process.

A.3 Motion Simulations of the Linear Stage

Application data

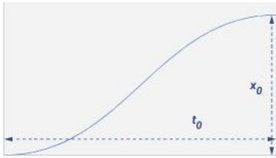
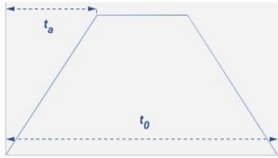

Temperature heatsink	Moving mass	Friction force
40 °C	20.000 kg	20.000 N
Rtherm heatsink	Incliment angle	Power supply
0.05 °K/W	0.000 deg	208.000 V
<input checked="" type="radio"/> AC <input type="radio"/> DC		
Name		
Point to point trapezoidal movement (t3rd)		
Moving distance	Moving time	Acceleration time
0.600 m	0.568 s	0.123 s
Position	Velocity	Acceleration
		
Max. Vdi volts	Load in newtons	
208.000 V	0.000 N	

Figure A.5 Parameters for the simulation in Tecnotion.

A.4 Electrical Components of AP-SALD System

Table A.1 The electrical components used in the AP-SALD system.

Components (Manufacturer)	Description	AP-SALD Usage
CPU 1515SP PC (F/T/TF) (Siemens)	ET 200SP Open Controller	PC-based CPU with fail-safe version
CM PtP (Siemens)	Point-to-point communications module	Mass flow controller's RS485 communication connection to PLC
CM PtP (Siemens)	Point-to-point communications module	Linear actuator's controller 1's RS232 communication connection to PLC
CM PtP (Siemens)	Point-to-point communications module	Linear actuator's controller 2's RS232 communication connection to PLC
F-DI 8x24VDC HF (Siemens)	Fail-safe digital input module	Contactors', eStop's, VentAlert's feedback
F-DI 8x24VDC HF (Siemens)	Fail-safe digital input module	Safety door lock's, contactors', door's feedback
F-DQ 4x24VDC/2A PM HF (Siemens)	Fail-safe digital output module	Heater contactor's, linear stage contactor's, pneumatic manifold's ON/OFF
DI 8x24VDC HF (Siemens)	Digital input module	Button box button's control, flow sensor's feedback, door open's feedback
DQ 8x24VDC/0.5A HF (Siemens)	Digital output module	Button box button's light, buzzer's trigger, door unlock's trigger
AI 4xRTD/TC 2-,3-,4-wire HF (Siemens)	Analog input module	Thermocouple's connections
DQ 8x24VDC/0.5A HF (Siemens)	Digital output module	EStop's button light, flow sensor's power ON/OFF, reactor exhaust pump ON/OFF, enclosure exhaust fan's ON/OFF
DI 8x24VDC HF (Siemens)	Digital input module	Reed sensor's feedback, Kollmorgen AKD drive feedback
Continued on next page		

Table A.1 – continued from previous page

Components (Manufacturer)	Description	AP-SALD Usage
DQ 4x24VDC/2A HS (Siemens)	Digital output module with PWM function	Heater's PWM output, cabinet light's control
DI 8x24VDC HF (Siemens)	Digital input module	Flow sensor's feedback
LK-G5001P (Keyence)	Hi-speed hi-accuracy displacement sensor PNP controller	Laser sensor's controller
LK-HA100 (Keyence)	Hi-speed hi-accuracy displacement sensor PNP controller expansion unit	Laser sensor's controller expansion
AB7670 (HMS)	EtherNet/IP Scanner - PROFINET-IO Device	Laser sensor's communication connection to PLC
EX260-SPN (SMC)	Fieldbus output for SMC's directional control valves	Pneumatic manifold's communication connection to PLC
X-MCB2 (Zaber)	Zaber's X-Series stepper motor controller	Linear actuator's controller 1
X-MCB2 (Zaber)	Zaber's X-Series stepper motor controller	Linear actuator's controller 2
DMC-30010 (Galil)	Single axis motion controller card	Akribis stage's controller and communication connection to PLC
AKD-B00606-NBAN-0000 (Kollmorgen)	AKD series brushless servo drive	Akribis stage's servo drive.

A.5 AP-SALD Human Machine Interface (HMI)

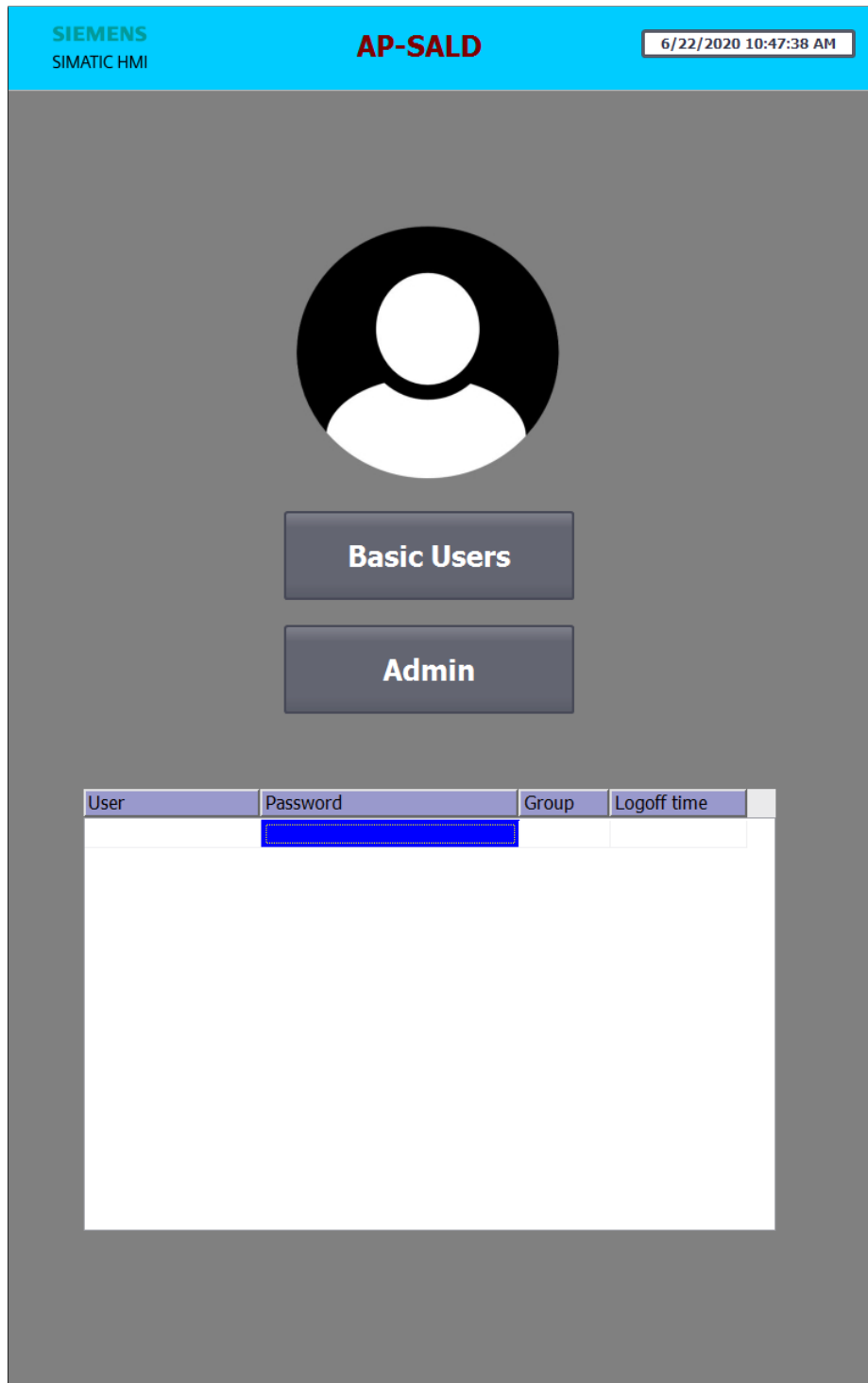


Figure A.6 The log-on page of HMI.

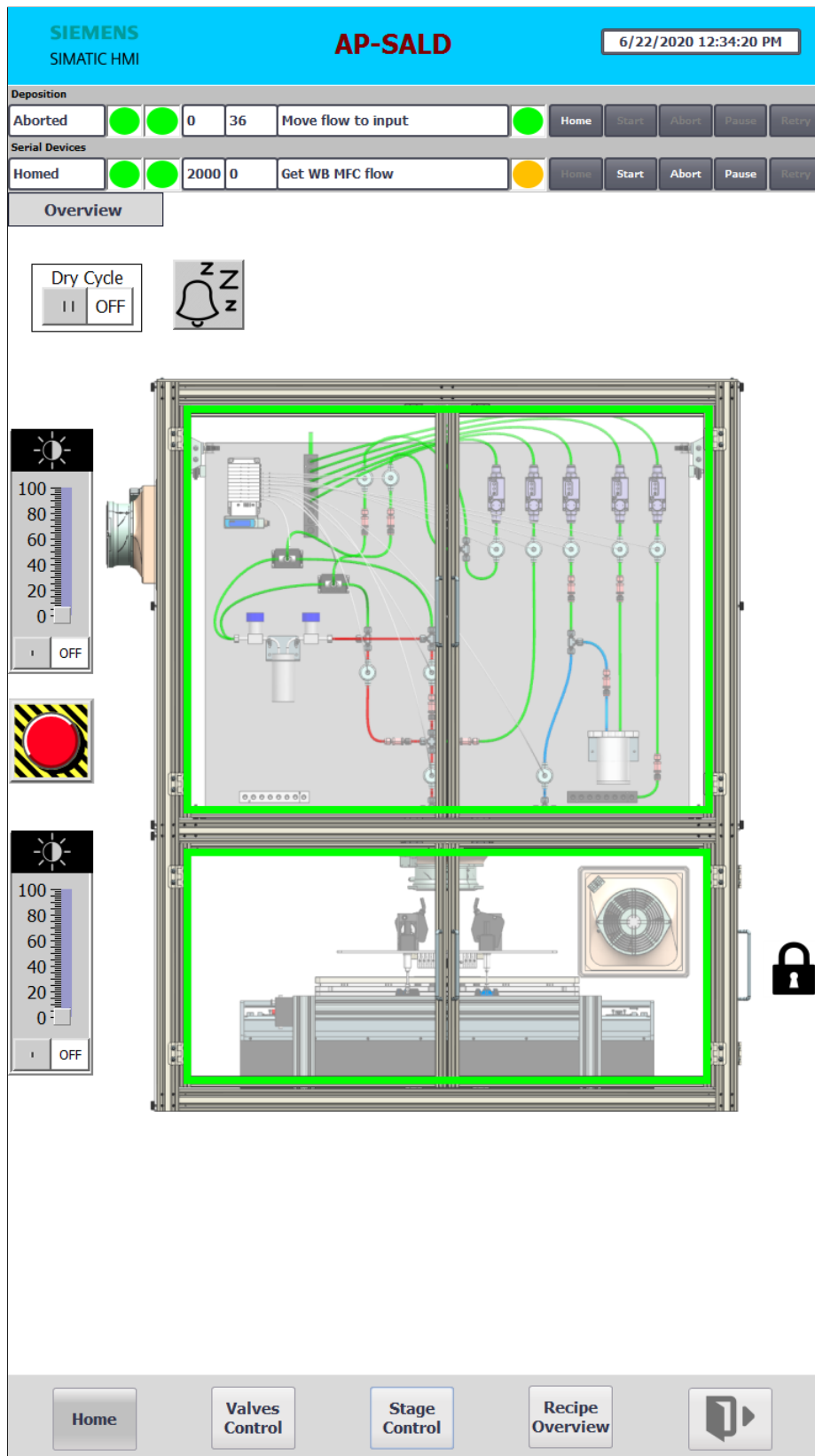


Figure A.7 The home page of HMI.

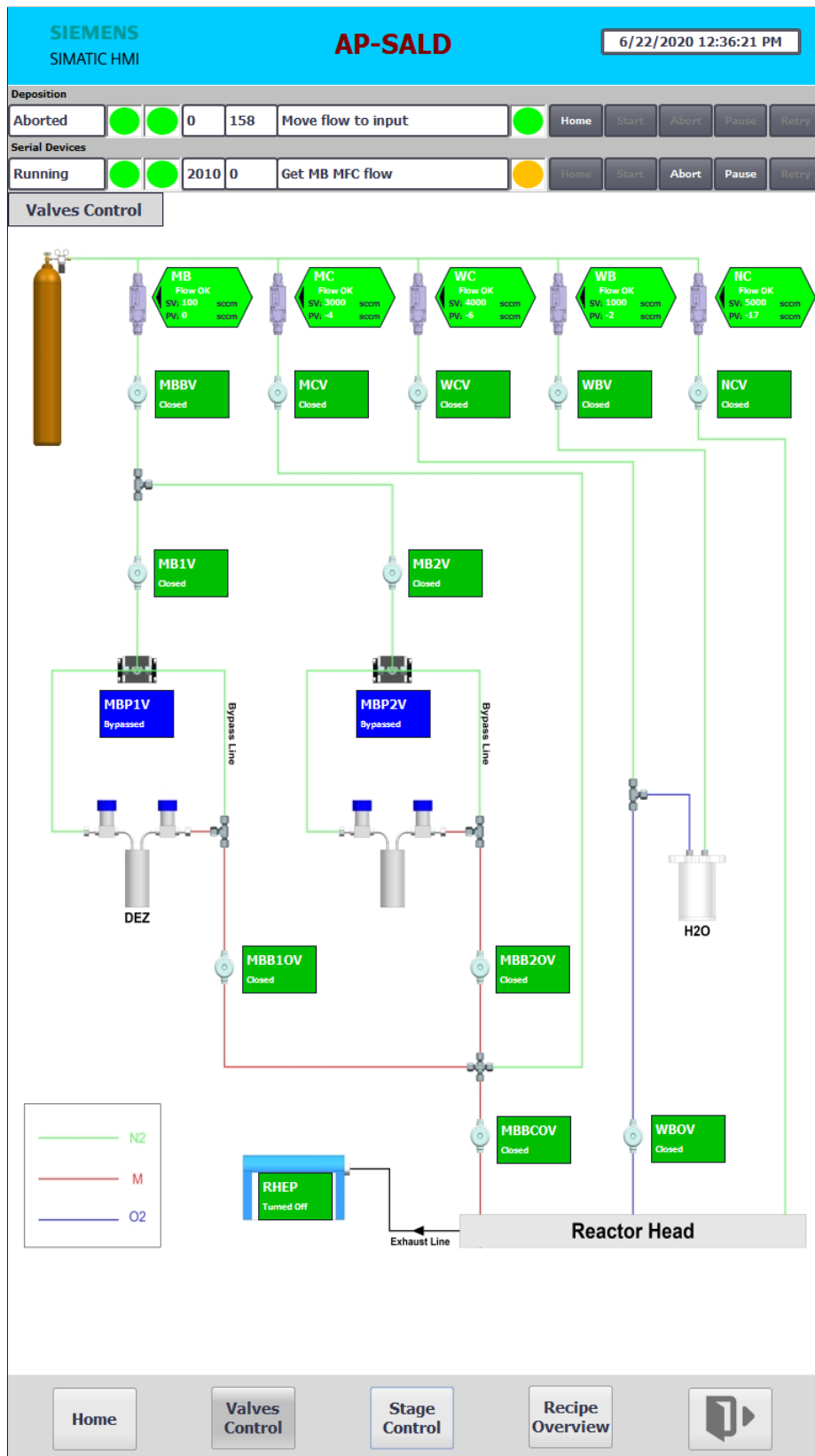


Figure A.8 The flow control page of HMI.

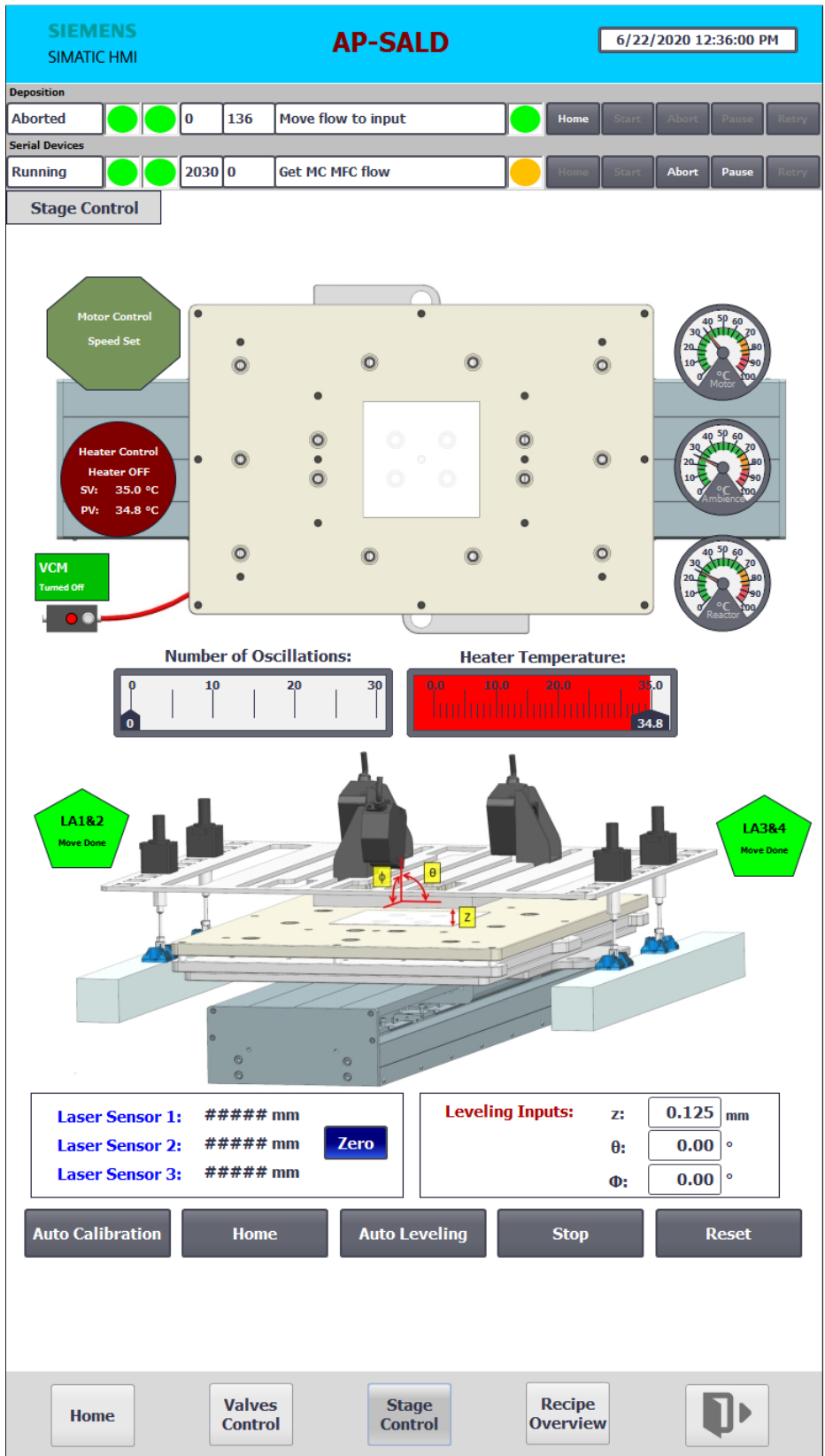


Figure A.9 The stage control page of HMI.

SIEMENS
SIMATIC HMI
AP-SALD
6/22/2020 12:36:44 PM

Deposition

Aborted ● ● 0 181 Move flow to input ● Home Start Abort Pause Retry

Serial Devices

Running ● ● 2050 0 Get LA12 positions ● Home Start Abort Pause Retry

Recipe Overview

User Name: No.:

Recipe Name: No.:

Entry Name	Value
Stage Speed, mm/s	500
Start Position, mm	105
End Position, mm	405
Number of Oscillation	30
Stage Temperature, °C	35.0
Spacing Z Input, mm	0.125
Spacing Theta Input, °	0.0
Spacing Phi Input, °	0.0
Metal Bubbler Flow Rate, sccm	100
Metal Carrier Flow Rate, sccm	3000
Water Bubbler Flow Rate, sccm	1000
Water Carrier Flow Rate, sccm	4000
Nitrogen Curtain Flow Rate, sccm	5000

Data record read

Recipe Overview on PLC

User Number 1	Recipe Number 2
Linear Stage	Leveling
Start Position mm 105 Set	0.125
End Position mm 405 Set	
Speed mm/s 500 Set	z spacing mm
Oscillation Number 30	θ ° 0.0
35.0	φ ° 0.0
Mass Flow Controller's Flow Rate [sccm]	
Metal Bubbler 100	Metal Carrier 3000
Water Bubbler 1000	Water Carrier 4000
Nitrogen Curtain 5000	

Home
Valves Control
Stage Control
Recipe Overview
▶

Figure A.10 The recipe overview page of HMI.

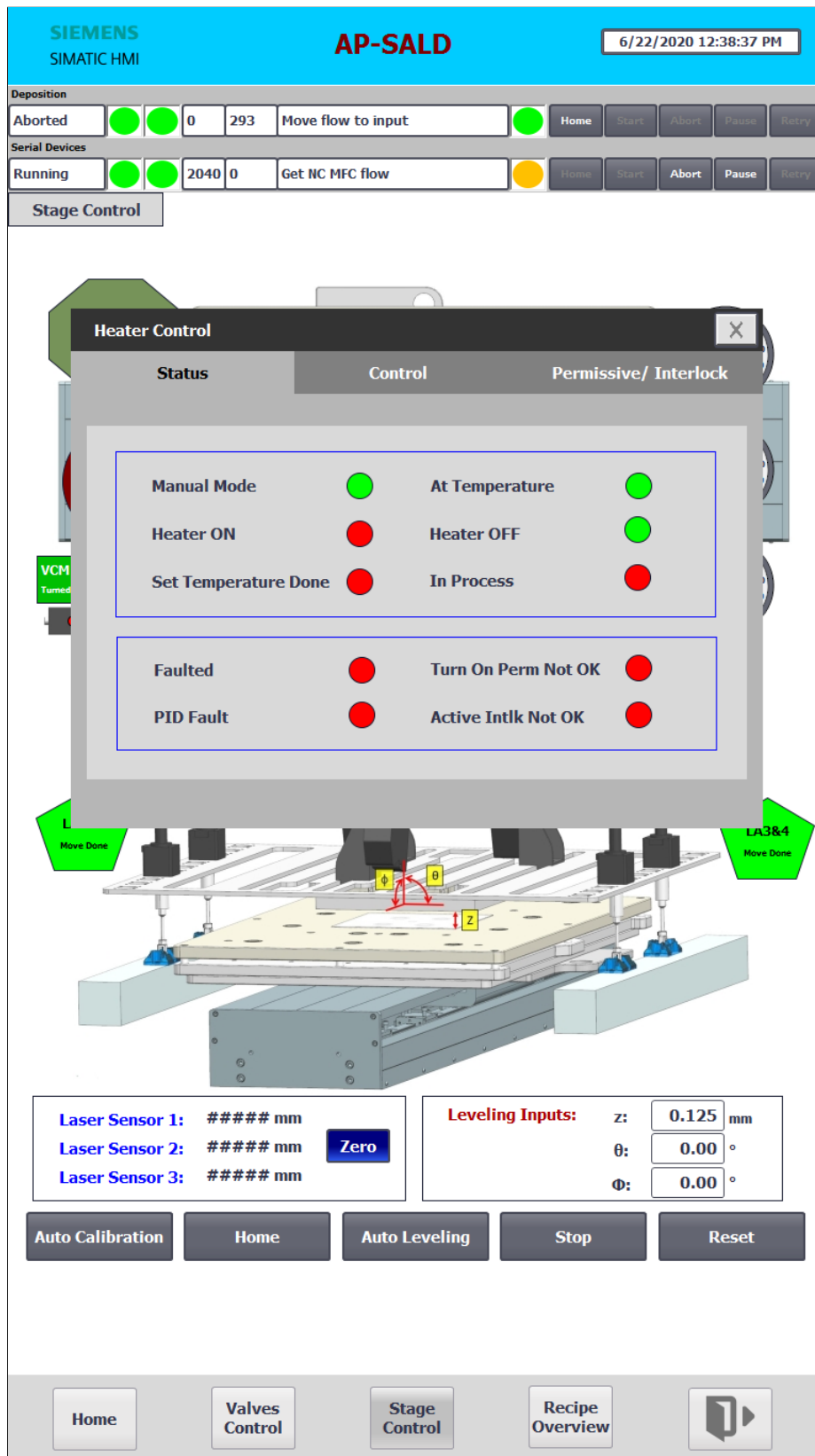


Figure A.11 The heater's status interface of HMI.

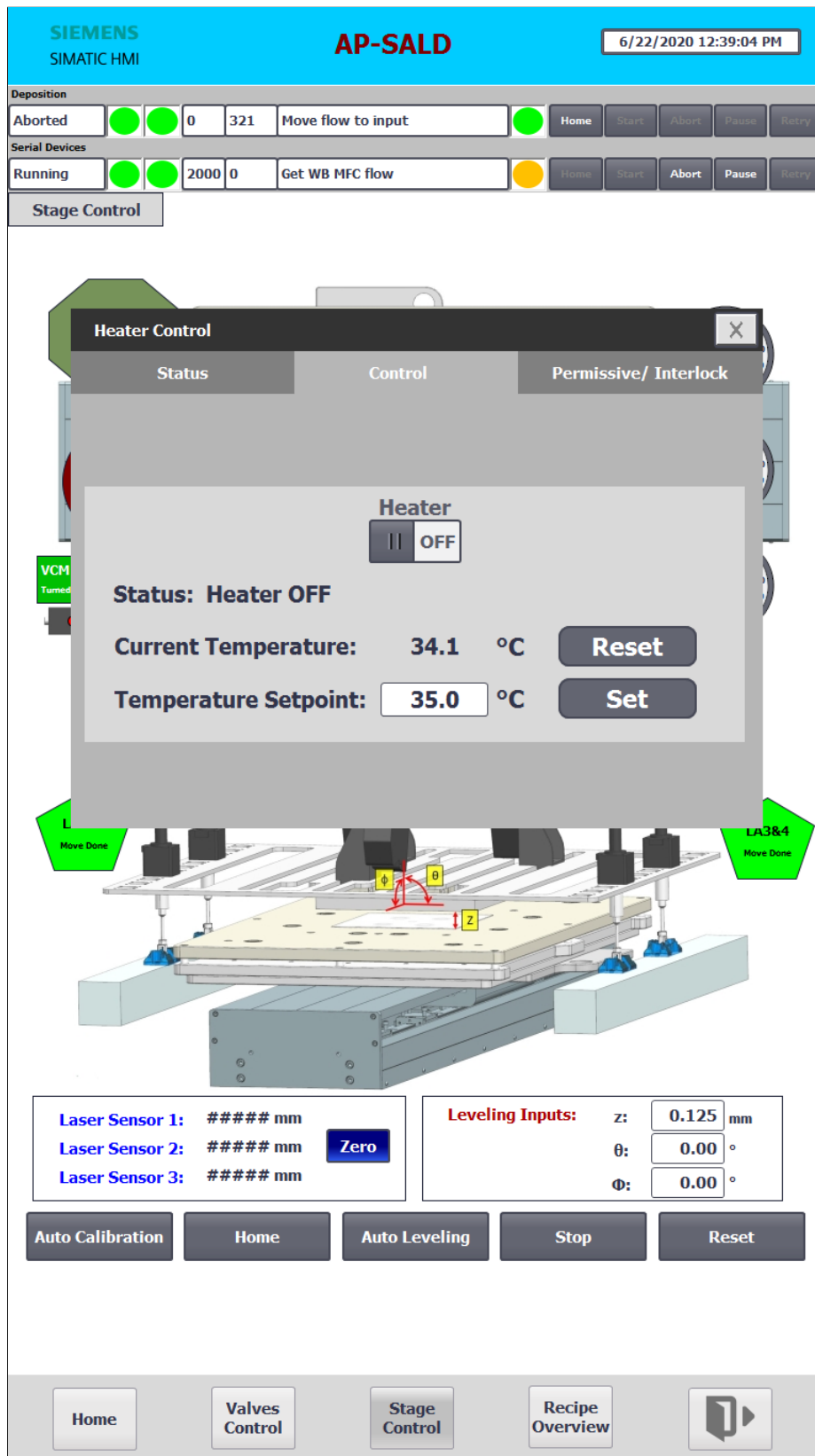


Figure A.12 The heater's control interface of HMI.

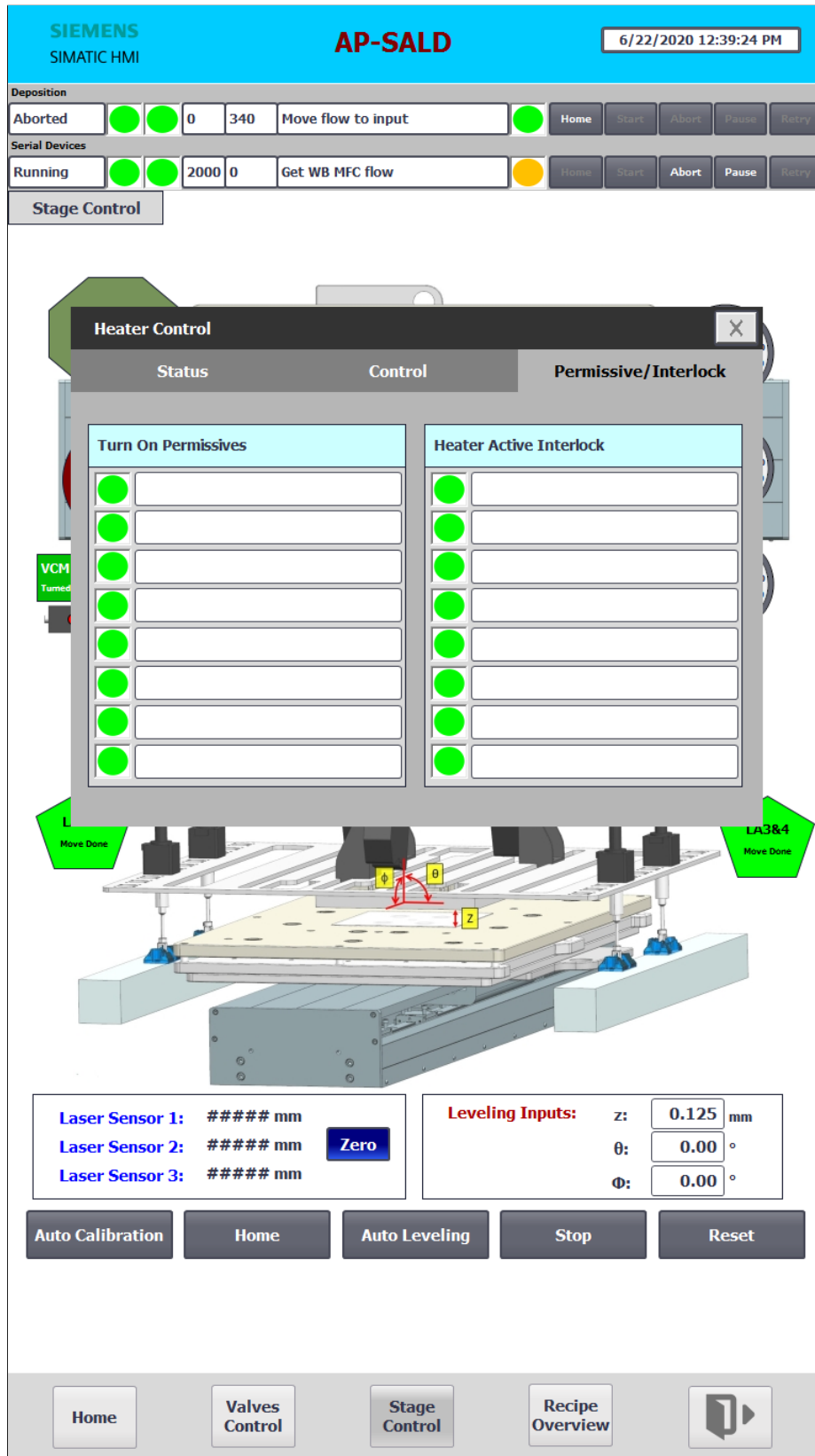


Figure A.13 The heater's permissive and interlock interface of HMI.

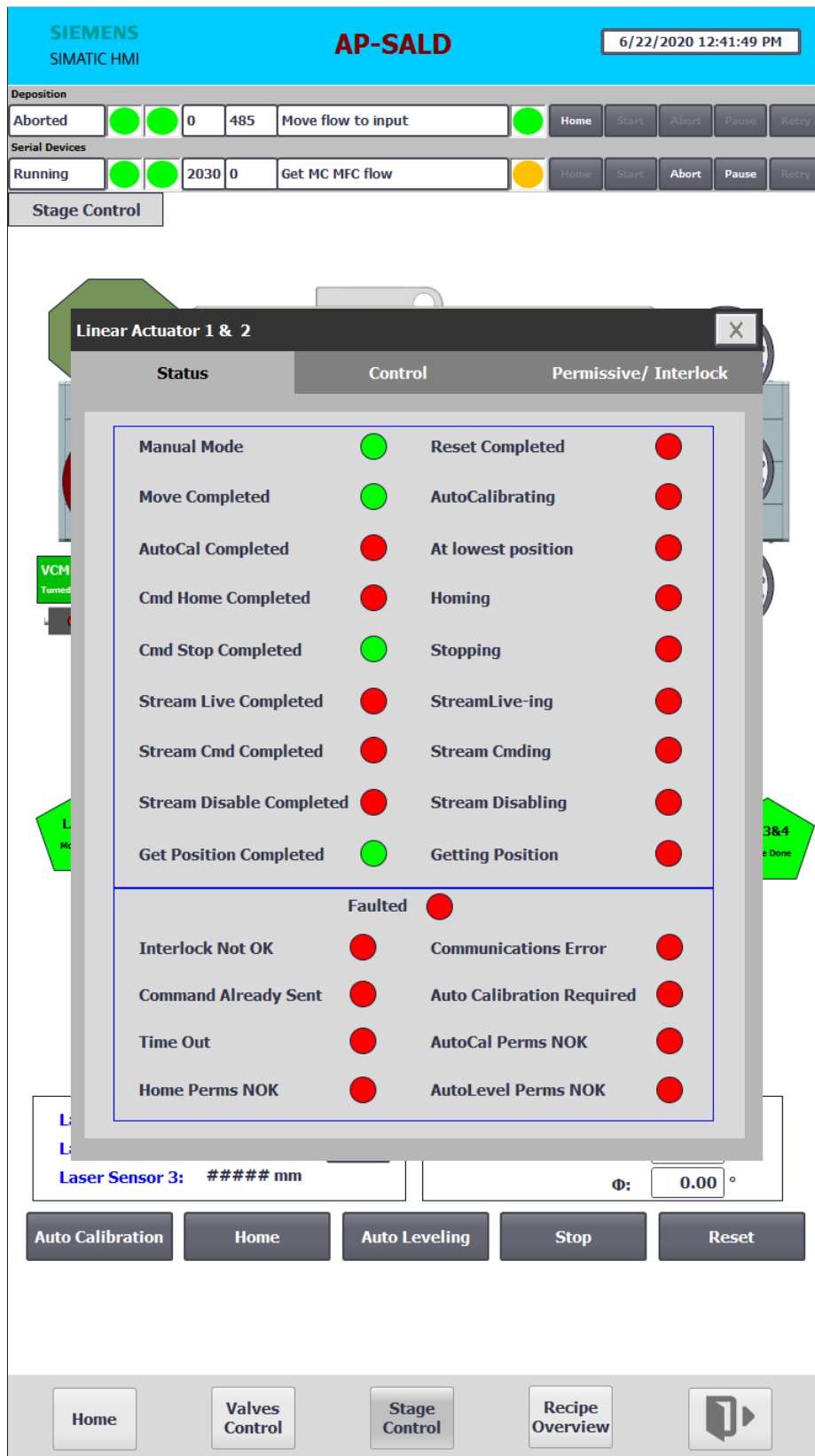


Figure A.14 The linear actuator's status interface of HMI.

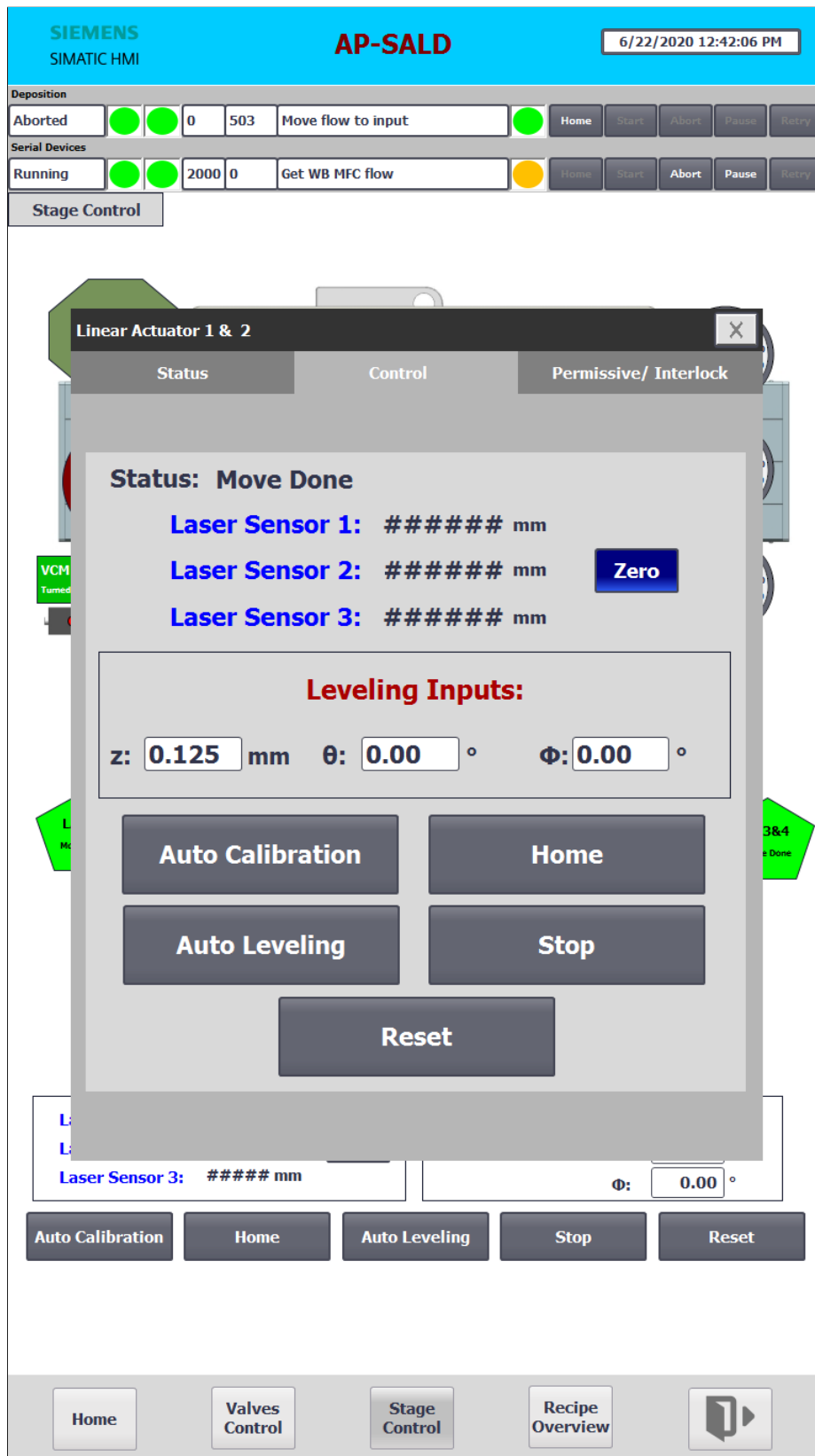


Figure A.15 The linear actuator's control interface of HMI.

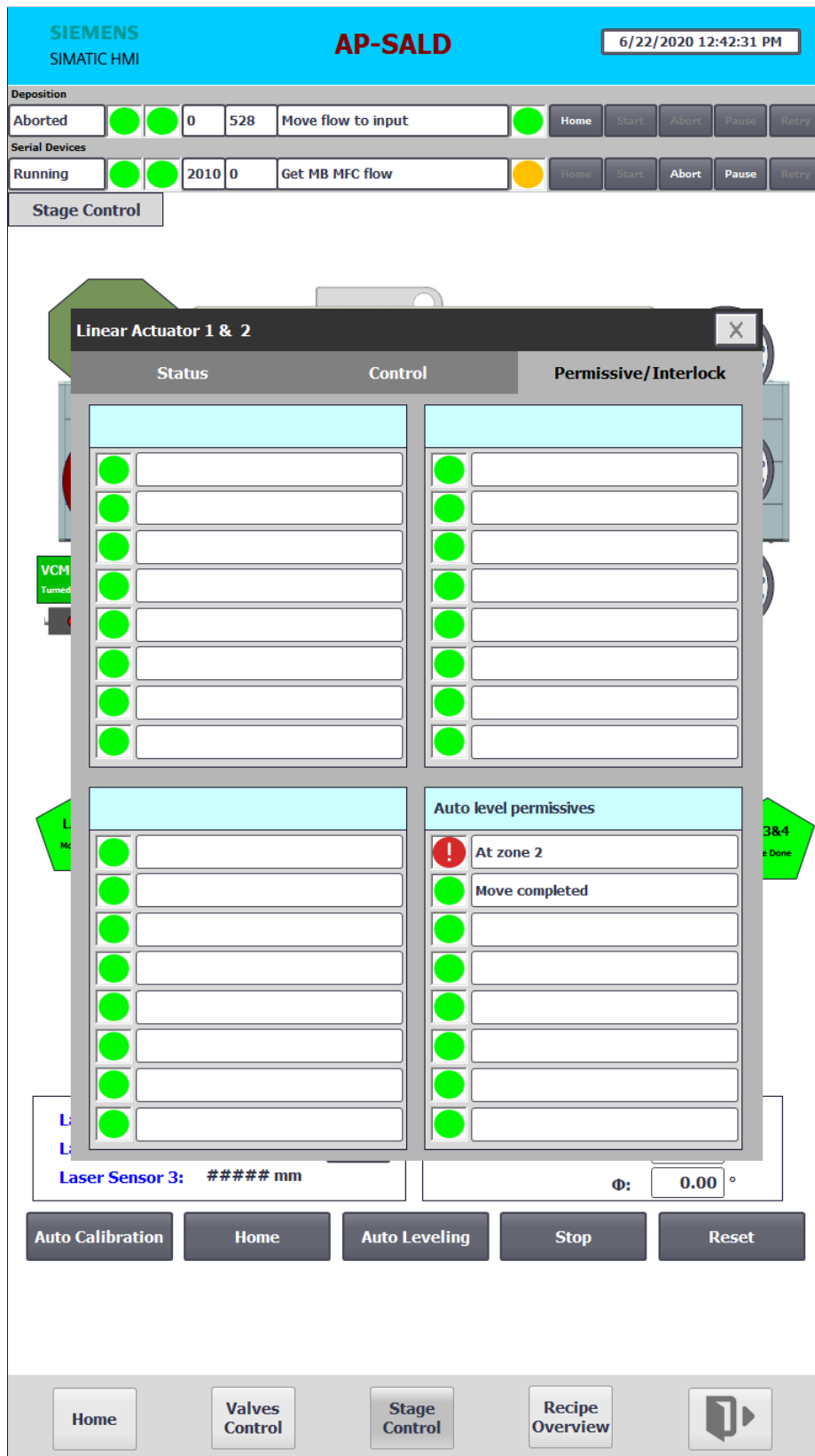


Figure A.16 The linear actuator's permissive and interlock interface of HMI.

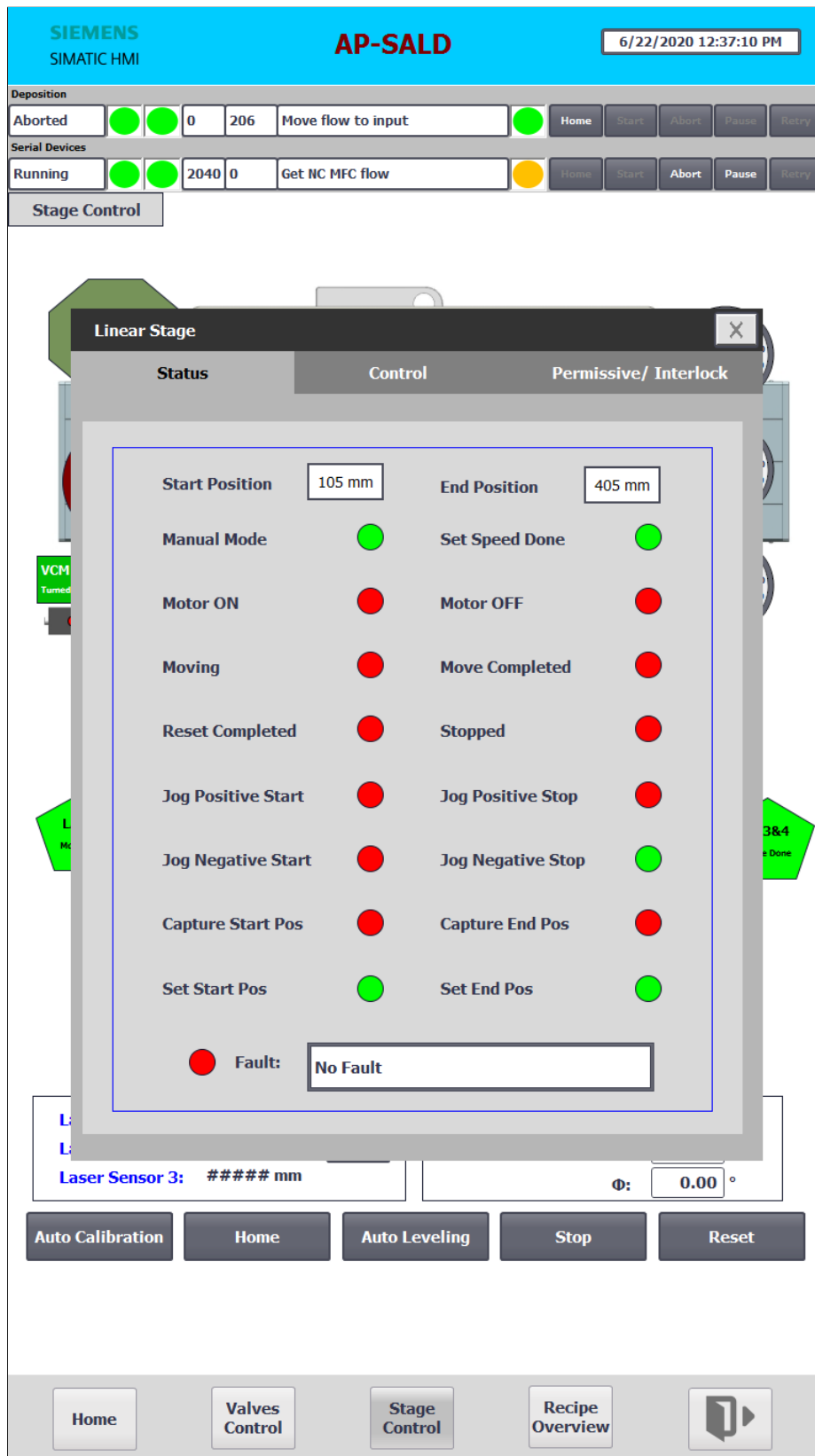


Figure A.17 The linear stage's status interface of HMI.



Figure A.18 The linear stage's control interface of HMI.

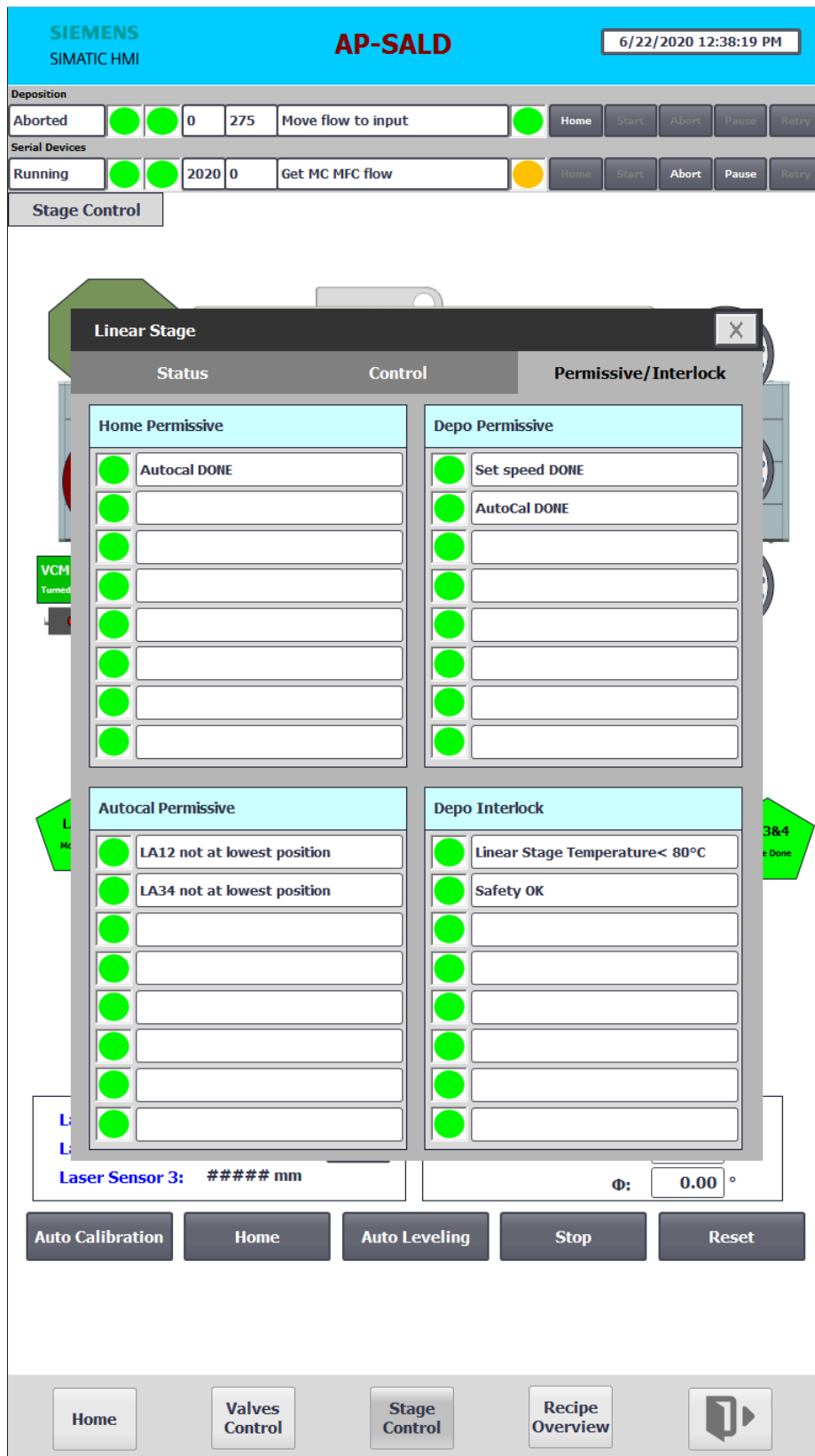


Figure A.19 The linear stage's permissive and interlock interface of HMI.

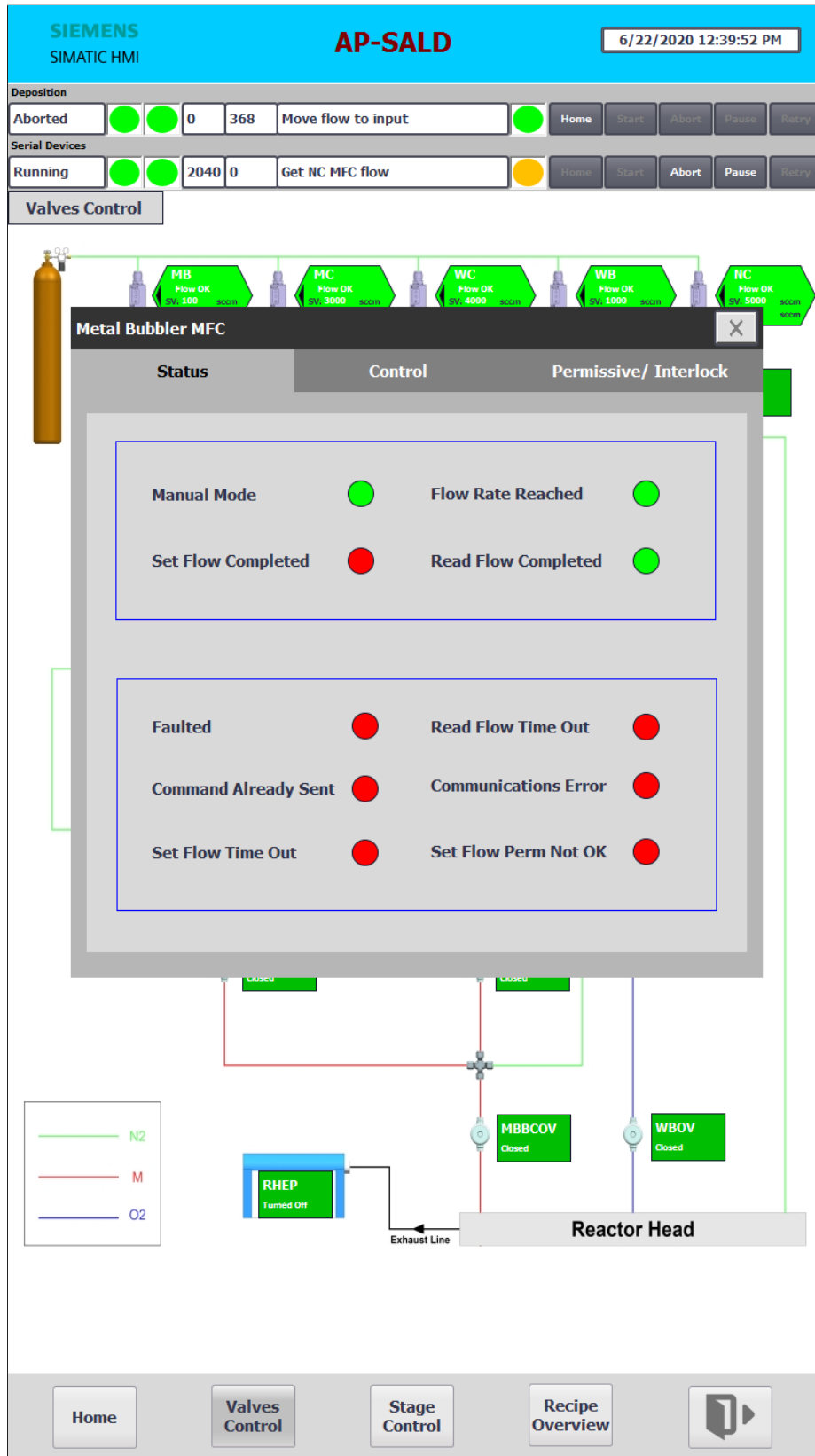


Figure A.20 The MFC's status interface of HMI.

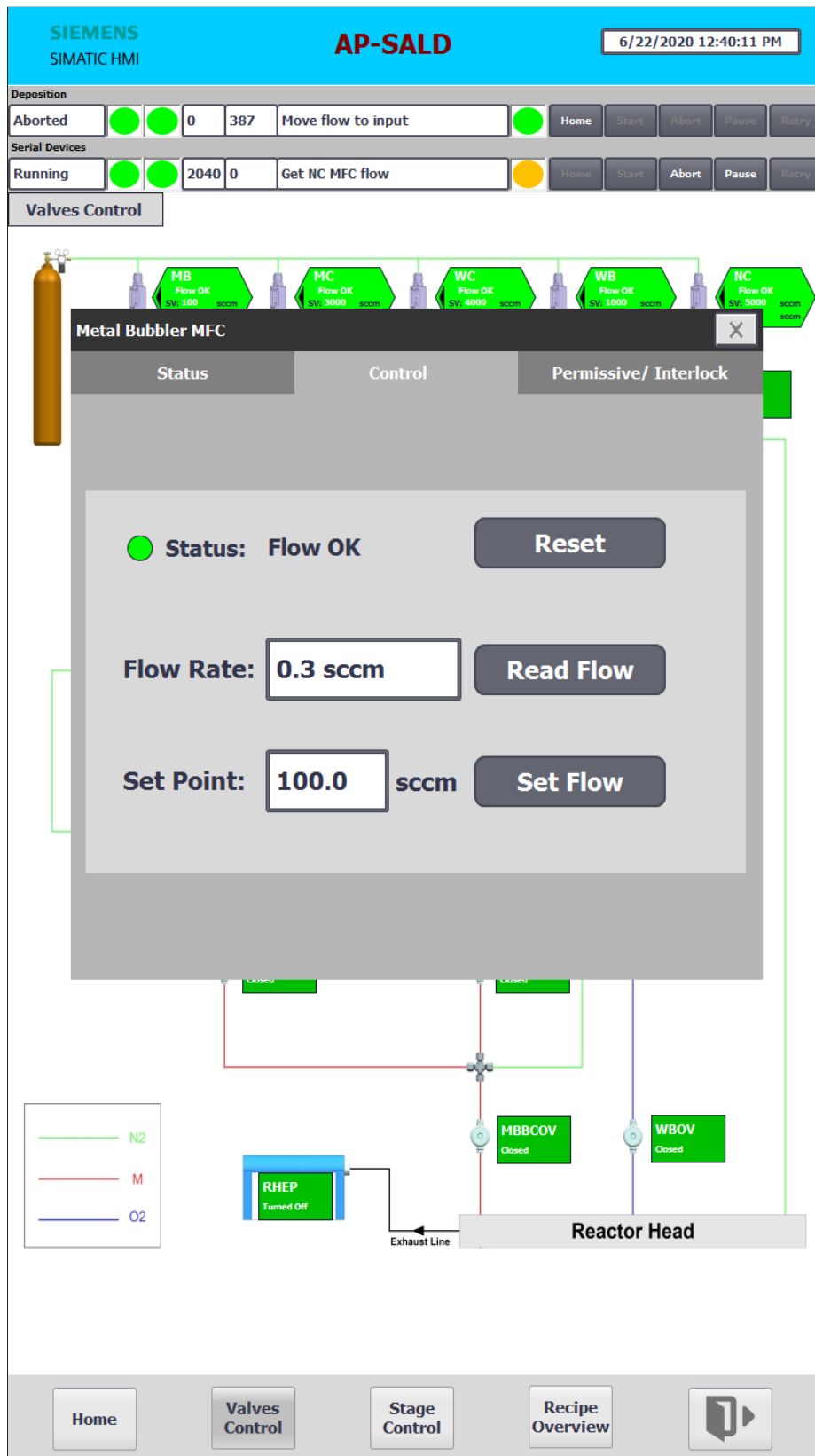


Figure A.21 The MFC's control interface of HMI.

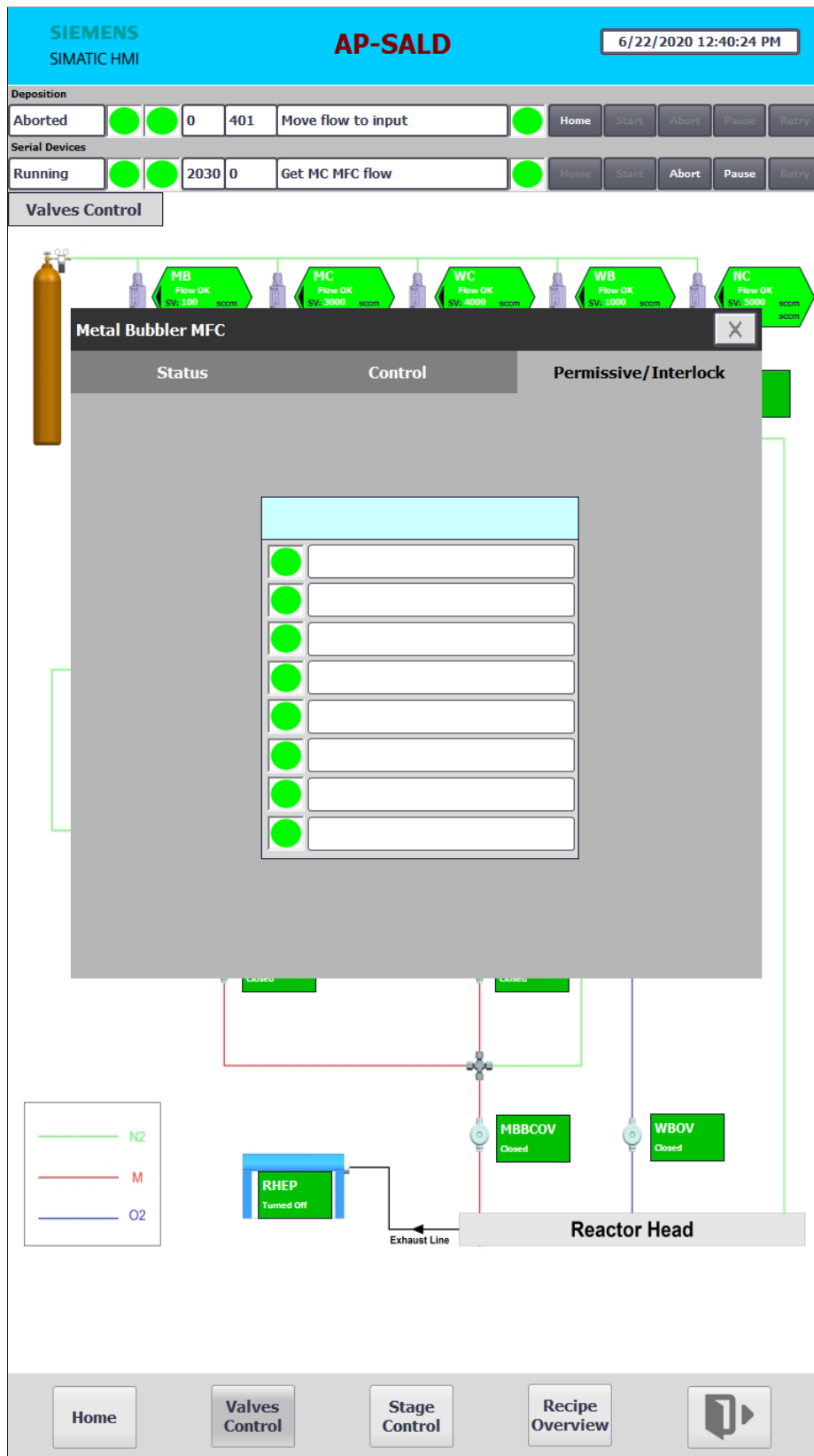


Figure A.22 The MFC's permissive and interlock interface of HMI.

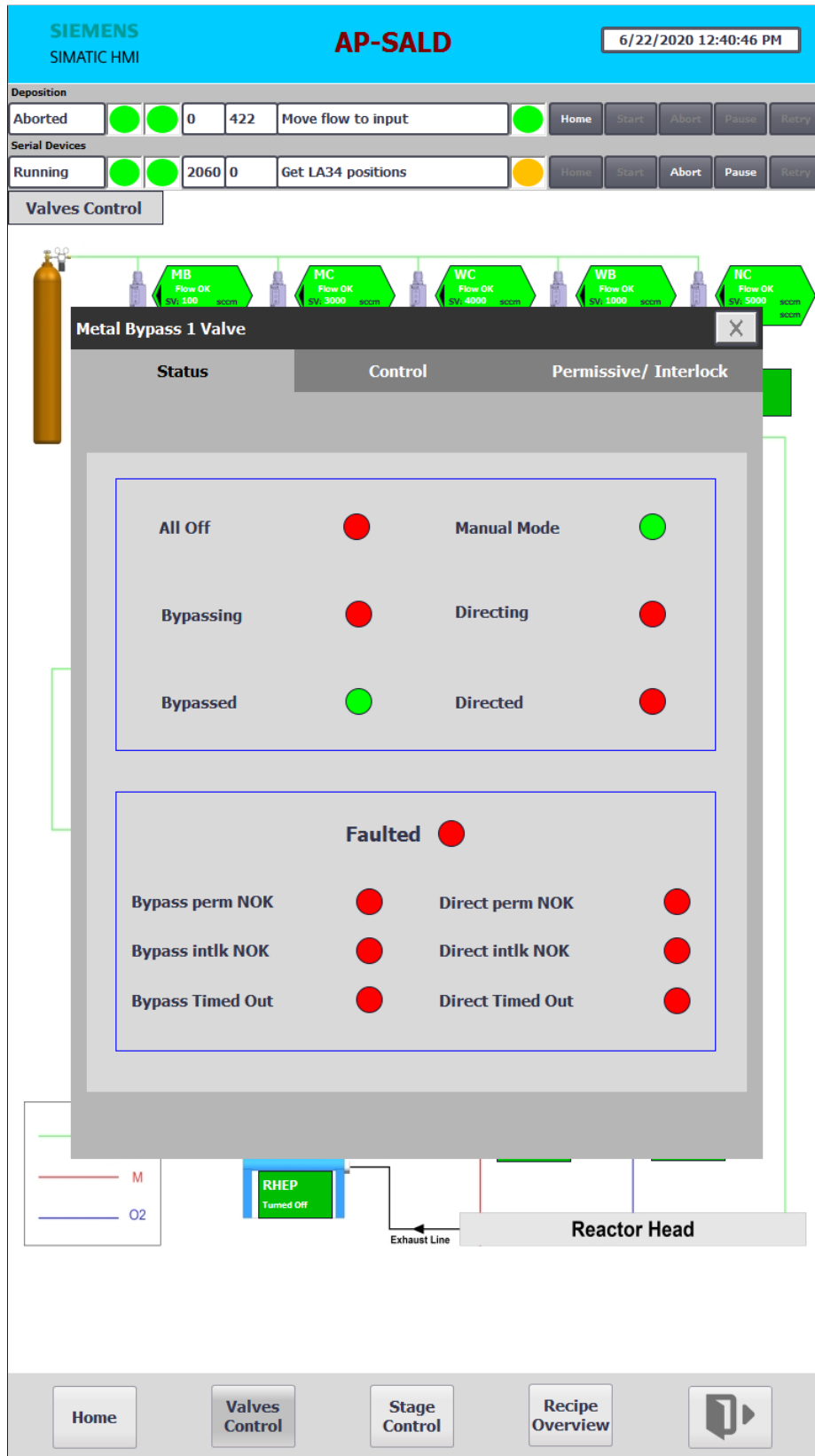


Figure A.23 The valve's status interface of HMI.

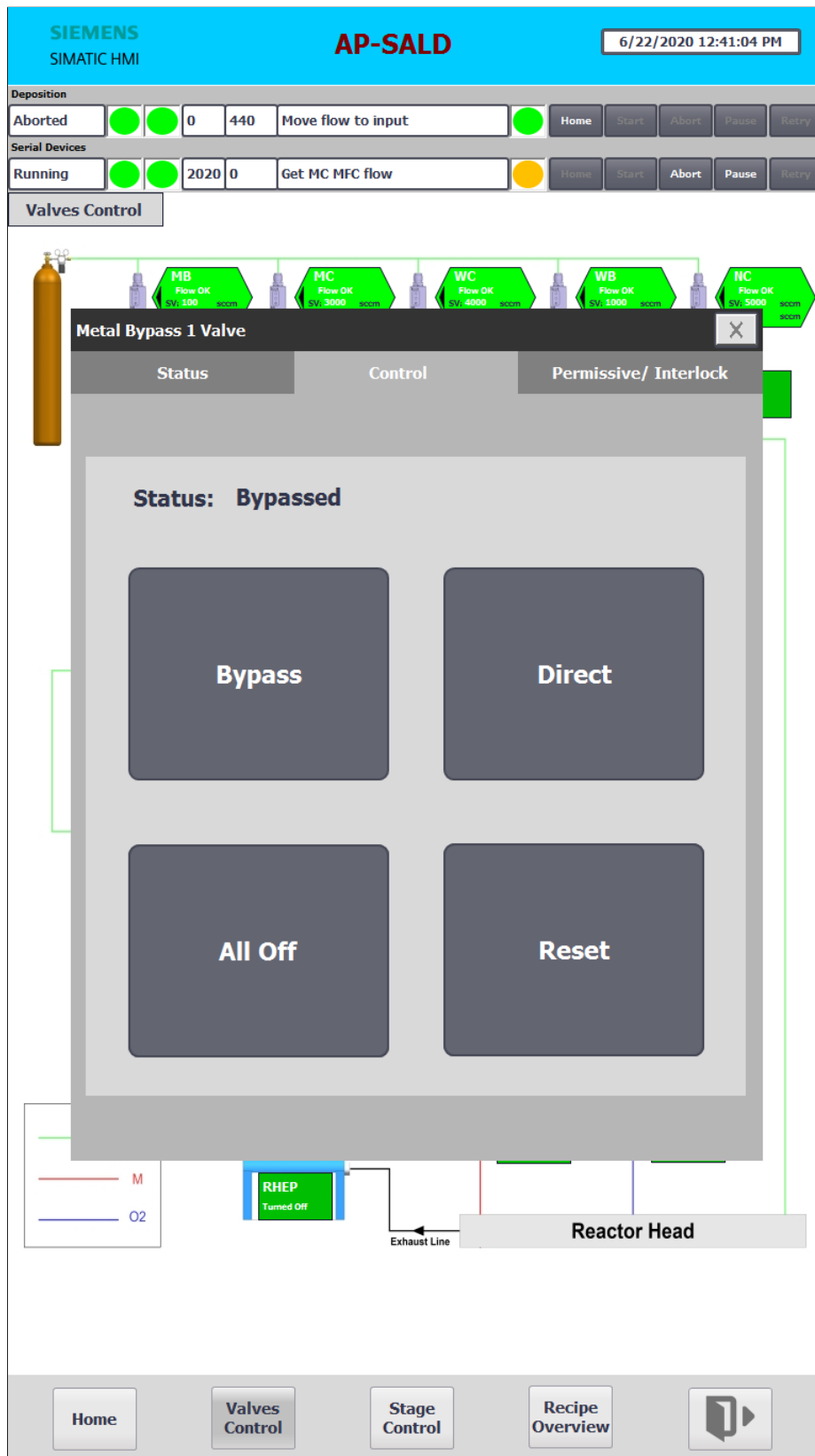


Figure A.24 The valve's control interface of HMI.

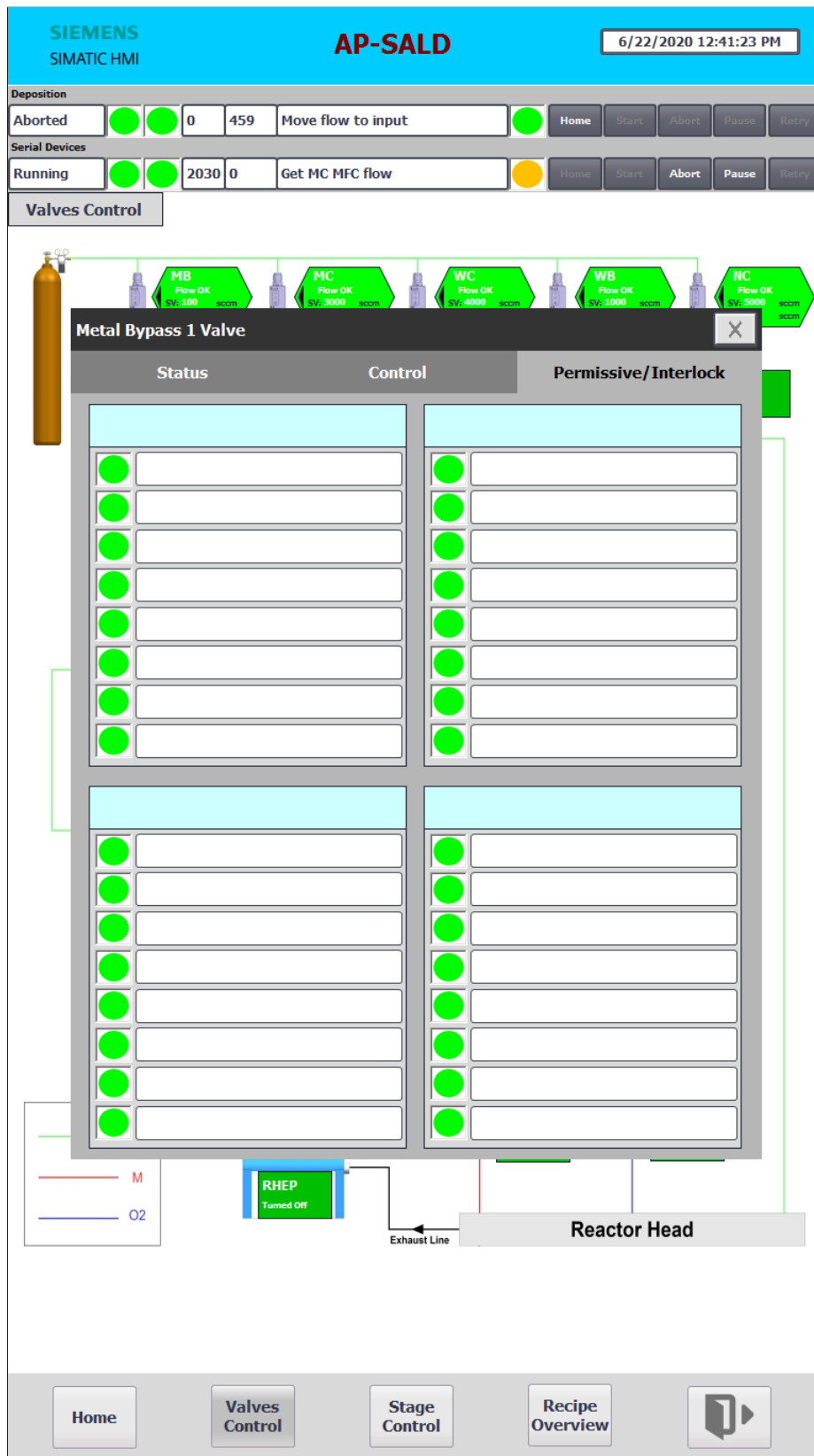


Figure A.25 The valve's permissive and interlock interface of HMI.

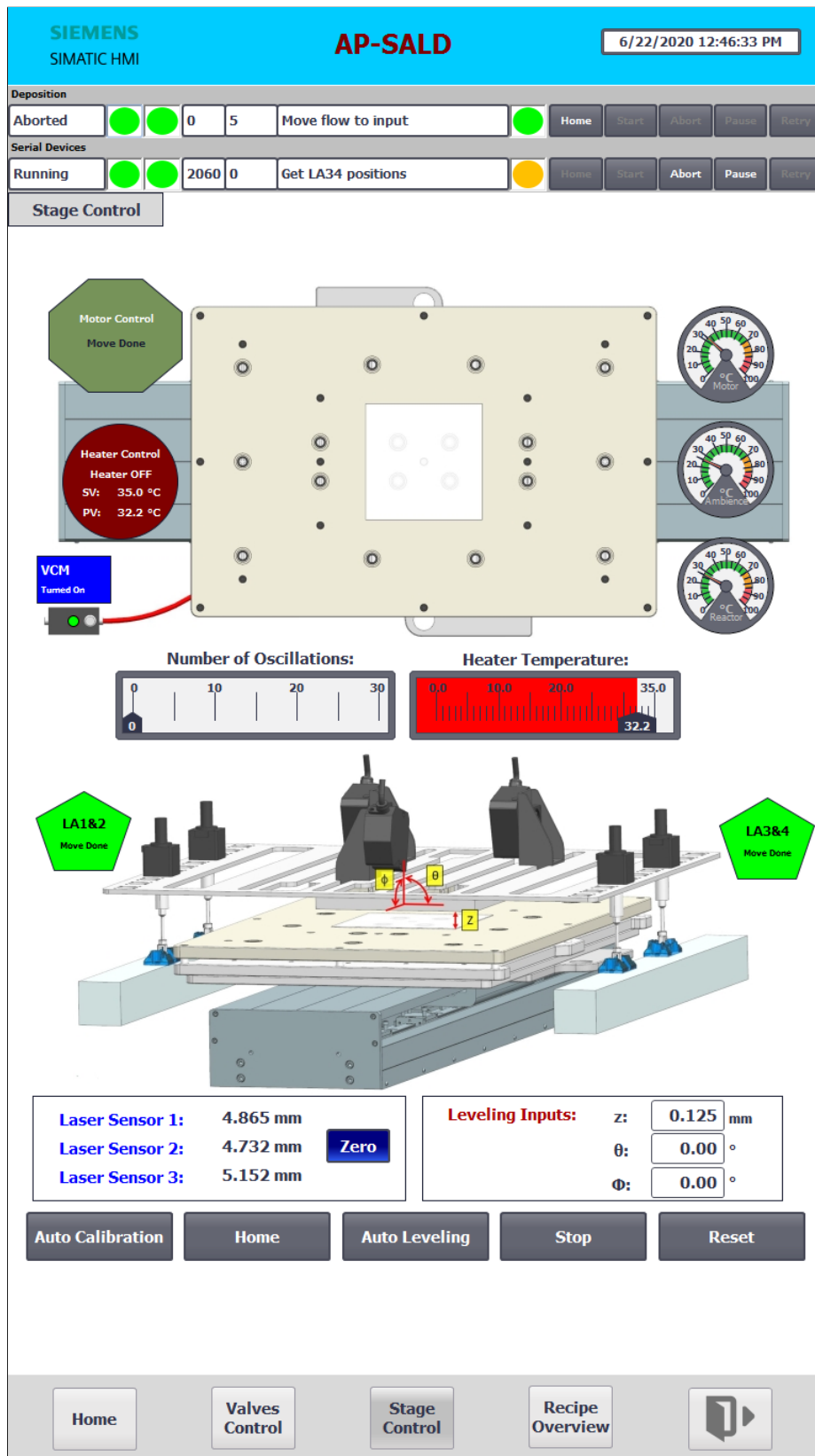


Figure A.26 The laser sensors' reading on the HMI before auto-leveling is commanded.

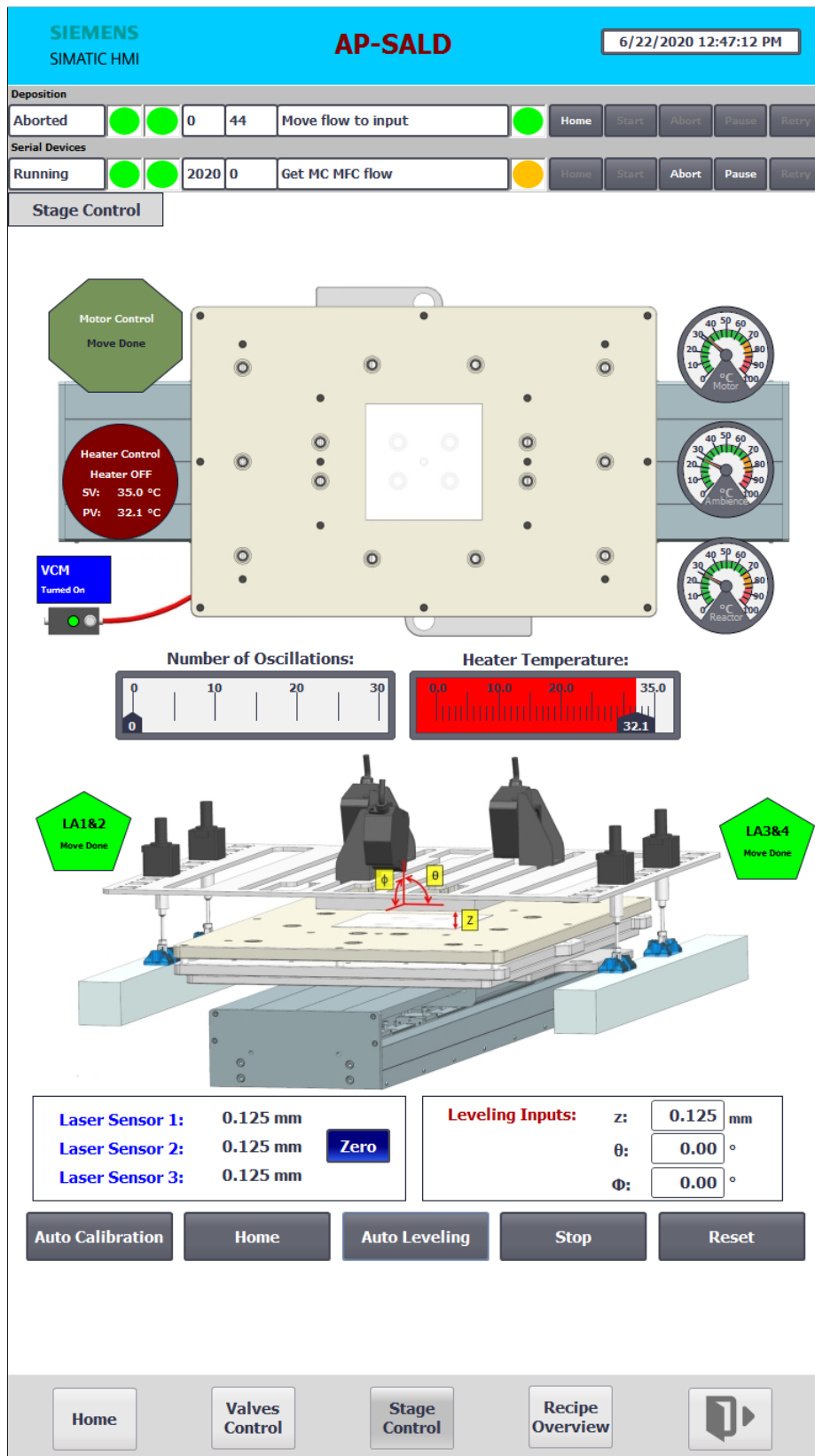


Figure A.27 The laser sensors' reading on the HMI after auto-leveling is commanded.

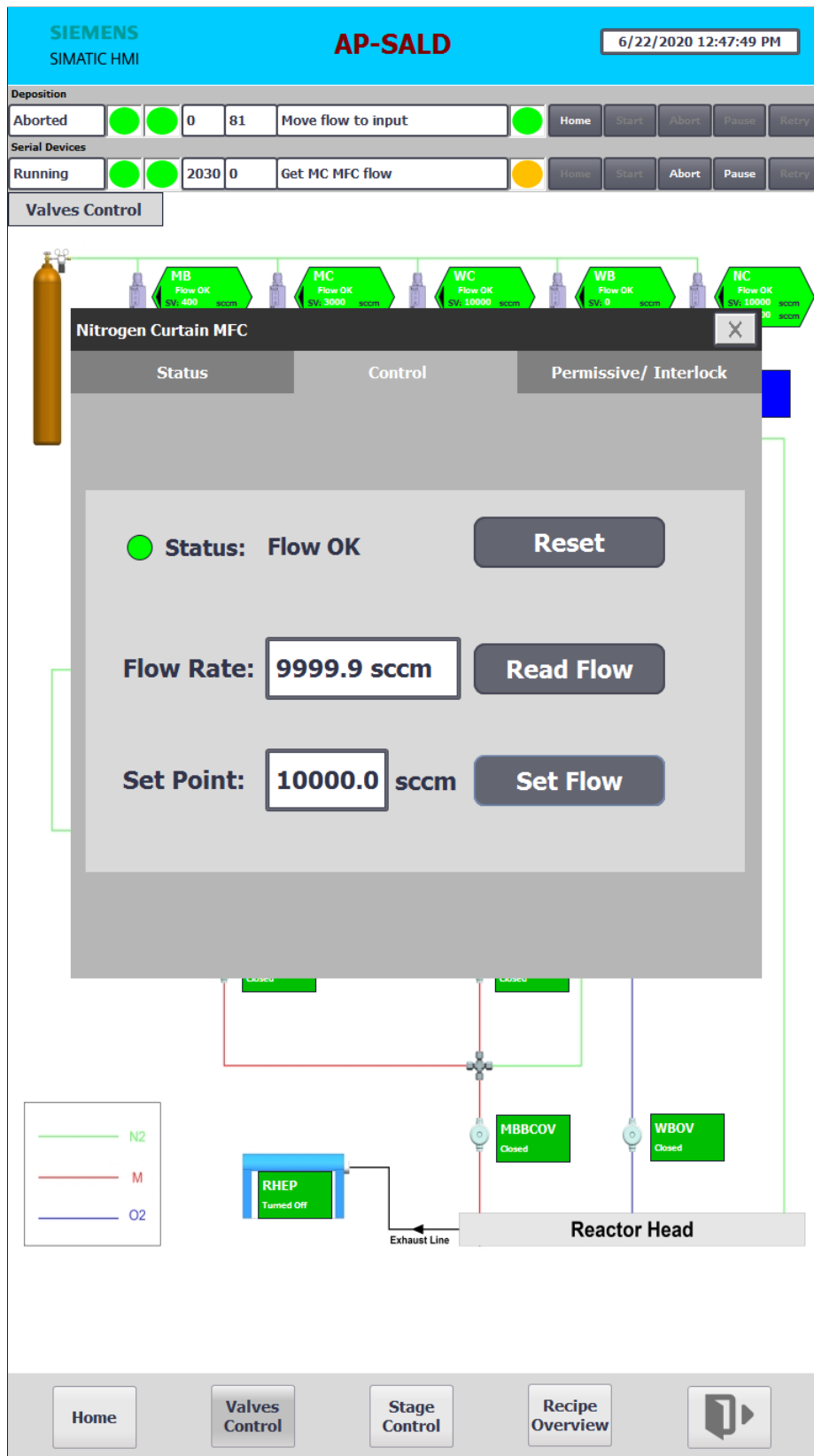


Figure A.28 A screenshot of flow reading vs. setpoint of mass flow controller from HMI.

Table A.2 The functions of each interface designed in the HMI.

Interface	Functions
Log-on page	It allows the users to sign in for basic access or advanced access. Basic access provides the users all the functions they need to operate the system, while advanced access will provide additional features to troubleshoot the program on top of the basic functions.
Home page	It shows the safety status of the door. If the door is opened, the green frame will turn flashing red and cut the flow. It also includes two brightness adjustment bars for the users to turn on and off the LED lights in the cabinet. Dry cycle switch allows the users to run the system without the chemical, while the buzzer silence button is included to mute the buzzer temporarily to allow the users to troubleshoot the errors in peace.
Valves Control page	It illustrates the connections between the flow devices and valves of AP-SALD system. It provides status overview of each components, such as the flow rates and set points of MFCs. The program has automated the opening and closing of the valves in the Running state. Hence, the users do not need to input any values here, unless they want to troubleshoot.
Stage Control page	It covers heater, linear stage, vacuum, linear actuators and laser sensors. It provides an overview of the temperatures of motor, ambience, reactor head, and heater, the laser sensors' readings, auto-leveling inputs, temperature setpoint, and number of oscillation. The users do not need to input any values here, unless they want to troubleshoot.
Recipe Overview page	This page is where the users create their recipes by inputting different setpoints for different parameters. This page provides the users an overview of their recipes and streamlines the operation. Their recipes will be saved in the database in the PLC. They can save and upload their recipes, or download the recipes into the PLC. Start position, End position, and Speed are the three variables that require the users to press SET.
Device's Status interface	It shows communication status and feedback of the device.
Device's Control interface	It allows the users to control and set values for the device during Manual mode (in Paused or Aborted state).
Device's Permissive/ Interlock interface	It shows permissives and interlocks of the device for the users to monitor and troubleshoot if there are any faults.